



**NTNU – Trondheim**  
Norwegian University of  
Science and Technology

# Development and Implementation of Effective Stress Soil Models

**Vegard Gavel-Solberg**

Civil and Environmental Engineering

Submission date: June 2014

Supervisor: Steinar Nordal, BAT

Co-supervisor: Gustav Grimstad, BAT  
Jon A. Rønningen, BAT

Norwegian University of Science and Technology  
Department of Civil and Transport Engineering





Report Title: Development and Implementation of Effective Stress Soil Models	Date: June 9, 2014		
	Number of pages (incl. appendices): 188		
	Master Thesis	X	Project Work
Name: Vegard Gavel-Solberg			
Professor in charge/supervisor: Professor Steinar Nordal			
Other external professional contacts/supervisors: Professor Gustav Grimstad, PhD Candidate Jon A. Rønningen			

**Abstract:**  
Soil exhibit complex behavior that require advanced models to recreate stiffness and strength during loading. The complex behavior may be due to preconsolidation, dilation and contraction, softening, anisotropy, stress dependency or other effects.

Today, an effective stress based soil model for soft Scandinavian clays is being developed at NTNU, as part of the ongoing research project GeoFuture. The goal of this thesis is to implement and develop an effective stress based soil model, applying the concept of modular programming used in the GeoFuture project.

The soil model was implemented using Fortran and MATLAB code for application in PLAXIS. Modular programming was used to separate the implemented code into two material independent codes and one material dependent code. For development of the model, only the material dependent code needs to be modified.

A simple linear elastic-perfect plastic Drucker--Prager model was implemented at first. Simulations in PLAXIS were performed, using the implemented model and the Mohr--Coulomb model in PLAXIS to compare the behavior. For simulation of triaxial compression and extension tests, the models gave the same behavior. In plane strain conditions, the implemented model gave a softer response close to failure. The same strength is obtained for the two models, yet greater deformations arise before failure in the Drucker--Prager model.

Applying the advantage of modular programming, the model was further developed to include strain hardening and stress dependent dilatancy. Two formulations of stress dependent dilatancy were used to reproduce behavior of sand in undrained conditions. Simulations of undrained triaxial tests using the model were performed, showing that only one formulation gave the intended behavior.

The stress dependent dilatancy was finally related to a critical void ratio for a critical state. Using both constant and mean stress dependent elastic stiffnesses, undrained triaxial compression tests on Toyoura sand were simulated. Simulations gave a good fit between the test results and the simulations. The mean stress dependent stiffness gave superior simulations compared to the constant stiffness.

During the development of the model, continuous testing has been executed. The concept of modular programming has shown to perform well. After establishing the first framework with material dependent and independent routines, including new features, or even changing constitutive model, is a manageable and convenient task. The concept yields a good tool for implementing and developing constitutive models of soils.

As the strength of the implemented model must be correlated manually to the relevant stress state, further development of the model should include a Lode angle dependency of the strength. Mobilization dependent dilatancy is not included and would improve the performance. A more complete evaluation of material properties from laboratory tests with subsequent simulations would be of great interest to indicate the predictive capacity of the model.

**Keywords:**

- |                                       |
|---------------------------------------|
| 1. Effective stress based soil models |
| 2. Drucker-Prager strength criterion  |
| 3. User-defined soil models (PLAXIS)  |
| 4. Toyoura sand                       |





# Preface

This Master's Thesis is the final part of the integrated five-year Master of Science program in Civil and Environmental Engineering at Norwegian University of Science and Technology (NTNU). The specialization in Geotechnical Engineering is one of the possible specializations of the Structural Engineering branch of the program. For this specialization, TBA4900 Geotechnical Engineering, Master's Thesis is mandatory and finishes the master's degree.

The Master's Thesis was carried out during the spring semester of 2014. Professor Steinar Nordal brought up the idea to this Master's Thesis through a conversation in the fall of 2013. My interest for constitutive modeling was triggered during the fourth year in my study program when studying material mechanics of metals and alloys. The Project Thesis during the fall of 2013 gave me the opportunity to obtain more insight into constitutive modeling of soils. The Master's Thesis was carried out individually for the Department of Civil and Transport Engineering, Geotechnical Engineering group, in close collaboration with PhD Candidate Jon A. Rønningen.

Trondheim, June 9, 2014

---

Vegard Gavel-Solberg

# Acknowledgements

I would like to express my gratitude to my supervisor, Professor Steinar Nordal, as always welcoming for guidance and questions. During my Master's Thesis, I have had the opportunity to study constitutive soil modeling and the guidance of Professor Nordal has truly been valuable to acquire a deeper understanding of geotechnics.

PhD Candidate Jon A. Rønningen has offered me extraordinary help during this spring. Even though powerful, Fortran programming can be quite frustrating and without his follow-up and aid I would probably still be debugging the code. My work has been made a lot easier and I am very grateful for his assistance and help.

Professor Gustav Grimstad has been helpful for discussing both constitutive modeling and implementation into PLAXIS by Fortran code, giving new perspectives to the theory and finding solutions to problems.

Every workplace consists of more than just tasks and duties and I am lucky to have such good study colleagues and friends. Through many academic discussions, laughs and long nights at the reading room, we've learned from each other and helped each other through hard work. Now we are finally engineers!

Last but not least, I am thankful to my loving wife, Léonor, who lightens up each day and helps me get my spirit up when I am down. You have made my days brighter and funnier even when an enormous amount of errors and failed calculations have dominated. Next spring I'm making you dinners.

V.G.S.

# Abstract

Soil exhibit complex behavior that require advanced models to recreate stiffness and strength during loading. The complex behavior may be due to preconsolidation, dilation and contraction, softening, anisotropy, stress dependency or other effects.

Today, an effective stress based soil model for soft Scandinavian clays is being developed at NTNU, as part of the ongoing research project GeoFuture. The goal of this thesis is to implement and develop an effective stress based soil model, applying the concept of modular programming used in the GeoFuture project.

The soil model was implemented using Fortran and MATLAB code for application in PLAXIS. Modular programming was used to separate the implemented code into two material independent codes and one material dependent code. For development of the model, only the material dependent code needs to be modified.

A simple linear elastic-perfect plastic Drucker–Prager model was implemented at first. Simulations in PLAXIS were performed, using the implemented model and the Mohr–Coulomb model in PLAXIS to compare the behavior. For simulation of triaxial compression and extension tests, the models gave the same behavior. In plane strain conditions, the implemented model gave a softer response close to failure. The same strength is obtained for the two models, yet greater deformations arise before failure in the Drucker–Prager model.

Applying the advantage of modular programming, the model was further developed to include strain hardening and stress dependent dilatancy. Two formulations of stress dependent dilatancy were used to reproduce behavior of sand in undrained conditions. Simulations of undrained triaxial tests using the model were performed, showing that only one formulation gave the intended behavior.

The stress dependent dilatancy was finally related to a critical void ratio

for a critical state. Using both constant and mean stress dependent elastic stiffnesses, undrained triaxial compression tests on Toyoura sand were simulated. Simulations gave a good fit between the test results and the simulations. The mean stress dependent stiffness gave superior simulations compared to the constant stiffness.

During the development of the model, continuous testing has been executed. The concept of modular programming has shown to perform well. After establishing the first framework with material dependent and independent routines, including new features, or even changing constitutive model, is a manageable and convenient task. The concept yields a good tool for implementing and developing constitutive models of soils.

As the strength of the implemented model must be correlated manually to the relevant stress state, further development of the model should include a Lode angle dependency of the strength. Mobilization dependent dilatancy is not included and would improve the performance. A more complete evaluation of material properties from laboratory tests with subsequent simulations would be of great interest to indicate the predictive capacity of the model.

# Sammendrag

Jords kompliserte oppførsel krever avanserte materialmodeller for å gjenskape stivhet og styrke ved belastning. Den kompliserte oppførselen kan skyldes prekonsolidering, dilatans og kontaktans, styrkereduksjon, anisotropi eller spenningsavhengigheter for å nevne noen effekter.

Som en del av et pågående forskningsprosjekt, GeoFuture, utvikles det på NTNU nå en effektivspenningsbasert jordmodell for bløt, skandinavisk leire. Målet for denne masteroppgaven er å vise hvordan en effektivspenningsbasert jordmodell kan implementeres og utvikles ved hjelp av modulær programmering, et av prinsippene brukt i GeoFuture-prosjektet.

Jordmodellen har blitt implementert ved hjelp av Fortran- og MATLAB-kode, for bruk i PLAXIS. Modulær programmering ble brukt til å dele programkoden inn i to materialuavhengige koder og en materialavhengig kode. Kun den materialavhengige koden må endres ved utvikling av modellen.

Først ble en enkel lineær elastisk-perfekt plastisk Drucker–Prager-modell implementert. Deretter ble modellen brukt til simuleringer i PLAXIS og Mohr–Coulomb-modellen i PLAXIS ble brukt som referanse for å sammenligne oppførselen. Modellene ga lik oppførsel for simuleringer av treaksiale trykk- og strekkforsøk. Den implementerte modellen ga en mykere oppførsel nær brudd i plan tøyingsforhold. Modellene ga samme styrke, men Drucker–Prager-modellen ga større deformasjoner før brudd.

Modellen ble videre utviklet med bruk modulær programmering for å inkludere tøyingskontrollert fastning og spenningsavhengig dilatans. To dilatansformuleringer ble brukt for å forsøke å gjenskape oppførselen til sand i udrenert tilstand. Simuleringer av udrenerte, treaksiale trykkforsøk viser at bare én av formuleringene ga ønsket oppførsel.

Til slutt ble den spenningsavhengige dilatansen koplet til et kritisk pore-tall for en kritisk tilstand (*critical state*). Både konstante og middelspenningsavhengige elastiske stivheter ble brukt i simuleringer av udrenerte, treaksiale trykkforsøk på Toyoura-sand. Simuleringene gjenskapte viktige aspekter

ved oppførselen godt. Middelspenningsavhengig stivhet gjensker oppførselen klart bedre enn konstant stivhet.

Gjennom utviklingsprosessen har kontinuerlig testing av modellen blitt gjennomført. Konseptet med modulær programmering har vist seg å fungere godt. Etter at rutinene først er etablert er det en relativt enkel oppgave å legge til nye effekter, eller til og med bytte materialmodell. Konseptet er et godt verktøy for implementering og utvikling av jordmodeller.

Etttersom styrken til den implementerte jordmodellen må korrigeres etter spenningssituasjonen manuelt, bør videre utvikling av modellen inkludere avhengighet av Lode-vinkelen. Mobiliseringsavhengig dilatans er ikke inkludert så langt, og vil forbedre modellens evne til å gjensker jords oppførsel. En mer fullstendig tolkning av materialeegenskaper fra laboratorieundersøkelser med påfølgende simuleringer, vil være svært interessant for å kunne si noe om modellens evne til å forutsi jords oppførsel for andre spenningstilstander.

# Contents

<b>1</b>	<b>Introduction</b>	<b>1</b>
1.1	Background . . . . .	1
1.2	Problem Formulation . . . . .	1
1.3	Objectives . . . . .	2
1.4	Limitations and Approach . . . . .	2
1.5	Relevant Literature . . . . .	3
1.6	Structure of the Report . . . . .	3
<b>2</b>	<b>Theoretical Foundation</b>	<b>5</b>
2.1	The Finite Element Method . . . . .	5
2.1.1	Key Assumptions and Principles of Finite Element Method	5
2.1.2	Finite Element Software . . . . .	7
2.2	Continuum Mechanics . . . . .	7
2.2.1	Key Assumptions in Soil Modeling . . . . .	7
2.2.2	Stresses and Stress Invariants . . . . .	8
2.2.3	Deviatoric Stresses and Deviatoric Stress Invariants . .	9
2.2.4	Haigh-Westergaard Coordinates and Stress Space . . . .	11
2.2.5	Strains and Strain Invariants . . . . .	12
2.3	Elasto-Plastic Soil Models . . . . .	13
2.3.1	Elasto-Plasticity: Strain Decomposition . . . . .	14
2.3.2	Elasticity: Linear Elasticity . . . . .	14
2.3.3	Elasticity: Nonlinear Elasticity . . . . .	16
2.3.4	Plasticity: Yield Criteria . . . . .	16
2.3.5	Plasticity: Flow Rule . . . . .	17
2.3.6	Plasticity: Hardening Rule . . . . .	18
2.3.7	Elasto-Plasticity: The Constitutive Matrix . . . . .	20

2.4	Undrained Conditions . . . . .	20
2.5	The Mohr–Coulomb Criterion . . . . .	21
2.5.1	Defining Equations . . . . .	21
2.5.2	Triaxial Test Formulation . . . . .	22
2.5.3	Plane Strain Formulation . . . . .	23
2.5.4	Mean and Deviatoric Stress Formulations . . . . .	24
2.5.5	Dilatancy Control . . . . .	25
2.5.6	Yield Surfaces in Haigh-Westergaard Coordinates . . . . .	27
2.6	The Drucker–Prager Criterion . . . . .	27
2.6.1	Defining Equations . . . . .	27
2.6.2	Coefficients of the Drucker-Prager Criterion . . . . .	28
2.6.3	Yield Surface in Haigh-Westergaard Coordinates . . . . .	31
2.6.4	Hardening Parameter . . . . .	33
2.6.5	Dilatancy and Dilatancy Control . . . . .	34
2.7	State Parameter for Sands and Sand Modeling . . . . .	36
2.7.1	A State Parameter for Sands . . . . .	36
2.7.2	A Sand Model Applying the State Parameter . . . . .	37
2.8	Numerical Methods . . . . .	39
2.8.1	Stress Integration . . . . .	39
2.8.2	Newton–Raphson Method . . . . .	40
<b>3</b>	<b>Implementation of an Elasto-Plastic Soil Model</b>	<b>45</b>
3.1	Calculation Process . . . . .	45
3.1.1	PLAXIS User-Defined Soil Models . . . . .	45
3.1.2	The Stress Integration Algorithm . . . . .	46
3.1.3	Modular Programming . . . . .	47
3.2	Material Independent Subroutines . . . . .	50
3.2.1	Main Subroutine . . . . .	50
3.2.2	Helper Subroutine . . . . .	52
3.2.3	User Interface Subroutine . . . . .	53
3.3	Development of Material Dependent Subroutine . . . . .	53
3.3.1	Linear Elastic-Perfect Plastic Model . . . . .	53
3.3.2	Strain Hardening and Stress Dependent Dilatancy . . . . .	53



3.3.3	Void Ratio Dependent Dilatancy . . . . .	54
3.4	Linear Elastic-Perfect Plastic Model . . . . .	54
3.4.1	Associated Flow . . . . .	54
3.4.2	Non-Associated Flow . . . . .	56
3.5	Strain Hardening and Stress Dependent Dilatancy . . . . .	57
3.5.1	Strain Hardening and Stress Dependent Dilation Angle	57
3.5.2	Strain Hardening and Stress Dependent Dilation Coefficient . . . . .	58
3.6	Void Ratio Dependent Dilatancy . . . . .	60
3.6.1	Void Ratio Dependency with Constant Elastic Stiffness	60
3.6.2	Mean Stress Dependency of Elastic Stiffness . . . . .	61
<b>4</b>	<b>Testing the Model</b>	<b>63</b>
4.1	Linear Elastic-Perfect Plastic Model . . . . .	63
4.1.1	Associated Flow in Single Material Point . . . . .	63
4.1.2	Non-Associated Flow in Single Material Point . . . . .	64
4.1.3	Loading and Safety Calculations . . . . .	64
4.2	Strain Hardening and Stress Dependent Dilatancy . . . . .	67
4.2.1	Strain Hardening and Stress Dependent Dilation Angle	67
4.2.2	Strain Hardening and Stress Dependent Dilation Coefficient . . . . .	68
4.3	Void Ratio Dependent Dilatancy . . . . .	68
4.3.1	Simulation of Toyoura Sand with Constant Elastic Stiffness	68
4.3.2	Simulation of Toyoura Sand with Mean Stress Dependent Stiffness . . . . .	70
<b>5</b>	<b>Results from Calculations</b>	<b>71</b>
5.1	Linear Elastic-Perfect Plastic Model . . . . .	71
5.1.1	Associated Flow . . . . .	71
5.1.2	Non-Associated Flow . . . . .	79
5.1.3	Loading and Safety Calculations . . . . .	81
5.2	Strain Hardening and Stress Dependent Dilatancy . . . . .	86
5.2.1	Strain Hardening and Stress Dependent Dilation Angle	86

5.2.2	Strain Hardening and Stress Dependent Dilation Coefficient . . . . .	90
5.3	Void Ratio Dependent Dilatancy . . . . .	94
5.3.1	Simulation of Toyoura Sand with Constant Elastic Stiffness	94
5.3.2	Simulation of Toyoura Sand with Mean Stress Dependent Stiffness . . . . .	98
<b>6</b>	<b>Conclusions and Recommendations for Further Work</b>	<b>103</b>
6.1	Summary and Conclusions . . . . .	103
6.2	Linear Elastic-Perfect Plastic Model . . . . .	104
6.2.1	Associated Flow in Single Material Point . . . . .	104
6.2.2	Non-Associated Flow in Single Material Point . . . . .	107
6.2.3	Loading and Safety Calculations . . . . .	107
6.3	Strain Hardening and Stress Dependent Dilatancy . . . . .	108
6.3.1	Strain Hardening and Stress Dependent Dilation Angle	108
6.3.2	Strain Hardening and Stress Dependent Dilation Coefficient . . . . .	110
6.4	Void Ratio Dependent Dilatancy . . . . .	111
6.4.1	Simulation of Toyoura Sand with Constant Elastic Stiffness	111
6.4.2	Simulation of Toyoura Sand with Mean Stress Dependent Stiffness . . . . .	112
6.5	Implemented Routines . . . . .	113
6.5.1	Modular programming . . . . .	113
6.5.2	Numerical methods . . . . .	113
6.6	Recommendations for Further Work . . . . .	114
	<b>Bibliography</b>	<b>115</b>
	Bibliography . . . . .	116
	<b>Appendix A Task Description</b>	<b>131</b>
	<b>Appendix B Mathematical Derivations</b>	<b>133</b>
B.1	Lode Angle . . . . .	133
B.2	Mohr–Coulomb Yield Surfaces in Haigh–Westergaard Coordinates	135

---

<b>Appendix C Material Independent Subroutines</b>	<b>139</b>
C.1 Main Subroutine . . . . .	139
C.2 Helper Subroutine . . . . .	142
<b>Appendix D Material Dependent Codes</b>	<b>147</b>
D.1 Fortran Subroutine . . . . .	147
D.2 MATLAB Script . . . . .	155
D.3 vars.f-module . . . . .	157
<b>Appendix E Documentation of Calculations</b>	<b>159</b>
E.1 Load-Displacement Curves . . . . .	159
E.2 Displacement-Factor of Safety Curves . . . . .	163
E.3 Shadings of Incremental Shear Strains . . . . .	167



# Chapter 1

## Introduction

### 1.1 Background

The choice of material model when simulating the behavior of soil, is of great importance in the use of Finite Element Analysis in geotechnical engineering. It is the very heart of the analysis. In general, soil exhibit complex behavior that includes effects from preconsolidation, dilation and contraction, softening, anisotropy and stress dependency. This complicates sound and correct modeling.

Today, an effective stress based soil model for soft Scandinavian clays is being developed at NTNU by PhD candidate Jon A. Rønningen, as part of the ongoing research project GeoFuture. This thesis is an extension of this project, applying some of the same principles. The implementation of the model has been carried out in close collaboration with Jon A. Rønningen.

### 1.2 Problem Formulation

The goal of this thesis is to implement an effective stress based soil model as a user-defined soil model into PLAXIS, applying the concept of modular programming in MATLAB and Fortran code. This concept is formulated by Rønningen (2014) and it is of interest that they are tested independently, by implementing the Drucker–Prager strength criterion. Further it is considered whether important aspects of undrained behavior of sand may be simulated by a few, quite simple elements from constitutive modeling.

Due to its simplicity, the Drucker–Prager model has been chosen for implementation. A smooth yield surface is attractive in programming, and the Drucker–Prager criterion has only one point where the surface is discontinu-

ous. The strength may be correlated to the Mohr–Coulomb criterion, thus the strength may be chosen to coincide for the two criteria. The Mohr–Coulomb model and some triaxial tests on Toyoura sand by Verdugo (1992) has been used for comparison to the implemented model.

### 1.3 Objectives

To achieve the goal of this thesis, three objectives are stated:

1. Implement a linear elastic-perfect plastic soil model by the use of modular programming
2. Implement effects of hardening, dilatancy and stress dependent stiffness into the model
3. Perform simulations with the model for consecutive comparison to existing models or real soil behavior

By reaching these objectives it should be possible to consider how modular programming may be used in constitutive soil modeling.

### 1.4 Limitations and Approach

The presentation will focus on principles giving an understanding of the material models. A large number of books and articles could have been studied, each with another approach to the field. In agreement with the supervisor, the literature study was limited to only the sources needed for implementing the model. Equations and derivations will be given in such a detail that the practical and numerical consequences are enlightened. Some theory of how to implement models in numerical schemes will also be presented. Further, Finite Element Method and continuum mechanics should be known for the reader. This is however presented in agreement with supervisor in order to gather all definitions used. In literature several different definitions for the same measure are found, so the reader may also check what definitions that are used as basis.

The first and second objective are met by implementing the Drucker–Prager model by modular programming. This involved implementing a linear elastic-perfect plastic model at first, then adding more features. Comparisons are made throughout the work by calculations in PLAXIS. Due to limited time, only one hardening relation and two formulations for dilatancy were implemented, yet several others could have been used. Only a few sets of parameters could be tested due to time limitation.

With the development of the model to include hardening and dilatancy it is possible to compare the model to real soil behavior. Stress dependent stiffness was also considered and is a common effect that are prominent when simulating soil over a wide stress range. A selection have been made and is restricted to some high-quality undrained triaxial tests on Toyoura sand by Verdugo (1992). These are used as reference for triaxial test simulations with the model.

## 1.5 Relevant Literature

For constitutive modeling and the elasto-plastic framework, lecture notes and background material from courses given at NTNU by Nordal (2012a) and Hopperstad and Børvik (2013) constitute the basis. The theory of the Mohr–Coulomb criterion is based on the presentation by Nordal (2012b), while the Drucker–Prager criterion was proposed by Drucker and Prager (1952) and presented in more detail by Nordal (2012a). Been and Jefferies (1985) proposed a state parameter for sands that are presented, together with an application of it, as described in an article by Muir Wood et al. (1994). These two articles are the original articles proposing their respective contents. Some numerical methods are presented and the theoretical basis are taken from both Cook et al. (2002), Kreyszig (2006) and Hopperstad and Børvik (2013).

## 1.6 Structure of the Report

Chapter 2 presents the necessary theoretical foundation for implementation of the model, including continuum mechanics and the elasto-plastic framework, Mohr–Coulomb and Drucker–Prager strength criteria, the mentioned state parameters and an application of it. Necessary assumptions will be clarified. Sections 2.1-2.5 are partially based on an earlier presentation by the author, from the course TBA4510 - Geotechnical Engineering, Specialization Project.

In chapter 3, the architecture of the implementation is presented. This is chronologically presented following the progress throughout the semester.

A description of the calculations for validations and simulations of Toyoura sand is presented in chapter 4. All necessary data to verify the calculations are presented. In chapter 5, results from the calculations are presented. The presentation in both chapters follows the chronological progress of the work.

Chapter 6 summarizes, discuss and concludes based on results of the calculations. Recommendations for further work are made at the end of the chapter.





# Chapter 2

## Theoretical Foundation

In this chapter, the theoretical foundation will be summarized. Necessary theory for implementing an effective stress based soil model is presented. This includes principles of constitutive modeling, the elasto-plastic framework and Mohr–Coulomb and Drucker–Prager strength criteria. At the end, a state parameter for sand, an application of it and numerical methods needed for the implementation will be presented.

### 2.1 The Finite Element Method

The Finite Element Method (FEM) or Finite Element Analysis (FEA) is a numerical method for solving a variety of engineering problems. This section will briefly summarize some of the most important key assumptions in Finite Element Method and point to the role of constitutive modeling.

#### 2.1.1 Key Assumptions and Principles of Finite Element Method

Important advantages of the finite element method are the ability to calculate both deformations and mobilization in one calculation rather than in two, like it's done in classical geotechnics, and has the possibility for coupled analysis of deformation and flow. Due to it being a numerical method, FEM introduces errors, but by proper use, these errors may be limited. The risk of defining the problem wrongly or choosing an insufficient material model for the relevant purpose, is always present, though (Nordal, 2012b; Cook et al., 2002).

The very name of the method reveals an important principle. The given problem is split into small, yet finite elements with special properties and then assembled, building up a model of the problem. Elements connect in

points called nodes, forming a mesh. In each node a set of degrees of freedom (DOF) is defined. If the element is used in structural or geotechnical problems, the element will simulate a displacement field and the global structure or soil volume has a certain stiffness and strength (Cook et al., 2002).

The displacement field is interpolated by the values in the nodes and some assumed shape polynomial functions. There is one shape function for each node. Shape functions are restricted to be unity in the specific node and zero in all other nodes. Thus the interpolated value in each node equals the value of the DOF in the node. Due to each node imposing another restriction of the shape function, a higher order element with more nodes results in shape functions of higher degree. The shape functions are established mathematically in a matrix  $\mathbf{N}$ , the nodal displacements are gathered in a vector  $\mathbf{v}$ , and the displacement field  $\mathbf{u}$  is thereby interpolated by:

$$\mathbf{u} = \mathbf{N}\mathbf{v} \quad \text{or incrementally} \quad \Delta\mathbf{u} = \mathbf{N}\Delta\mathbf{v} \quad (2.1)$$

Strains are derived from differentiating the displacement field and gathered in a vector  $\boldsymbol{\varepsilon}$ . The differentiation operator  $\boldsymbol{\delta}$  is dependent on the choice of element (Cook et al., 2002). Strains are expressed by a deformation matrix  $\mathbf{B}$  as:

$$\Delta\boldsymbol{\varepsilon} = \boldsymbol{\delta}\Delta\mathbf{u} = \mathbf{B}\Delta\mathbf{v} \quad \text{where} \quad \mathbf{B} = \boldsymbol{\delta}\mathbf{N} \quad (2.2)$$

Stresses  $\boldsymbol{\sigma}$  are related to the strains through a constitutive matrix  $\mathbf{D}$ . These relations are usually a stress dependent matrix in geotechnical engineering, raising the demand for non-linear finite element analysis and incremental calculations (Nordal, 2012b). Element stiffness  $\mathbf{k}$  is dependent on the constitutive matrix and the differentiated shape function matrix. It is referred to Cook et al. (2002) or other FEM-literature for the derivation:

$$\mathbf{k} = \int \mathbf{B}^T \mathbf{D} \mathbf{B} dV \quad (2.3)$$

As equation (2.3) is dependent on the constitutive matrix  $\mathbf{D}$ , the importance of obtaining a reliable and realistic constitutive matrix is underlined. At last stiffness of each element are gathered in to a system stiffness matrix connecting the external forces to global DOFs.

### 2.1.2 Finite Element Software

General-purpose FEM-software such as Abaqus FEA and COMSOL Multiphysics are available and relevant for geotechnical applications. PLAXIS is a specialized finite element program developed for geotechnical engineering, thus the user does not need to pre-define as much as in general-purpose software.

The elements available in PLAXIS 2D are two triangles, a 6-noded and a 15-noded. Higher order elements give more accurate solutions, but are more computational demanding. For accurate failure load predictions the 15-noded element is necessary and due to the power of today's computers, it is in general preferred for all calculations (Nordal, 2012b). In PLAXIS compressive stresses and strains are defined as negative, in accordance with other FEM-software (PLAXIS, 2012a).

## 2.2 Continuum Mechanics

Modeling of materials requires a set of mathematical equations that establish a constitutive model. For solid materials this is described by continuum mechanics.

### 2.2.1 Key Assumptions in Soil Modeling

Both stresses and strains in a material point may be represented as tensors with components in three orthogonal  $x_1$ ,  $x_2$  and  $x_3$ -directions, acting on three orthonormal planes in space. Stresses in three directions on three planes gives a total of nine independent stress and strain components, which may be represented by a 3x3-matrix. Due to moment equilibrium the coupled stress terms, e.g.  $\sigma_{12}$  and  $\sigma_{21}$ , must be equal, hence the stress matrix is symmetric. The stress tensor may thereby be represented as a 6x1-vector. Also the strain matrix may be written as a 6x1-vector (PLAXIS, 2012a). The stress and strain vectors are:

$$\sigma_{ij} = \boldsymbol{\sigma} = \left( \sigma_{11} \quad \sigma_{22} \quad \sigma_{33} \quad \sigma_{12} \quad \sigma_{23} \quad \sigma_{31} \right)^T \quad (2.4)$$

$$\begin{aligned} \varepsilon_{ij} = \boldsymbol{\varepsilon} &= \left( \varepsilon_{11} \quad \varepsilon_{22} \quad \varepsilon_{33} \quad \varepsilon_{12} \quad \varepsilon_{23} \quad \varepsilon_{31} \right)^T \quad (2.5) \\ &= \left( \varepsilon_{11} \quad \varepsilon_{22} \quad \varepsilon_{33} \quad \frac{1}{2}\gamma_{12} \quad \frac{1}{2}\gamma_{23} \quad \frac{1}{2}\gamma_{31} \right)^T \end{aligned}$$

As seen above, bold font is used to indicate vectors or matrices, but indexes in subscript also may be used. The number of subscript indexes corresponds

to the order of the tensor represented. Tensors are quantities described by multidimensional arrays. The description of a vector or matrix is dependent on the choice of basis, resulting in different expressions for the vectors and matrices for different choices of basis. Hence, for a stress analysis it is necessary to find measures that are independent of the choice of basis. Tensors transform according to given rules under coordinate transformation, while invariants are independent of any transformation (Nordal, 2012a; Hopperstad and Børvik, 2013).

In structural engineering, tension stresses and strains are defined as positive, which has been adopted in FEM-software like PLAXIS. In this thesis the classical geotechnical convention with positive compressive stresses and strains will be adopted.

Effective stress are usually denoted with a prime to distinguish it from total stresses. As the implementation of this thesis consider an effective stress based model, the prime is omitted in notations except where distinction is strictly necessary. Pore pressures in soil may be divided into excess pore pressure caused by undrained loading and the steady state pore pressure, giving:

$$p_w = p_{\text{excess}} + p_{\text{steady}} \quad (2.6)$$

$$\dot{p}_w = \dot{p}_{\text{excess}} \quad (2.7)$$

where the dot indicates the rate, or time derivative.

### 2.2.2 Stresses and Stress Invariants

The stresses are denoted as  $\sigma_{ij}$ , where  $i$  gives the surface of where the stress acts and  $j$  gives the direction of the stress. Due to being invariants, the eigenvalues of the matrix are of interest to evaluate the stress state due to being invariants. The eigenvalue problem of the  $\boldsymbol{\sigma}$ -matrix and its non-trivial solution reads:

$$(\boldsymbol{\sigma} - \sigma \cdot \mathbf{I}) \cdot \mathbf{n} = \mathbf{0} \quad (2.8a)$$

$$\det(\boldsymbol{\sigma} - \sigma \cdot \mathbf{I}) = 0 \quad (2.8b)$$

where  $\mathbf{I}$  is the identity matrix. Solving the non-trivial solution of equation (2.8b) results in a third order characteristic equation:

$$\sigma^3 - I_1\sigma^2 - I_2\sigma - I_3 = 0 \quad (2.9)$$

Equation (2.9) gives three real roots, the principal stresses  $\sigma_1$ ,  $\sigma_2$  and  $\sigma_3$ , usually ordered such that  $\sigma_1$  is the maximum compressive stress and  $\sigma_3$  is the

minimum compressive stress. The coefficients of the equation may be derived and expressed as:

$$\begin{aligned} I_1 &= \sigma_{11} + \sigma_{22} + \sigma_{33} \\ I_2 &= -\sigma_{11}\sigma_{22} - \sigma_{22}\sigma_{33} - \sigma_{33}\sigma_{11} + \sigma_{12}^2 + \sigma_{23}^2 + \sigma_{31}^2 \\ I_3 &= \det(\boldsymbol{\sigma}) \end{aligned} \quad (2.10)$$

The three principal stresses and any functions of them are invariants, they are independent of the choice of basis (Nordal, 2012a). The plane normal  $\mathbf{n}_i$  of the planes where the principal stresses  $\sigma_i$  act may be found from equation (2.8a). As the normal vectors  $\mathbf{n}_i$  forms an orthonormal basis, these may be chosen as the basis for  $\boldsymbol{\sigma}$ , giving a matrix with the principal stresses on the diagonal and zero shear stresses. Hence the stress invariants are:

$$\begin{aligned} I_1 &= \sigma_1 + \sigma_2 + \sigma_3 \\ I_2 &= -\sigma_1\sigma_2 - \sigma_2\sigma_3 - \sigma_3\sigma_1 \\ I_3 &= \det(\boldsymbol{\sigma}) = \sigma_1\sigma_2\sigma_3 \end{aligned} \quad (2.11)$$

A widely used stress measure in geotechnical practice, is the isotropic mean stress  $p$ , a scaled version of the first stress invariant:

$$p = \frac{1}{3}I_1 = \frac{1}{3}(\sigma_{11} + \sigma_{22} + \sigma_{33}) \quad (2.12)$$

### 2.2.3 Deviatoric Stresses and Deviatoric Stress Invariants

Deviatoric stresses are defined as:

$$\mathbf{s} = \boldsymbol{\sigma} - p\mathbf{I} \quad \text{or} \quad (2.13a)$$

$$s_{ij} = \sigma_{ij} - \delta_{ij}p \quad (2.13b)$$

where the Kronecker delta function is used. It is defined as:

$$\delta_{ij} = \begin{cases} 1 & \text{if } i = j \\ 0 & \text{if } i \neq j \end{cases}$$

The principal stresses and the stress invariants for the deviatoric stress  $\mathbf{s}$  may be calculated in the same manner as for the full stress state  $\boldsymbol{\sigma}$ , such that the eigenvalue problem is:

$$(\mathbf{s} - s \cdot \mathbf{I}) \cdot \mathbf{n} = \mathbf{0} \quad (2.14a)$$

$$\det(\mathbf{s} - s \cdot \mathbf{I}) = 0 \quad (2.14b)$$

resulting in a characteristic equation of third order:

$$s^3 - J_1 s^2 - J_2 s - J_3 = 0 \quad (2.15)$$

The deviatoric stress invariants may be derived and are written out as:

$$\begin{aligned} J_1 &= s_{11} + s_{22} + s_{33} \equiv 0 \\ J_2 &= -s_{11}s_{22} - s_{22}s_{33} - s_{33}s_{11} + s_{12}^2 + s_{23}^2 + s_{31}^2 \\ J_3 &= \det(\mathbf{s}) \end{aligned} \quad (2.16)$$

Due to the invariant properties, principal deviatoric stresses must simply be:

$$s_i = \sigma_i - p \quad \text{for } i = 1, 2, 3 \quad (2.17)$$

In many models the  $J_2$ -invariant plays a significant role. Other convenient expressions of  $J_2$  may be derived, such as:

$$\begin{aligned} J_2 &= \frac{1}{2} \mathbf{s}^T \mathbf{s} \\ &= \frac{1}{2} (s_{11}^2 + s_{22}^2 + s_{33}^2) + s_{12}^2 + s_{23}^2 + s_{31}^2 \\ &= \frac{1}{2} (s_1^2 + s_2^2 + s_3^2) \\ &= -s_1 s_2 - s_2 s_3 - s_3 s_1 \\ &= \frac{1}{6} [(\sigma_{11} - \sigma_{22})^2 + (\sigma_{22} - \sigma_{33})^2 + (\sigma_{33} - \sigma_{11})^2] + \sigma_{12}^2 + \sigma_{23}^2 + \sigma_{31}^2 \\ &= \frac{1}{6} [(\sigma_1 - \sigma_2)^2 + (\sigma_2 - \sigma_3)^2 + (\sigma_3 - \sigma_1)^2] \end{aligned} \quad (2.18)$$

In PLAXIS a deviatoric stress  $q$  is defined, also known as the equivalent stress or von Mises stress in structural engineering. This stress is related to  $J_2$  by:

$$q = \sigma_e = \sqrt{\frac{1}{2} [(\sigma_1 - \sigma_2)^2 + (\sigma_2 - \sigma_3)^2 + (\sigma_3 - \sigma_1)^2]} = \sqrt{3J_2} \quad (2.19)$$

For the special stress states of triaxial compression where  $\sigma_2 = \sigma_3$  and triaxial extension where  $\sigma_1 = \sigma_2$ ,  $q$  is reduced to a more commonly known expression in geotechnical practice:

$$q = |\sigma_1 - \sigma_3| \quad (2.20)$$

The full formulation of  $q$  from equation (2.19) will be used in this thesis unless anything else is explicitly stated.

### 2.2.4 Haigh-Westergaard Coordinates and Stress Space

To visualize stress states, paths and surfaces in stress space, it is useful to formulate a set of cylindrical coordinates in stress space. By selecting the hydrostatic axis as the longitudinal axis or cylindrical axis, it is possible to visualize planes of constant mean stress, so called deviatoric planes or  $\Pi$ -planes (Hopperstad and Børvik, 2013). The stress space and a  $\Pi$ -plane are shown in Figure 2.1. These planes will reduce to a set of polar coordinates.

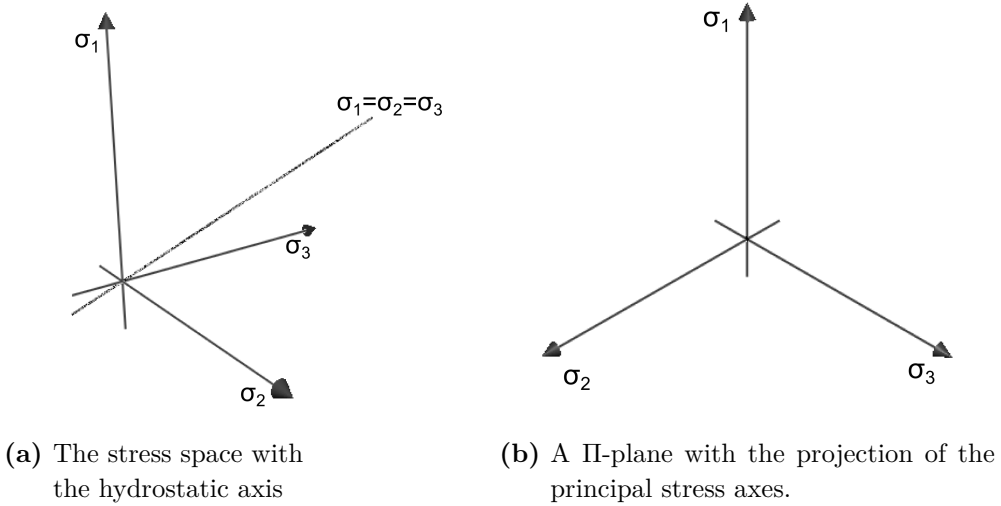


**Figure 2.1:** Principal stress space.

A derivation of these coordinates is shown in Appendix B.1. A vector in the  $\Pi$ -plane will be the deviatoric part of the stress state, hence must the radial distance from the axis be the magnitude of the deviatoric vector. The position at the longitudinal axis and the Lode angle may be defined in several ways, yet in this thesis the coordinates are defined as:

$$\xi = I_1/\sqrt{3} \quad (2.21a)$$

$$\rho = \sqrt{\mathbf{s} \cdot \mathbf{s}} = \sqrt{s_1^2 + s_2^2 + s_3^2} = \sqrt{2J_2} \quad (2.21b)$$

$$\cos 3\theta = \frac{3\sqrt{3} \cdot J_3}{2\sqrt{J_2^3}} \quad \text{for } \theta \in [0, \pi/3] \quad (2.21c)$$

The expression for  $\cos 3\theta$  may be verified to always be within the interval  $[-1, 1]$  for all values of  $J_2$  and  $J_3$  (Nordal, 2012a). Hence, all solutions of equation (2.21c) give  $3\theta \in [0, \pi]$ . As the cosine function is periodic,  $3\theta + 2\pi n$

are all solutions of equation (2.21c). Thus,  $\theta + 2\pi n/3$  are all solutions resulting in different values for  $\cos \theta$ . Ordered according to  $\sigma_1 > \sigma_2 > \sigma_3$ , the relations between the Haigh-Westergaard coordinates in stress space,  $(\xi, \rho, \theta)$ , and the principal stresses are:

$$\begin{bmatrix} \sigma_1 \\ \sigma_2 \\ \sigma_3 \end{bmatrix} = \frac{\xi}{\sqrt{3}} \begin{bmatrix} 1 \\ 1 \\ 1 \end{bmatrix} + \rho \sqrt{\frac{2}{3}} \begin{bmatrix} \cos \theta \\ \cos(\theta - \frac{2\pi}{3}) \\ \cos(\theta + \frac{2\pi}{3}) \end{bmatrix}, \quad \text{for } \theta \in [0, \pi/3] \quad (2.22)$$

For the presented definition of the Lode angle  $\theta$ ,  $\theta = 0^\circ$  correspond to triaxial compression conditions (along the projection of the  $\sigma_1$ -axis), while  $\theta = 60^\circ$  correspond to triaxial extension conditions (along the projection negative extension of the  $\sigma_3$ -axis).

The reader should be aware of that there exists other expressions of the Lode angle defined for other domains. Attention must be paid when comparing expressions using the Lode angle.

### 2.2.5 Strains and Strain Invariants

Applying the sign convention of classical geotechnical engineering, the infinitesimal strain tensor  $\varepsilon_{ij}$  of a body with a reference position vector  $\mathbf{x}$  when a displacement field  $\mathbf{u}$  is imposed is (Hopperstad and Børvik, 2013):

$$\varepsilon_{ij} = -\frac{1}{2} \left( \frac{\partial u_i}{\partial x_j} + \frac{\partial u_j}{\partial x_i} \right) \quad (2.23)$$

As for the stress tensor, the eigenvalues of the strain tensor may be solved from the eigenvalue problem:

$$(\boldsymbol{\varepsilon} - \varepsilon \cdot \mathbf{I}) \cdot \bar{\mathbf{x}} = \mathbf{0} \quad (2.24a)$$

$$\det(\boldsymbol{\varepsilon} - \varepsilon \cdot \mathbf{I}) = 0 \quad (2.24b)$$

where  $\bar{\mathbf{x}}$  is the orthonormal basis for the eigenvectors or principal axes of strain. This results in a characteristic equation of third order:

$$\varepsilon^3 - I_1^\varepsilon \varepsilon^2 - I_2^\varepsilon \varepsilon - I_3^\varepsilon = 0 \quad (2.25)$$

where invariants are:

$$\begin{aligned} I_1^\varepsilon &= \varepsilon_{11} + \varepsilon_{22} + \varepsilon_{33} \\ I_2^\varepsilon &= -\varepsilon_{11}\varepsilon_{22} - \varepsilon_{22}\varepsilon_{33} - \varepsilon_{33}\varepsilon_{11} + \varepsilon_{12}^2 + \varepsilon_{23}^2 + \varepsilon_{31}^2 \\ I_3^\varepsilon &= \det(\boldsymbol{\varepsilon}) \end{aligned} \quad (2.26)$$



Now, consider a rectangular body of which the sides are directed along the principal axes of strain with original lengths  $x_1^0, x_2^0, x_3^0$ . By applying common formulations of engineering strains, the deformed lengths are  $x_1^0(1 + \varepsilon_1), x_2^0(1 + \varepsilon_2), x_3^0(1 + \varepsilon_3)$ . The volumetric strain is then:

$$\begin{aligned}\varepsilon_V &= \frac{V - V_0}{V_0} = \frac{x_1^0(1 + \varepsilon_1)x_2^0(1 + \varepsilon_2)x_3^0(1 + \varepsilon_3) - x_1^0x_2^0x_3^0}{x_1^0x_2^0x_3^0} \\ &= (1 + \varepsilon_1)(1 + \varepsilon_2)(1 + \varepsilon_3) - 1 = \varepsilon_1 + \varepsilon_2 + \varepsilon_3 = I_1^\varepsilon\end{aligned}\quad (2.27)$$

where products of strain are neglected. The volumetric strain may also be referred to as  $\varepsilon_p$  to emphasize the relation to the mean stress  $p$ .

To separate volumetric deformation from deviatoric deformations, deviatoric strain invariants are developed for strain as well as for stress:

$$\mathbf{e} = \boldsymbol{\varepsilon} - \frac{\varepsilon_V}{3}\mathbf{I} \quad \text{or} \quad (2.28a)$$

$$e_{ij} = \varepsilon_{ij} - \frac{\varepsilon_V}{3}\delta_{ij} \quad (2.28b)$$

Thus, the deviatoric strain invariants are:

$$\begin{aligned}J_1^\varepsilon &= e_{11} + e_{22} + e_{33} \equiv 0 \\ J_2^\varepsilon &= -e_{11}e_{22} - e_{22}e_{33} - e_{33}e_{11} + e_{12}^2 + e_{23}^2 + e_{31}^2 \\ J_3^\varepsilon &= \det(\mathbf{e})\end{aligned}\quad (2.29)$$

In PLAXIS, deviatoric strain  $\gamma_s$  is calculated as (PLAXIS, 2012a):

$$\begin{aligned}\gamma_s &= \sqrt{\frac{2}{3} \left[ \left( \varepsilon_{11} - \frac{\varepsilon_V}{3} \right)^2 + \left( \varepsilon_{22} - \frac{\varepsilon_V}{3} \right)^2 + \left( \varepsilon_{33} - \frac{\varepsilon_V}{3} \right)^2 + \frac{1}{2}(\gamma_{12}^2 + \gamma_{23}^2 + \gamma_{31}^2) \right]} \\ &= \sqrt{\frac{2}{3}} \cdot 2J_2^\varepsilon = \frac{\gamma_{oct}}{\sqrt{2}}\end{aligned}\quad (2.30)$$

where  $\gamma_{oct}$  is the octahedral shear strain as defined by Nordal (2012a).

## 2.3 Elasto-Plastic Soil Models

For simple elasto-plastic models, one may say that elasticity governs the behavior up to failure while plasticity governs the behavior at failure. In more advanced models plasticity may play an important role also from the start of loading. Combining the theories constitutes a powerful method of describing material response.

### 2.3.1 Elasto-Plasticity: Strain Decomposition

Material response of elasto-plastic models is partly reversible and partly irreversible. Thus, the strain is decomposed into recoverable elastic strains,  $\epsilon^e$ , and irrecoverable plastic strains,  $\epsilon^p$ . Elastic strains are uniquely defined by the stress situation, e.g. by Hooke's law, while plastic strains are dependent on the stress and strain history of the material, hence not unique. This implies a need for defining the relations between the stress and the plastic strain on rate form (Hopperstad and Børvik, 2013). Thus, the total strains in elasto-plastic models are the sum of elastic and plastic strains:

$$\epsilon = \epsilon^e + \epsilon^p \quad (2.31)$$

For the special case of a one-dimensional linear elastic-perfect plastic material model, decomposition of strains is shown in Figure 2.2.

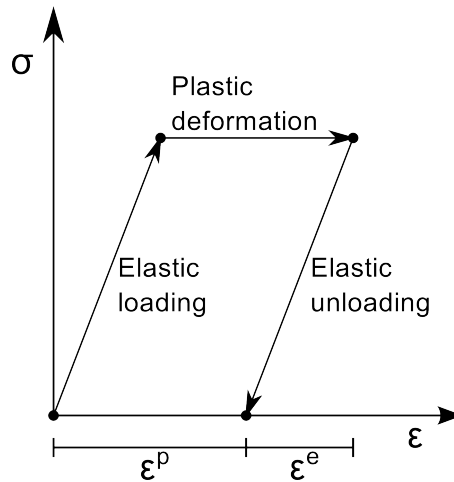


**Figure 2.2:** Decomposition of total strains into elastic and plastic strains. For simplicity perfect plasticity is illustrated. (Nordal, 2012b, Figure 6.1b)

### 2.3.2 Elasticity: Linear Elasticity

Elastic materials are characterized by reversible deformations, path independence, no dissipation of mechanical energy and rate independence. Further, a subset of elastic materials, hyperelastic materials, are materials where there exists an elastic potential function  $U_0$ , so that stresses are connected through

(Hopperstad and Børvik, 2013):

$$\sigma_{ij} = \frac{\partial U_0}{\partial \varepsilon_{ij}} \quad \text{for } i, j = 1, 2, 3 \quad (2.32)$$

The operator relating strain and stress, two second order tensors, must be of fourth order. The generalized Hooke's law is stated as (Hopperstad and Børvik, 2013):

$$\sigma_{ij} = \frac{\partial U_0}{\partial \varepsilon_{ij}} = D_{ijkl} \varepsilon_{kl} \quad \text{for } i, j, k, l = 1, 2, 3 \quad (2.33)$$

Due to differentiation order does not matter and symmetries of stress and strain, symmetries of the tensor  $D_{ijkl}$  arise:

$$\begin{aligned} D_{ijkl} &= \frac{\partial^2 U_0}{\partial \varepsilon_{ij} \partial \varepsilon_{kl}} = \frac{\partial^2 U_0}{\partial \varepsilon_{kl} \partial \varepsilon_{ij}} = D_{klij} \\ \sigma_{ij} = \sigma_{ji} &\implies D_{ijkl} = D_{jikl} \\ \varepsilon_{kl} = \varepsilon_{lk} &\implies D_{ijkl} = D_{ijlk} \end{aligned} \quad (2.34)$$

Thus,  $D_{ijkl}$ , may be written in a symmetric 6x6 matrix  $\mathbf{D}$ , with 21 independent constants.

In general, as the stress and strain tensors are dependent of the choice of basis, the operator relating those must also be dependent of the choice of basis. However, if the elastic material have no preferred directions, all constants of the tensor  $D_{ijkl}$  must be independent of the choice of basis, which is the case for an isotropic elastic material (Hopperstad and Børvik, 2013).

Hopperstad and Børvik (2013) show that Hooke's law for an isotropic material may be written as:

$$\sigma_{ij} = K \varepsilon_V \delta_{ij} + 2G e_{ij} \quad (2.35)$$

where the modules  $K$  and  $G$  are functions of Young's modulus  $E$  and Poisson's ratio  $\nu$ :

$$K = \frac{E}{3(1-2\nu)} \quad (2.36a)$$

$$G = \frac{E}{2(1+\nu)} \quad (2.36b)$$

Thus, the relations between the hydrostatic and deviatoric parts may be stated as:

$$p = \frac{1}{3} \sigma_{ii} = \frac{1}{3} \cdot 3K \varepsilon_V + \frac{2}{3} G e_{ii} = K \varepsilon_V \quad (2.37a)$$

$$s_{ij} = K \varepsilon_V \delta_{ij} + 2G e_{ij} - p \delta_{ij} = 2G e_{ij} \quad (2.37b)$$

Equation (2.37) shows an important consequence of isotropic elasticity. The deviator stress is a pure proportional scaling of the deviator strain. Such a scaling does not influence the principal directions. Any hydrostatic contribution cancels each other and the orientation of a principal stress plane must be independent of this. Thus, the stress and strain have the same principal directions for isotropic elasticity, they are coaxial (Nordal, 2012a). This implies that also stress and stress increments are coaxial for isotropic elasticity.

By the decomposition it follows that any change in only hydrostatic stress, only results in volumetric strain change, and likewise for deviatoric stresses. For soils this behavior is not correct due to dilatancy effects. However, by coupling elasticity with plasticity, the dilatancy effects may be captured unless the dilatancy is substantial even in elastic regions (Nordal, 2012a).

### 2.3.3 Elasticity: Nonlinear Elasticity

Nonlinear elasticity may model the elastic strains of soil more correctly than linear elasticity. Modules for a hyperelastic material may be derived from equation (2.34). By finding an elastic potential function  $U_0$  or its complementary strain energy function  $U_c$ , modules depending of the stress level may be established.

As the strain energy must be unique and independent of loading history, Nordal (2012a) showed that the only dependencies that may exist are when the shear modulus are dependent on deviatoric stress and when the bulk modulus are dependent of the hydrostatic stress. However, laboratory results often exhibit a mean stress dependency of the shear modulus. Problems may arise if a mean stress dependent shear modulus is used. In a closed loop, energy may then end up being generated, hence violating thermodynamic laws. This may not be a huge problem for monotonically increasing static loads, but may cause severe troubles for un-/reloading loops, dynamic and cyclic loading.

### 2.3.4 Plasticity: Yield Criteria

As opposed to elasticity, plasticity theory is characterized by irreversible deformations, path dependence and energy dependence, yet still no rate effects as any viscous effects are not included (Hopperstad and Børvik, 2013). Materials subjected to loading will evolve plastic strains when the loading exceeds a yield limit. The yield limit may either be a threshold or the plastic strains may gradually increase, without any sharp limit. The yield criterion is defined

mathematically by a yield surface in stress space. Further, hardening are often included by a single or a set of hardening variables  $\kappa$ , thus the surface may or may not be fixed. An example of a yield surface is shown in Figure 2.3 and the surface  $F$  is given by:

$$F = F(\boldsymbol{\sigma}, \kappa) = 0 \quad (2.38)$$

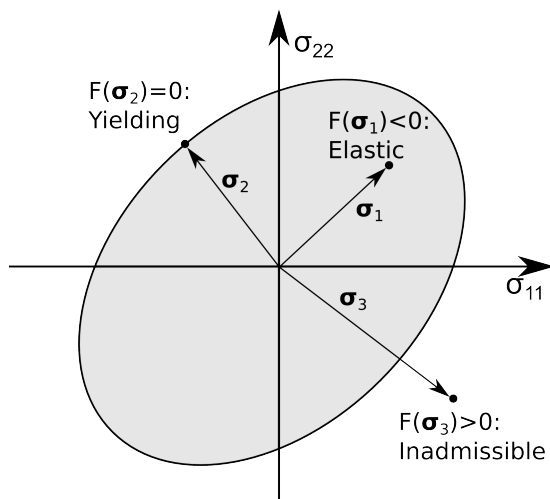


**Figure 2.3:** Sketch of a yield surface. (Hopperstad and Børvik, 2013, Figure 7-1)

For stress situations where  $F(\boldsymbol{\sigma}, \kappa) < 0$ , the material response is elastic, while  $F(\boldsymbol{\sigma}, \kappa) = 0$  yields plastic deformations. A stress situation where  $F(\boldsymbol{\sigma}, \kappa) > 0$  is not allowed in elasto-plastic models. If no hardening is incorporated in the model, as for a perfect plastic Mohr–Coulomb model, infinite plastic strains develop when attempting to load a stress increment at the yield limit. This implies no stiffness and that particular yield limit is then a failure state, giving a failure surface.

The initial part of a loading history may be within an elastic region, or plastic strains may evolve even from an initial stress state.

### 2.3.5 Plasticity: Flow Rule

The development of plastic strains is defined by the plastic flow rule. For the general case, the plastic flow is defined by a plastic potential function  $Q = Q(\boldsymbol{\sigma}) = 0$ . The infinitesimal change in plastic strains is then (Hopperstad and Børvik, 2013):

$$d\varepsilon_{ij}^p = d\lambda \frac{\partial Q}{\partial \sigma_{ij}} \quad (2.39)$$

The magnitude of the plastic strain increment is determined by the scalar  $d\lambda$ . The scalar will be further described in section 2.3.6.

Further, the flow rule states direction of plastic flow is normal to the plastic potential function. If the plastic potential function  $Q$  is defined by the yield function  $F$ , the flow rule is associated. Materials that obeys Drucker's postulate of material stability may be shown to obey associated flow. The postulate requires the flow to be normal to the yield surface and the yield surface to be convex. As soils violate Drucker's postulate, they are considered not to be a subset of the stable, work hardening materials obeying the postulate (Nordal, 2012a).

An associated flow rule is often performing well for metals and alloys, yet not on soils. This is due to the normality overestimates volume change. As a remedy the dilation angle is introduced, giving a plastic potential surface that relates plastic flow to other parameters than those defining the yield surface (Nordal, 2012b).

A consequence of equation (2.39) is that the plastic strain increment is solely dependent on the stress state, not the stress increment. Further, the change in plastic parameter, only scales the plastic strain vector. While the elastic strain increment and the stress increment are coaxial, the plastic strain increment and the stress are coaxial.

### 2.3.6 Plasticity: Hardening Rule

The hardening rule gives a relation determining the magnitude of the scalar  $d\lambda$  in equation (2.39). Hardening processes may be either work hardening or strain hardening. While work hardening is based on dissipation of work during the process of expanding the yield surface, strain hardening connects the plastic strains directly to a hardening parameter,  $\kappa$ . Hardening may either be isotropic, giving an isotropic expansion or collapse of the yield surface, or it may be kinematic, giving a translation of the yield surface. A combination of the two also exist (Nordal, 2012a).

The focus here is strain hardening. Work hardening may however be considered in a similar manner. During plastic flow, the yield function must always remain  $F = 0$ . Thus, the change in the yield function is zero:

$$dF = \left( \frac{\partial F}{\partial \sigma_{ij}} \right)^T d\sigma_{ij} + \frac{\partial F}{\partial \kappa} d\kappa = 0 \quad (2.40)$$

This is known as the consistency condition for plastic loading (Nordal, 2012a). Equation (2.40) connects incremental stress change  $d\boldsymbol{\sigma}$  to incremen-

tal change in the hardening parameter  $d\kappa$ . The hardening parameter may be related to the plastic parameter through:

$$\left(\frac{\partial F}{\partial \sigma_{ij}}\right)^T d\sigma_{ij} + \frac{\partial F}{\partial \kappa} \frac{d\kappa}{d\lambda} d\lambda = 0 \quad \text{or} \quad (2.41a)$$

$$\left(\frac{\partial F}{\partial \sigma_{ij}}\right)^T d\sigma_{ij} + \frac{\partial F}{\partial \kappa} \frac{d\kappa}{d\varepsilon^p} \frac{d\varepsilon^p}{d\lambda} d\lambda = 0 \quad (2.41b)$$

Now  $d\lambda$  is related to  $d\boldsymbol{\sigma}$ . The relations giving  $d\kappa/d\varepsilon^p$  or  $d\kappa/d\lambda$  may be taken from laboratory tests and the plastic strain scalar may be calculated as:

$$d\varepsilon^p = |d\varepsilon^p| = \sqrt{(d\varepsilon^p)^T \cdot d\varepsilon^p} = d\lambda \sqrt{\left(\frac{\partial Q}{\partial \boldsymbol{\sigma}}\right)^T \frac{\partial Q}{\partial \boldsymbol{\sigma}}} \quad (2.42)$$

By solving equation (2.41b) for  $d\lambda$ , the magnitude of the plastic strains may be calculated. For strain hardening the scalar is determined by:

$$d\lambda = \frac{1}{\frac{\partial F}{\partial \kappa} \frac{d\kappa}{d\varepsilon^p} \frac{d\varepsilon^p}{d\lambda}} \left(\frac{\partial F}{\partial \boldsymbol{\sigma}}\right)^T d\boldsymbol{\sigma} = \frac{1}{A} \left(\frac{\partial F}{\partial \boldsymbol{\sigma}}\right)^T d\boldsymbol{\sigma} \quad (2.43)$$

where  $A$  is a plastic resistance number. Equation (2.43) is valid for work hardening as well, with another expression for the plastic resistance number (Nordal, 2012a). When approaching failure,  $A$  reduces to zero and, theoretically, infinite plastic strains arise. The fact that  $d\lambda$  diverges when approaching failure causes trouble in the implementation into computer codes. To overcome these problems, another expression may be derived, not resulting in  $d\lambda$  diverging even when  $A = 0$ . Here, the expression are only reproduced and it is referred to Nordal (2012a) for the derivation:

$$d\lambda = \frac{\left(\frac{\partial F}{\partial \boldsymbol{\sigma}}\right)^T \mathbf{D} d\varepsilon}{A + \left(\frac{\partial F}{\partial \boldsymbol{\sigma}}\right)^T \mathbf{D} \left(\frac{\partial Q}{\partial \boldsymbol{\sigma}}\right)} \quad (2.44)$$

It may be shown from equation (2.44) that the plastic parameter always  $d\lambda$  are positive for any plastic increment, softening and hardening, and zero for any elastic increment (Nordal, 2012a).

### 2.3.7 Elasto-Plasticity: The Constitutive Matrix

As the elastic strains are uniquely defined by the elastic constitutive matrix  $\mathbf{D}$ , the infinitesimal total strain is:

$$d\boldsymbol{\varepsilon} = d\boldsymbol{\varepsilon}^e + d\boldsymbol{\varepsilon}^p = \mathbf{D}^{-1} d\boldsymbol{\sigma} + d\lambda \frac{\partial Q}{\partial \boldsymbol{\sigma}} \quad (2.45)$$

In some cases, the stress dependent non-linear constitutive matrix,  $\mathbf{D}_{ep}$ , may be established analytically and used in the calculation of the stiffness matrix of an element. The formulation of the plastic parameter  $d\lambda$  from equation (2.44) must be used to avoid divergence of the parameter. For the derivation, it is referred to Nordal (2012a). The result is the constitutive matrix to be used in calculation of the element stiffness matrix in equation (2.3):

$$\mathbf{D}_{ep} = \mathbf{D} - \frac{\mathbf{D} \left( \frac{\partial Q}{\partial \boldsymbol{\sigma}} \right) \left( \frac{\partial F}{\partial \boldsymbol{\sigma}} \right)^T \mathbf{D}}{\left[ A + \left( \frac{\partial F}{\partial \boldsymbol{\sigma}} \right)^T \mathbf{D} \left( \frac{\partial Q}{\partial \boldsymbol{\sigma}} \right) \right]} \quad (2.46)$$

where  $\mathbf{D}$  is the elastic stiffness matrix from Hooke's law and  $\mathbf{D}_{ep}$  is the elasto-plastic constitutive matrix where plastic stiffness is included.

## 2.4 Undrained Conditions

The undrained shear strength is controlled by the drained strength parameters, which gives the opportunity to establish an effective stress based constitutive model that applies to undrained situations. No dissipation of water yields the condition of no volume change, due to water is incompressible. This may be stated in several ways:

$$\Delta \varepsilon_V = 0 \quad (2.47a)$$

$$\Delta e = \Delta v = 0 \quad (2.47b)$$

This implies increased stiffness when no dissipation of water is allowed.

The inverted Hooke's law on time rate form may be established and formulated by both drained and undrained stiffness parameters relating elastic strain rate to the stress rate. By using Terzaghi's principle and equation (2.7), the effective and total stress are related by:

$$\dot{\sigma}'_{ij} = \dot{\sigma}_{ij} - \dot{p}_w \delta_{ij} \quad (2.48)$$



Assuming water to be slightly compressible, PLAXIS (2012a) gives the rate of excess pore pressure as:

$$\dot{p}_w = \frac{K_w}{n}(\dot{\varepsilon}_{xx}^e + \dot{\varepsilon}_{yy}^e + \dot{\varepsilon}_{zz}^e) \quad (2.49)$$

where  $n$  is porosity and  $K_w$  is bulk modulus of water. This gives a stiffness contribution from the bulk modulus of water into the constitutive matrix relation stress and strain. Volumetric stiffness from the water only contributes to the isotropic stiffness of the soil skeleton, not to the shear stiffness, in accordance with reality.

The inverted Hooke's on rate form may now be written in terms of both drained and undrained stiffness parameters, relating effective and total stress rates respectively to elastic strain rates. By introducing equations (2.48) and (2.49), drained and undrained stiffnesses may be related through:

$$E_u = 2G(1 + \nu_u) \quad \nu_u = \frac{\nu' + \mu(1 + \nu')}{1 + 2\mu(1 + \nu')} \quad (2.50)$$

$$\mu = \frac{1}{3n} \frac{K_w}{K'} \quad K' = \frac{E'}{3(1 - 2\nu')} \quad (2.51)$$

PLAXIS give the opportunity to use drained stiffness parameters for calculation of undrained stiffness parameters by equations (2.50) and (2.51).

For incompressible materials, the Poisson's ratio is  $\nu = 0.5$ , as can be seen from (2.51). However, this creates a singular stiffness matrix and a ratio giving a sufficiently high stiffness matrix while not causing any numerical difficulties must be chosen. The bulk stiffness  $K_w$  should thereby rather be understood as a numerical value related to the undrained stiffness of the soil, rather than the actual bulk modulus of water. An undrained stiffness in the order of 10 times the drained stiffness is not unusual (Nordal, 2012b).

## 2.5 The Mohr–Coulomb Criterion

As the Mohr–Coulomb criterion is a widely used strength criterion in geotechnical engineering, it is useful for comparison to other strength criteria. Equations that are necessary for later comparisons are presented here.

### 2.5.1 Defining Equations

The Mohr–Coulomb strength criterion is defined by failure shear stress  $\tau_f$  as proportional to effective stresses,  $\sigma$ . Thus, the strength parameters are the

friction angle  $\phi$  and either cohesion  $c$  or attraction  $a$ :

$$\tau_f = c + \sigma \cdot \tan \phi = (\sigma + a) \tan \phi \quad (2.52)$$

As earlier stated, prime is omitted as effective stress mark, as all stresses considered are effective stresses.

Mohr's circle defined by the maximum and minimum principal stresses,  $\sigma_1$  and  $\sigma_3$  respectively, is introduced where the Coulomb-criterion is tangent to the circle. Using simple geometry, the criterion of equation (2.52) may be written as:

$$R = \frac{1}{2}(\sigma_1 - \sigma_3) = \left( \frac{1}{2}(\sigma_1 + \sigma_3) + a \right) \sin \phi \quad (2.53)$$

After some mathematical operations the yield surface for the criterion may be formulated as:

$$F = (\sigma_1 + a) - N_f(\sigma_3 + a) = 0, \quad \text{where} \quad N_f = \frac{1 + \sin \phi}{1 - \sin \phi} \quad (2.54)$$

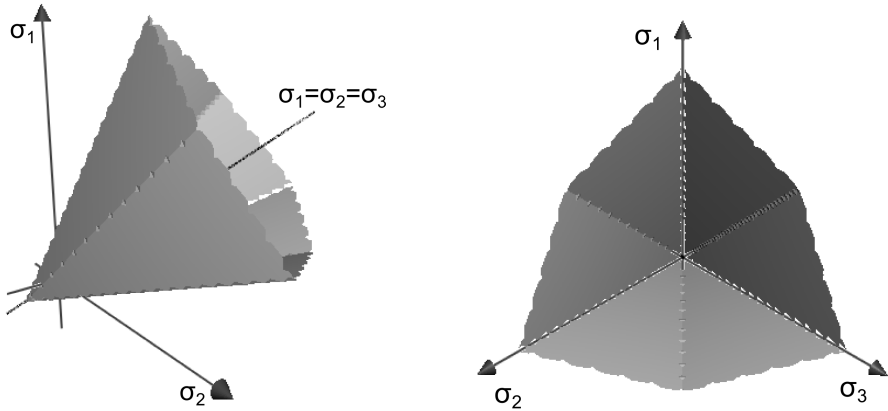
Equation (2.54) defines the failure surface of the Mohr–Coulomb criterion. It is seen that the Mohr–Coulomb strength criterion is independent of the intermediate stress,  $\sigma_2$ .

If the ordering of the principal stresses is removed, six possible stress states of a maximum and a minimum principal stress is possible, as both  $\sigma_1 > \sigma_2$  and  $\sigma_1 < \sigma_2$  are equally possible. The same applies for other combinations of stresses. As a result, six planes in principal stress space form the failure surfaces of a Mohr–Coulomb-model. The planes form a hexagonal pyramid along the hydrostatic axis in principal stress space, with the apex located in  $(\sigma_1, \sigma_2, \sigma_3) = (-a, -a, -a)$ , shown in Figure 2.4.

Due to the nonlinearity of the soil, the linearization of the failure stress into two parameters may cause errors. The two strength parameters should hence be considered as curve fitting parameters for the relevant stress interval rather than valid for the full range of soil behavior. Of the same reason, any attraction  $a$  should not be taken as a real tensile strength of the soil and caution should be made if tensile stresses are allowed.

## 2.5.2 Triaxial Test Formulation

In triaxial tests, the cell pressure is equal to  $\sigma_3$  for the shearing phase of the test, while the piston force applied is  $(\sigma'_1 - \sigma'_3)A = (\sigma_1 - \sigma_3)A$ . Thus, a formulation relating  $\sigma_3$  to  $\frac{1}{2}(\sigma_1 - \sigma_3)$  is useful for triaxial tests. From equation



(a) Yield surfaces in stress space. (b) Yield surfaces seen from hydrostatic axis.

**Figure 2.4:** Mohr–Coulomb yield surfaces.

(2.54) a new formulation may be obtained:

$$\frac{1}{2}[(\sigma_1 + a) - (\sigma_3 + a)] = \frac{1}{2}[N_f(\sigma_3 + a) - (\sigma_3 + a)] \quad (2.55)$$

$$\frac{1}{2}(\sigma_1 - \sigma_3) = S_f(\sigma_3 + a), \quad \text{where} \quad S_f = \frac{1}{2}(N_f - 1) = \frac{\sin \phi}{1 - \sin \phi} \quad (2.56)$$

### 2.5.3 Plane Strain Formulation

For plane strain conditions, a set of stress measures that uses the center of Mohr's circle,  $s$ , and the radius of Mohr's circle,  $t$ , may be useful. Mathematically, the stress measures  $s$  and  $t$  are:

$$s = \frac{\sigma_1 + \sigma_3}{2} = \frac{(\sigma_1 + a) + (\sigma_3 + a)}{2} - a = \frac{N_f + 1}{2}(\sigma_3 + a) - a \quad (2.57)$$

$$t = \frac{\sigma_1 - \sigma_3}{2} = \frac{(\sigma_1 + a) - (\sigma_3 + a)}{2} = \frac{N_f - 1}{2}(\sigma_3 + a) \quad (2.58)$$

Thus, the inclination of the Coulomb-line in a  $s$ - $t$ -plot is:

$$\frac{t}{s + a} = \frac{N_f - 1}{N_f + 1} = \frac{2 \sin \phi}{2} = \sin \phi \quad (2.59)$$

Now it is assumed that both minor and major principal stress lie in the plane strain-plane. For a cartesian basis of  $\mathbf{x}_1$ ,  $\mathbf{x}_2$ ,  $\mathbf{x}_3$ , the plane strain-plane is  $\mathbf{x}_1$ - $\mathbf{x}_3$ -plane. Yielding now only occur in this plane and the intermediate principal

stress  $\sigma_2$  is the out of plane stress. Using geometry of Mohr's circle, principal stresses may be obtained for a cartesian stress state with shear stresses:

$$\sigma_{1,3} = \frac{\sigma_{11} + \sigma_{33}}{2} \pm \sqrt{\left(\frac{\sigma_{11} - \sigma_{33}}{2}\right)^2 + \sigma_{13}^2} \quad (2.60)$$

Inserting this into equations (2.57) and (2.58) gives expressions for  $s$  and  $t$  as functions of cartesian stresses  $\sigma_{11}$ ,  $\sigma_{33}$  and  $\sigma_{13}$  in stead of principal stresses:

$$s = \frac{\sigma_{11} + \sigma_{33}}{2} \quad (2.61)$$

$$t = \sqrt{\left(\frac{\sigma_{11} - \sigma_{33}}{2}\right)^2 + \sigma_{13}^2} \quad (2.62)$$

#### 2.5.4 Mean and Deviatoric Stress Formulations

To express the yield surface in terms of effective hydrostatic stress  $p$  and deviatoric stress  $q$ , a new parameter  $b$  is introduced, relating the intermediate principal stress  $\sigma_2$  to the minimum and maximum principal stresses. The parameter is defined by:

$$b = \frac{\sigma_2 - \sigma_3}{\sigma_1 - \sigma_3} \quad (2.63)$$

$$\implies \sigma_2 = \sigma_3 + b(\sigma_1 - \sigma_3) \quad (2.64)$$

The  $p$ - $q$ -formulation of the Mohr–Coulomb-criterion may be presented with the definition of  $q = \sigma_1 - \sigma_3$ . Here, the formulation of the criterion will be shown with the full formulation of  $q$  as defined in equation (2.19), to make use of its relation to the invariant  $J_2$  later:

$$\begin{aligned} q &= \sqrt{\frac{1}{2}[(\sigma_1 - \sigma_2)^2 + (\sigma_2 - \sigma_3)^2 + (\sigma_3 - \sigma_1)^2]} \\ &= \sqrt{\frac{1}{2}[(\sigma_1 - \sigma_3)^2(1 - b)^2 + (\sigma_1 - \sigma_3)^2b^2 + (\sigma_3 - \sigma_1)^2]} \\ &= (\sigma_1 - \sigma_3)\sqrt{1 - b + b^2} \end{aligned} \quad (2.65)$$

Principal stresses now relate to mean and deviatoric stresses by:

$$\sigma_1 = p + \frac{2 - b}{3\sqrt{1 - b + b^2}}q \quad (2.66)$$

$$\sigma_3 = p - \frac{1 + b}{3\sqrt{1 - b + b^2}}q \quad (2.67)$$

Inserted into equation (2.54) and collecting  $q$ -terms and  $(p+a)$ -terms gives:

$$q = \frac{3\sqrt{1-b+b^2}(N_f-1)}{(1+b)N_f+(2-b)}(p+a) = M(p+a) \quad (2.68)$$

Now the yield surface may be expressed as

$$F = q - M(p+a) = 0, \quad \text{where} \quad M = \frac{3\sqrt{1-b+b^2}(N_f-1)}{(1+b)N_f+(2-b)} \quad (2.69)$$

A more common expression for the inclination  $M$ , where  $q = \sigma_1 - \sigma_3$  is used in the derivation is (Nordal, 2012b):

$$M = \frac{3(N_f-1)}{3+(1+b)(N_f-1)} \quad (2.70)$$

For the special cases of triaxial compression ( $\sigma_2 = \sigma_3 \implies b = 0$ ) and triaxial extension ( $\sigma_1 = \sigma_2 \implies b = 1$ ) either of the expressions for the inclination  $M$  yields:

$$M_c = M(b=0) = \frac{6 \sin \phi}{3 - \sin \phi} \quad (2.71a)$$

$$M_e = M(b=1) = \frac{6 \sin \phi}{3 + \sin \phi} \quad (2.71b)$$

### 2.5.5 Dilatancy Control

As discussed in section 2.3.5, soils are not correctly modeled by an associated flow rule. This may be seen for a material at failure. At failure, no stress increment may be applied and any strains are plastic. The ratio between strains in the first and third principal direction for a Mohr–Coulomb model in drained conditions, with the yield surface defined in equation (2.54) and associated flow is:

$$\frac{d\varepsilon_3}{d\varepsilon_1} \approx \frac{d\varepsilon_3^p}{d\varepsilon_1^p} = \frac{d\lambda \frac{\partial F}{\partial \sigma_3}}{d\lambda \frac{\partial F}{\partial \sigma_1}} = -N_f \quad (2.72)$$

For a friction angle  $\phi = 30^\circ$ ,  $N_f = 3$  which implies that lateral strains will be 3 times as large as strains in axial direction.

This may also be seen from Figure 2.5, which sketches the failure criterion plotted in a  $\sigma_1$ - $\sigma_3$ -plane, along with a plastic potential function for the Mohr–Coulomb model for a given stress state  $\boldsymbol{\sigma}$ . The associated flow rule (plastic stress increment normal to  $Q = F$ ) gives a large plastic strain contribution in  $\sigma_3$ -direction. As a remedy the dilation angle  $\psi < \phi$  is introduced, accounting

for less volume change. The non-associated flow rule (plastic stress increment normal to  $Q \neq F$ ) gives a smaller plastic strain contribution in  $\sigma_3$ -direction than the associated flow rule. The plastic potential function  $Q$  for a Mohr–Coulomb constitutive model is:

$$Q = (\sigma_1 + a) - N_\psi(\sigma_3 + a) = 0, \quad \text{where} \quad N_\psi = \frac{1 + \sin \psi}{1 - \sin \psi} \quad (2.73)$$

Thus, plastic strains in  $\sigma_3$ -direction may be modeled more realistically with a non-associated flow rule.

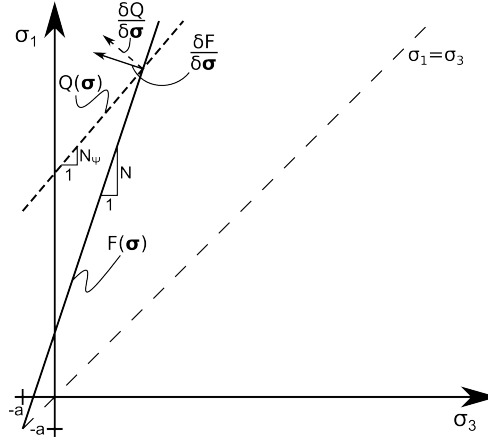


**Figure 2.5:** Sketch of a  $\sigma_1$ - $\sigma_3$ -plot showing associated flow rule and non-associated flow rule connected to a plastic potential function where the dilation angle controls the flow. (Nordal, 2012b, Figure 6.3), (Nordal, 2012b, Figure 6.4)

At large strains, i.e. at failure, the relation between volumetric and first principal strain for a drained triaxial test is:

$$\begin{aligned} \frac{d\varepsilon_V^p}{d\varepsilon_1^p} &= \frac{d\varepsilon_1^p + d\varepsilon_2^p + d\varepsilon_3^p}{d\varepsilon_1^p} = \frac{d\lambda \frac{\partial Q}{\partial \sigma_1} + d\lambda \frac{\partial Q}{\partial \sigma_2} + d\lambda \frac{\partial Q}{\partial \sigma_3}}{d\lambda \frac{\partial Q}{\partial \sigma_1}} \\ &= 1 + 0 - N_\psi = \frac{-2 \sin \psi}{1 - \sin \psi} \end{aligned} \quad (2.74)$$

This gives a useful expression for the inclination of a path in a  $\varepsilon_1$ - $\varepsilon_v$ -plot at large strains, giving the dilation angle from laboratory curves.

Typical dilation angle of quartz sand is given as (Nordal, 2012b), (PLAXIS, 2012a):

$$\psi = \begin{cases} \psi = \phi - 30^\circ & \text{if } \phi > 30^\circ \\ \psi = 0^\circ & \text{if } \phi \leq 30^\circ \end{cases} \quad (2.75)$$

### 2.5.6 Yield Surfaces in Haigh–Westergaard Coordinates

The yield surfaces of the Mohr–Coulomb-criterion may be expressed in Haigh–Westergaard coordinates. This eases plotting in the full stress space or in a  $\Pi$ -plane. The reader is referred to Appendix B.2 for derivation of the expressions, but a summary is given here.

The Mohr–Coulomb criterion in equation (2.53) may be written as:

$$\frac{\sigma_1 - \sigma_3}{2} = \frac{\sigma_1 + \sigma_3}{2} \sin \phi + a \sin \phi \quad (2.76)$$

$$\implies \sigma_1(1 - \sin \phi) - \sigma_3(1 + \sin \phi) = 2a \sin \phi \quad (2.77)$$

Expression for the principal stresses as functions of the Haigh–Westergaard coordinates from equation (2.22) may be inserted into the Mohr–Coulomb criterion. After gathering of terms, some trigonometric relations are used to simplify the expressions and the six yield surfaces may be written as:

$$\rho(\xi, \theta) = \frac{\sqrt{6}a \sin \phi + \sqrt{2}\xi \sin \phi}{\pm\sqrt{3} \sin(\theta + \frac{\pi}{3}) - \cos(\theta + \frac{\pi}{3}) \sin \phi} \quad (2.78a)$$

$$\rho(\xi, \theta) = \frac{\sqrt{6}a \sin \phi + \sqrt{2}\xi \sin \phi}{\pm\sqrt{3} \sin(\theta + \frac{2\pi}{3}) - \cos(\theta - \frac{\pi}{3}) \sin \phi} \quad (2.78b)$$

$$\rho(\xi, \theta) = \frac{\sqrt{6}a \sin \phi + \sqrt{2}\xi \sin \phi}{\pm\sqrt{3} \sin \theta + \cos \theta \sin \phi} \quad (2.78c)$$

## 2.6 The Drucker–Prager Criterion

The Drucker–Prager strength criterion is a pressure dependent criterion, giving effective stress dependency of the strength like the Mohr–Coulomb criterion. While the Mohr–Coulomb criterion is defined by six yield surfaces, the Drucker–Prager criterion is defined by one single surface.

### 2.6.1 Defining Equations

The criterion is a modification of the pressure independent von Mises-criterion. For a constant hydrostatic stress, as in a  $\Pi$ -plane-plot, the strength surface reduces to a circle. Drucker and Prager (1952) defined the strength surface defined by invariants and the coefficients  $\alpha$  and  $k$  and by classical geotechnical sign convention the criterion reads:

$$F = \sqrt{J_2} - \alpha I_1 = k \quad (2.79)$$

This may be rewritten in accordance to conventional way of defining a yield surface  $F = 0$ :

$$F = \sqrt{J_2} - \alpha I_1 - k = 0 \quad (2.80)$$

For the special case of  $\alpha = 0$ , the von Mises criterion is obtained. The criterion is sometimes referred to as the extended von Mises-criterion.

The property of one, single surface is attractive for implementation in computer codes. The yield surface has the form of a right circular cone with the axis directed along the hydrostatic axis in principal stress space, and the apex in the point  $(\sigma_1, \sigma_2, \sigma_3) = (-a, -a, -a)$ , shown in Figure 2.6.

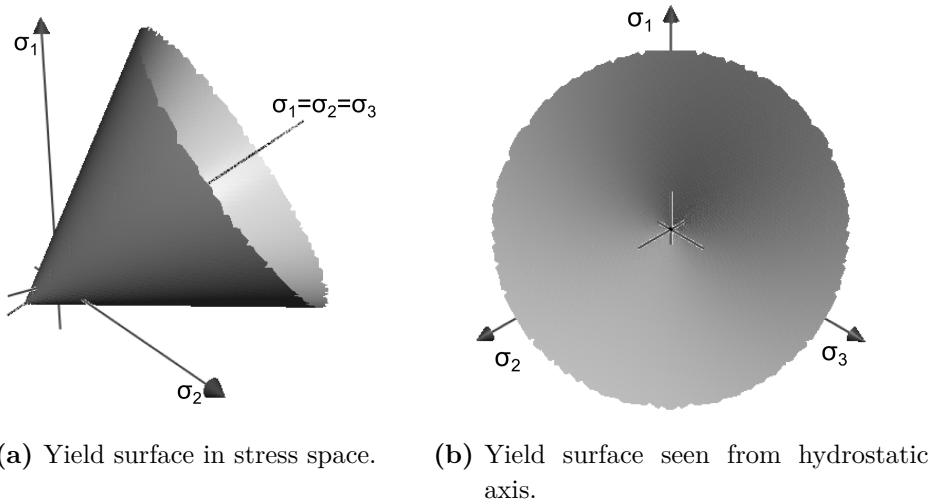


**Figure 2.6:** Drucker–Prager yield surface.

### 2.6.2 Coefficients of the Drucker-Prager Criterion

The coefficients  $\alpha$  and  $k$  are parameters that are not in use in common geotechnical practice. Proper calibration of the parameters may hence be difficult in practice. A possibility is to set the parameters such that the Drucker–Prager criterion match other criteria for certain conditions, such as the Mohr–Coulomb criterion in different stress states.

**Triaxial conditions** By relating mean effective stress  $p$  and deviatoric stress  $q$  to the invariants  $I_1$  and  $J_2$  using the relations from equations (2.12) and



(2.19), the Drucker–Prager-criterion may be written as:

$$\begin{aligned} F &= \frac{q}{\sqrt{3}} - 3\alpha p - k = 0 \\ \implies F &= q - 3\sqrt{3} \cdot \alpha p - \sqrt{3} \cdot k = 0 \end{aligned} \quad (2.81)$$

Matching the  $p$ - $q$ -formulation of the Mohr–Coulomb criterion in equation (2.69) with equation (2.81), gives relations for the coefficients  $\alpha$  and  $k$  to inclination  $M$  and attraction  $a$  by:

$$3\sqrt{3} \cdot \alpha = M \quad (2.82a)$$

$$\sqrt{3} \cdot k = M \cdot a \quad (2.82b)$$

The expressions for  $M$  in triaxial conditions are stated in equation (2.71), giving:

$$\alpha_{\text{TXC}} = \frac{M_c}{3\sqrt{3}} = \frac{2 \sin \phi}{\sqrt{3}(3 - \sin \phi)} \quad (2.83a)$$

$$\alpha_{\text{TXE}} = \frac{M_e}{3\sqrt{3}} = \frac{2 \sin \phi}{\sqrt{3}(3 + \sin \phi)} \quad (2.83b)$$

$$k = 3a \cdot \alpha \quad (2.83c)$$

**Plane strain** The Drucker–Prager criterion may be matched with the Mohr–Coulomb criterion in plane strain by manipulation of the invariants  $I_1$  and  $J_2$ , as first shown by Drucker and Prager (1952). The derivation is reproduced in the following.

At failure, stress change equals zero per definition in a linear elastic-perfect plastic model. Due to this, elastic strains cannot change at failure and all strain change is plastic. Assuming associated flow and imposing the conditions of no change in strain out of the plane, results in a condition for the Drucker–Prager criterion in plane strain:

$$\begin{aligned} d\varepsilon_{22} = d\varepsilon_{22}^p &= d\lambda \frac{\partial F}{\partial J_2} \frac{\partial J_2}{\partial \sigma_{22}} = d\lambda \left( \frac{s_{22}}{2\sqrt{J_2}} - \alpha \right) = 0 \\ \implies s_{22} &= 2\alpha\sqrt{J_2} \end{aligned} \quad (2.84)$$

Now the first full stress invariant may be expressed as:

$$\begin{aligned} I_1 &= \sigma_{11} + (s_{22} + \frac{1}{3}I_1) + \sigma_{33} \implies \frac{2}{3}I_1 = \sigma_{11} + \sigma_{33} + 2\alpha\sqrt{J_2} \\ I_1 &= \frac{3}{2}(\sigma_{11} + \sigma_{33}) + 3\alpha\sqrt{J_2} = 3s + 3\alpha\sqrt{J_2} \end{aligned} \quad (2.85)$$

where  $s$  is the center of Mohr’s circle from equation (2.57).

Through some mathematical operations, the second deviatoric invariant may be transformed:

$$\begin{aligned}
 J_2 &= \frac{1}{2}s_{11}^2 + \frac{1}{2}s_{22}^2 + \frac{1}{2}s_{33}^2 + \sigma_{13}^2 \\
 &= \frac{1}{2}(\sigma_{11} - \frac{1}{3}I_1)^2 + \frac{1}{2} \cdot 4\alpha^2 J_2 + \frac{1}{2}(\sigma_{33} - \frac{1}{3}I_1)^2 + \sigma_{13}^2 \\
 J_2(1 - 2\alpha^2) &= \frac{1}{2}(\frac{1}{2}\sigma_{11} - \frac{1}{2}\sigma_{33} - \alpha\sqrt{J_2})^2 + \frac{1}{2}(\frac{1}{2}\sigma_{33} - \frac{1}{2}\sigma_{11} - \alpha\sqrt{J_2})^2 + \sigma_{13}^2 \\
 &= \frac{1}{2}(\frac{1}{4}\sigma_{11}^2 + \frac{1}{4}\sigma_{33}^2 + \alpha^2 J_2 - \frac{1}{2}\sigma_{11}\sigma_{33} - \sigma_{11}\alpha\sqrt{J_2} + \sigma_{33}\alpha\sqrt{J_2}) \\
 &\quad + \frac{1}{2}(\frac{1}{4}\sigma_{11}^2 + \frac{1}{4}\sigma_{33}^2 + \alpha^2 J_2 - \frac{1}{2}\sigma_{11}\sigma_{33} + \sigma_{11}\alpha\sqrt{J_2} - \sigma_{33}\alpha\sqrt{J_2}) + \sigma_{13}^2 \\
 &= (\frac{1}{4}\sigma_{11}^2 - \frac{1}{2}\sigma_{11}\sigma_{33} + \frac{1}{4}\sigma_{33}^2) + \sigma_{13}^2 + \alpha^2 J_2 \\
 J_2 &= \frac{[\frac{1}{2}(\sigma_{11} - \sigma_{33})]^2 + \sigma_{13}^2}{1 - 3\alpha^2} = \frac{t^2}{1 - 3\alpha^2} \tag{2.86}
 \end{aligned}$$

where  $t$  is the radius of Mohr's circle from equation (2.58).

Inserting the expressions of the invariants in equations (2.85) and (2.86) into the Drucker–Prager strength criterion from equation (2.80), yields:

$$\begin{aligned}
 F &= \sqrt{J_2} - \alpha \left( 3s + 3\alpha\sqrt{J_2} \right) - k = 0 \\
 F &= t\sqrt{(1 - 3\alpha^2)} - 3\alpha s - k = 0 \\
 F &= t - \frac{3\alpha}{\sqrt{(1 - 3\alpha^2)}}s - \frac{k}{\sqrt{(1 - 3\alpha^2)}} = 0 \tag{2.87}
 \end{aligned}$$

Finally, it is possible to match the plane strain formulation of Mohr–Coulomb in equation (2.59) with equation (2.87) giving expressions for the coefficients  $\alpha$  and  $k$ :

$$\frac{3\alpha}{\sqrt{1 - 3\alpha^2}} = \sin \phi \tag{2.88a}$$

$$\frac{k}{\sqrt{1 - 3\alpha^2}} = a \cdot \sin \phi \tag{2.88b}$$

The expressions for  $\alpha$  and  $k$  in plane strain reads:

$$\alpha = \frac{\sin \phi}{\sqrt{3}\sqrt{3 + \sin^2 \phi}} \tag{2.89a}$$

$$k = 3a \cdot \alpha \tag{2.89b}$$

**Summary** The coefficients of the Drucker–Prager criterion are summarized in Table 2.1 for matching the Mohr–Coulomb-model in different stress states.

**Table 2.1:** Coefficients of the Drucker–Prager criterion matching the Mohr–Coulomb-model for different stress states.

Stress state	$\alpha$	$k$
Triaxial compression	$\frac{2 \sin \phi}{\sqrt{3}(3 - \sin \phi)}$	$3a \cdot \alpha = \frac{6a \cdot \sin \phi}{\sqrt{3}(3 - \sin \phi)}$
Triaxial extension	$\frac{2 \sin \phi}{\sqrt{3}(3 + \sin \phi)}$	$3a \cdot \alpha = \frac{6a \cdot \sin \phi}{\sqrt{3}(3 + \sin \phi)}$
Plane strain	$\frac{\sin \phi}{\sqrt{3}\sqrt{3 + \sin^2 \phi}}$	$3a \cdot \alpha = \frac{3a \cdot \sin \phi}{\sqrt{3}\sqrt{3 + \sin^2 \phi}}$

### 2.6.3 Yield Surface in Haigh–Westergaard Coordinates

The Drucker–Prager criterion may easily be stated in Haigh–Westergaard coordinates. Inserting the relations  $\rho = \sqrt{2J_2}$  and  $\xi = I_1/\sqrt{3}$  from chapter 2.2.4 gives:

$$\begin{aligned}
 F &= \sqrt{J_2} - \alpha I_1 - k = 0 \\
 \implies \frac{\rho}{\sqrt{2}} - \sqrt{3} \cdot \alpha \xi - k &= 0
 \end{aligned} \tag{2.90}$$

Thus, the Drucker–Prager yield surface in Haigh–Westergaard coordinates is:

$$\rho = \rho(\xi, \theta) = \sqrt{6}\alpha\xi + \sqrt{2}k \tag{2.91}$$

This is used to sketch the Drucker–Prager yield surface in the  $\Pi$ -plane in Figures 2.7 and 2.8 for the different expressions of the  $\alpha$ -coefficient. The Mohr–Coulomb yield surfaces are also sketched showing how different  $\alpha$ -coefficients correspond to different calibrations of the Drucker–Prager-model.

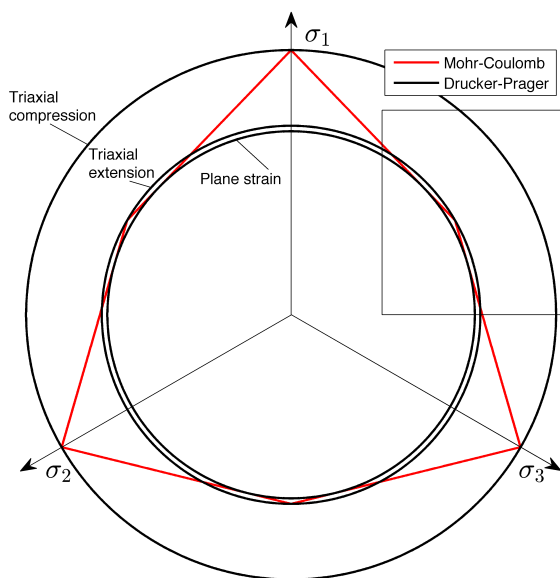


**Figure 2.7:** Yield surfaces of Drucker–Prager with the different  $\alpha$ -coefficients, along with the Mohr–Coulomb yield surfaces.

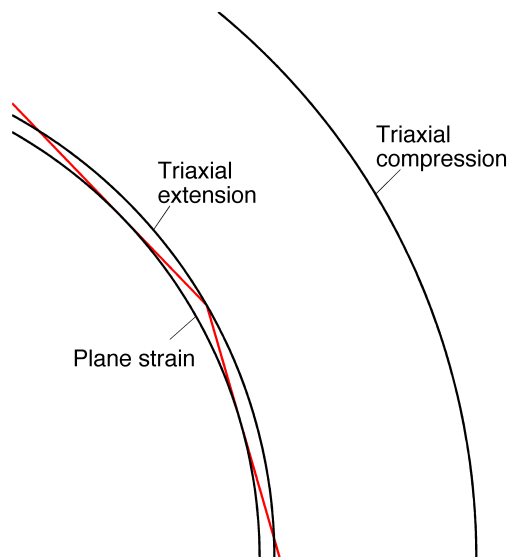


**Figure 2.8:** Detailed view of the yield surfaces.

### 2.6.4 Hardening Parameter

A possible hardening formulation for the Drucker–Prager criterion is to let  $\sin \rho$  be the hardening parameter, where  $\rho$  is the mobilized friction angle. As stated in section 2.3.6, strain hardening relates the hardening parameter directly to accumulated plastic strains. If it is assumed that there exists a unique relation between hardening parameter  $\sin \rho$  and accumulated plastic strains  $\lambda = \Sigma \Delta \lambda$ , results from laboratory tests may be used to express this relation. NTNU/NTH research supports this assumption (Nordal, 2012a). The hardening parameter may easily be related to the criterion through the  $\alpha$ -coefficients in Table 2.1, by relating the coefficient to mobilized friction  $\sin \rho$  rather than ultimate friction  $\sin \phi$ . Thus, the  $\alpha = \alpha(\sin \rho)$  increases from a low value, possibly zero, up to the failure value  $\alpha = \alpha(\sin \phi)$ .

It should be noted that even though the mobilized friction arises from the stress state, after calibration from laboratory tests, the mobilized friction is defined as a hardening parameter independent of the stress state. The development of the hardening parameter only relates to accumulated plastic strains, not to the actual stress state.

In order to establish a relation between  $\sin \rho$  and  $\lambda = \Sigma \Delta \lambda$ , triaxial tests may be used. Assuming associated flow rule gives:

$$\Delta \varepsilon_1^p = \Delta \lambda \frac{\partial F}{\partial \sigma_1} = \Delta \lambda \left( \frac{s_1}{2\sqrt{J_2}} - \alpha_F \right) \quad (2.92a)$$

$$\Delta \varepsilon_3^p = \Delta \lambda \frac{\partial F}{\partial \sigma_3} = \Delta \lambda \left( \frac{s_3}{2\sqrt{J_2}} - \alpha_F \right) \quad (2.92b)$$

For triaxial conditions, the second deviatoric invariant relates to the principal stresses through  $\sqrt{J_2} = \frac{1}{\sqrt{3}}q = \frac{1}{\sqrt{3}}(\sigma_1 - \sigma_3)$ . The difference between the principal plastic strains is then:

$$\Delta \varepsilon_1^p - \Delta \varepsilon_3^p = \Delta \lambda \frac{s_1 - s_3}{2\sqrt{J_2}} = \Delta \lambda \sqrt{3} \frac{\sigma_1 - \sigma_3}{2(\sigma_1 - \sigma_3)} = \frac{\sqrt{3}}{2} \Delta \lambda \quad (2.93)$$

By subtracting the elastic strains from the total strains, changes in the plastic parameter  $\Delta \lambda$  can be found for each increment of the triaxial test. Now, mobilized friction may be plotted versus accumulated plastic strains as seen in Figure 2.9, and a unique relation can be obtained. The relation may for instance be a quarter of an ellipse or a superellipse or a hyperbola asymptotically reaching the ultimate friction  $\sin \phi$ . As coefficients of the yield function now is dependent on the mobilized friction, which in turn is dependent on the

accumulated plastic strains, the yield function itself is dependent on more than only the stress state, giving  $F = F(\boldsymbol{\sigma}, \lambda)$ .

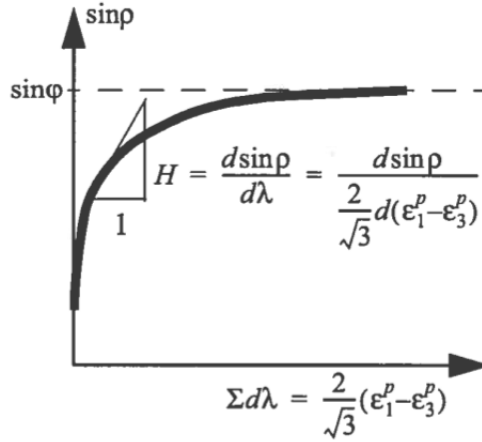


**Figure 2.9:** Sketch of accumulated plastic strains plotted against mobilized friction for a drained triaxial test. (Nordal, 2012a, Figure 6.21)

It may be seen from equation (2.93) that it also holds for non-associated flow if a properly chosen potential function  $Q$  is used.

### 2.6.5 Dilatancy and Dilatancy Control

To account for the dilatancy effects of soils, non-associated flow may be introduced by the plastic potential function  $Q$ . A simple adjustment of the yield function is:

$$Q = \sqrt{J_2} - \alpha_Q \cdot I_1 - C = 0 \quad (2.94)$$

where  $\alpha_Q$  may be taken as the  $\alpha$ -coefficients of Table 2.1 dependent on a dilation angle  $\psi$  instead of the friction angle  $\phi$ . The constant  $C$  is differentiated for any application of the plastic flow rule, but is used when potential functions are visualized at given stress states.

If  $\alpha_Q$  is controlled by the single input dilatancy parameter only, the representation of reality may be incorrect. This is in particular true if hardening is included from an initial isotropic state, causing plastic flow for the whole stress path. Some refinement of the dilatancy control is desirable. A possible formulation is to make an input dilatancy parameter  $\psi_0$  define a normalized  $\alpha_{Q0}$  by the previous stated expressions in Table 2.1. Further, the actual dilatancy may be formulated as a function of the normalized dilatancy and as many parameters as desired,  $\alpha_Q = \alpha_Q(\alpha_{Q0}, c_1, c_2, \dots)$ .

The plastic flow rule for non-associated flow and the chosen plastic potential function, results in:

$$\begin{aligned} d\varepsilon_V^p &= d\lambda \left( \frac{\partial Q}{\partial \sigma_1} + \frac{\partial Q}{\partial \sigma_2} + \frac{\partial Q}{\partial \sigma_3} \right) \\ &= d\lambda \left( \frac{s_1}{2\sqrt{J_2}} + \frac{s_2}{2\sqrt{J_2}} + \frac{s_3}{2\sqrt{J_2}} - 3\alpha_Q \right) = -3\alpha_Q d\lambda \end{aligned} \quad (2.95)$$

Using the expression for the plastic increment in equation (2.93), triaxial tests offers the possibility to plot  $\alpha_Q$  versus accumulated plastic strains for each increment. The  $\alpha_Q$ -variation for accumulated plastic strains may now be approximated by calibration of a function.

In addition to a plastic strain dependency, the dilation may be dependent on the effective mean stress level, as sketched in Figure 2.10. A reference mean stress  $p_{ref}$  may be defined for which a stress level below, i.e.  $p < p_{ref}$ , the soil dilates in an undrained triaxial test, while for stress levels greater, i.e.  $p > p_{ref}$ , the soil contracts. The reference stress may be a stand-alone user-defined input value, or connected to a "critical state" defined by for instance a critical void ratio.

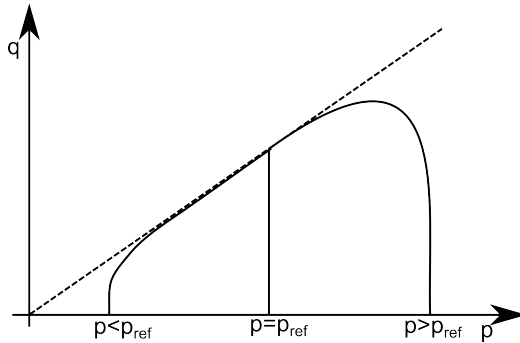


**Figure 2.10:** Sketch of a possible mean stress dependent dilation formulation.

When applying the conditions of no volumetric strains in undrained conditions, it may be observed that the mean stress change and  $\alpha_Q$  relates through:

$$d\varepsilon_V = d\varepsilon_V^e + d\varepsilon_V^p = \frac{dp}{K} - 3\alpha_Q d\lambda = 0 \quad (2.96)$$

For this condition to be fulfilled, a positive  $\alpha_Q$  needs to imply a positive mean stress change, hence dilative behavior. Negative  $\alpha_Q$  results in contractive behavior. It is seen that  $\alpha_Q$  and  $K$  governs the mean stress change.

## 2.7 State Parameter for Sands and Sand Modeling

The void ratio is a parameter that describes the current state of the soil. However, this is a reference point that depends on the mean stress level. A higher mean stress should give a more compact soil and lower void ratio. These are connected by a state parameter that may be used in constitutive modeling of sands.

### 2.7.1 A State Parameter for Sands

Been and Jefferies (1985) proposed a state parameter for sands that describes whether the density of sand at a given stress level gives loose or dense sand. For a given void ratio  $e$  at a high mean stress level, the sand will act as a loose sand. However, at small mean stress levels, the same sand acts as dense. The reference condition from which the state of the sand is defined by, rests on there being a "unique, repeatable particle arrangement at the steady state condition" (Been and Jefferies, 1985, p. 101).

The concept of the state parameter is defined by whether the sand is close to or far away from the steady state condition. By steady state, it is here referred to a critical or ultimate state that is obtained at large strains. A possible definition is "an ultimate condition in which plastic shearing could continue indefinitely without changes in volume or effective stresses" (Muir Wood, 1990, p. 139).

In  $e$ - $\log I_1$ -plane, two lines are defined. One line corresponds to the critical state and one parallel line to the current state, both with inclination  $\lambda^*$ . The vertical distance between the lines are the state parameter. This are illustrated in Figure 2.11. In other words is the state parameter the difference in void ratio between current and critical state for any constant mean stress level (Been and Jefferies, 1985):

$$\psi^* = e_\lambda - e_{ss} \quad (2.97)$$

To distinguish the state parameter and the inclination from dilation angle and plastic parameter, they are here denoted with asterisks in superscript. The void ratio for the current and the critical state are respectively:

$$e = e_\lambda - \lambda^* \log I_1 \quad (2.98a)$$

$$e_{cr} = e_{ss} - \lambda^* \log I_1 \quad (2.98b)$$

The state parameter is negative for dense sand, zero at the critical state and positive for loose sand.



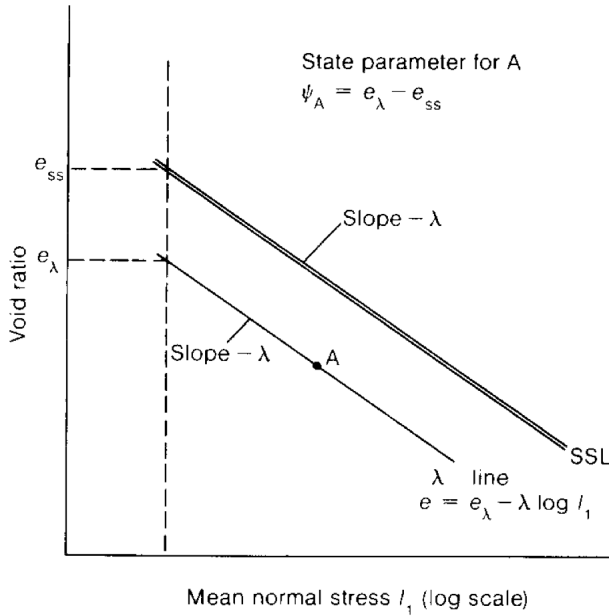


**Figure 2.11:** Illustration of the state parameter  $\psi^*$  (Been and Jefferies, 1985, Figure 2).

### 2.7.2 A Sand Model Applying the State Parameter

An application of the state parameter in a model for sand was presented by Muir Wood et al. (1994), later revised and extended by Gajo and Muir Wood (1999b) and Gajo and Muir Wood (1999a). The model is sometimes referred to as Severn Trent sand model and a short introduction is given here.

Triaxial compression conditions are assumed, hence  $\sigma_1 = \sigma_a$  and  $\sigma_2 = \sigma_3 = \sigma_r$  and a stress ratio  $\eta$  is defined:

$$\eta = \frac{q}{p} = \frac{\sigma_1 - \sigma_3}{\frac{1}{3}(\sigma_1 + 2\sigma_3)} \quad (2.99)$$

For cohesionless soil like sands, the  $p$ - $q$ -formulation of the Mohr–Coulomb criterion reduces equation (2.99) to the inclination  $M$  from equation (2.71):

$$\eta = \frac{q}{p} = M = \frac{6 \sin \phi}{3 - \sin \phi} \quad (2.100)$$

An available peak stress ratio  $M_p$  is assumed to be dependent on the state parameter  $\psi^*$ , the critical state stress ratio  $M_{cr}$  and a constant  $k$ :

$$M_p = M_{cr} - k\psi^* \quad (2.101)$$

Now, a hardening relation that connects stress ratio change to distortional strain  $\varepsilon_q$  is used, assuming the soil want to achieve the available stress ratio:

$$\frac{\eta}{M_p} = \frac{\varepsilon_q}{B + \varepsilon_q} \quad (2.102)$$

The parameter  $B$  governs the development of strains. Equation (2.102) fulfills the following properties:

$$\left. \frac{d\eta}{d\varepsilon_q} \right|_{\varepsilon_q=0} = \frac{M_p}{B} \quad (2.103a)$$

$$\lim_{\varepsilon_q \rightarrow \infty} \eta = M_p \quad (2.103b)$$

The sand will now always search the available stress ratio defined in equation (2.101) for the current state parameter value.

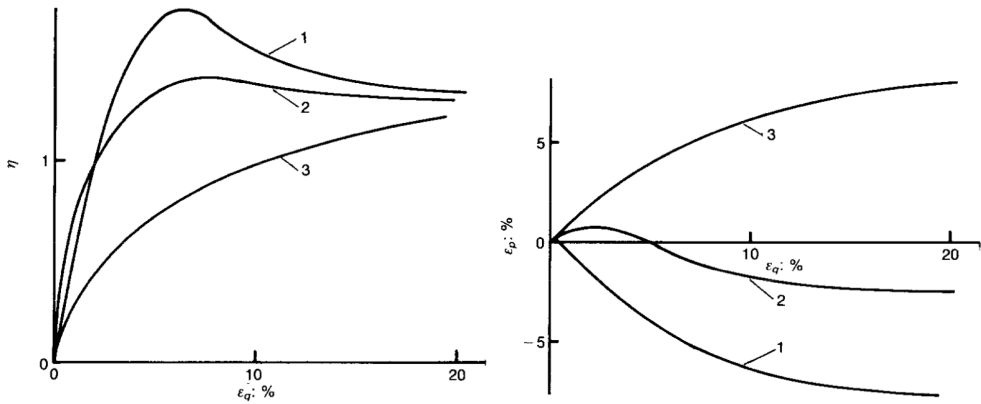
Finally, a flow rule is necessary to relate volumetric strains to distortional strains. Muir Wood et al. (1994) assumed a simple relation where:

$$\frac{d\varepsilon_p}{d\varepsilon_q} = A(M_{cr} - \eta) \quad (2.104)$$

For the special case of  $A = 1$ , the flow rule reduces to the flow rule of the original Cam Clay model (Muir Wood et al., 1994).

The initial value of the state parameter is of special importance. Initially deviatoric strains are zero, thus for a dense sand, the model will aim for a high peak stress, with post-peak softening when the state parameter evolves towards critical state. This may be seen by inserting a negative value for the state parameter in equation (2.101). The sand will now strive to reach a higher stress ratio than at critical state. On the contrary, for loose sand, the model asymptotically approach the critical state, continuously adjusting the aim towards the critical state. The Severn Trent model is now able to simulate the behavior of sand, sketched in Figure 2.12.

By simulations of Hokksund sand, Tadesse and Nordal (2002) showed that the model performs well, but an adjustment of the constants  $A$ ,  $B$  and  $k$  were proposed. In particular  $A$ , but also  $k$  and  $B$ , exhibited a variation over the relevant testing interval. A state parameter dependency were introduced and linear regression were performed to obtain a best fit linear line. This introduces a second degree dependency of the state parameter  $\psi^*$  to the available stress ratio in equation (2.101). With this modification, the model simulated the behavior of the sand well. Tadesse and Nordal (2002) pointed out that due to the state parameter dependency of  $A$ , attention should be paid to improve the flow rule of the model.



(a) Stress ratio-distortional strain curve. (b) Volumetric strain-distortional strain curve.

**Figure 2.12:** Figure showing typical drained triaxial compression tests on sand for (1) dense sand at low stress level, (2) dense sand at medium stress level and (3) loose sand at low stress level (Muir Wood et al., 1994, Figure 1).

## 2.8 Numerical Methods

The plastic strains are controlled by the plastic parameter  $d\lambda$ , which is a non-linear scalar that is not possible to integrate analytically in general. Thus, numerical methods are needed in the implementation of a constitutive model.

### 2.8.1 Stress Integration

A possible numerical method needed for implementation of constitutive modes, is the generalized trapezoidal rule. For a single-variable non-linear function  $y = f(x)$ , this is written as (Cook et al., 2002):

$$y_{n+1} = y_n + \left[ (1 - \gamma) \frac{dy}{dx} \Big|_n + \gamma \frac{dy}{dx} \Big|_{n+1} \right] \Delta x \quad (2.105)$$

where  $0 \leq \gamma \leq 1$  and  $y_{n+1}$  is the wanted output value for the next step after the known  $y_n$ -value.  $\gamma = 0$  and  $\gamma = 1$  correspond to the Euler forward and the Euler backward integration respectively, but  $\gamma$  may also take other values.

Explicit methods, such as the Euler forward integration, are in general less computational demanding than implicit methods, such as the Euler backward integration. Implicit methods use the calculated information at the end of the

step until a certain given tolerance is reached. An iterative corrector procedure enforces the step within the tolerance before the next step is calculated. Explicit methods use the information from the previous step to calculate all information in the next step. This causes the explicit method to drift away from the real solution. The greater steps the greater error. While each step in an implicit method is computational costly, it produces small errors even for large steps. Explicit methods are computationally cheaper, but demands smaller steps. The choice is hence a choice between few, expensive steps or many, cheap steps.

For a given strain increment a unique stress increment may be found, even for a linear elastic-perfect plastic material model at failure. This is not the case the other way. Thus, the non-linear equation that a computer code needs to solve in each sampling point is Hooke's law from equation (2.33), reproduced in equation (2.106)

$$\Delta\boldsymbol{\sigma} = \mathbf{D}\Delta\boldsymbol{\varepsilon}^e \quad (2.106)$$

Now, using a system formulation of the trapezoidal rule in equation (2.105) for a stress independent stiffness matrix, the stress in the next step may be written as:

$$\boldsymbol{\sigma}_{n+1} = \boldsymbol{\sigma}_n + \mathbf{D} \left[ (1 - \gamma)\Delta\boldsymbol{\varepsilon}_n^e + \gamma\Delta\boldsymbol{\varepsilon}_{n+1}^e \right] \quad (2.107)$$

Inserting strain decomposition and the flow rule from equations (2.31) and (2.39) gives

$$\begin{aligned} \boldsymbol{\sigma}_{n+1} &= \boldsymbol{\sigma}_n + \mathbf{D}\Delta\boldsymbol{\varepsilon} - \mathbf{D}\Delta\lambda \left[ (1 - \gamma) \left. \frac{\partial Q}{\partial \boldsymbol{\sigma}} \right|_n + \gamma \left. \frac{\partial Q}{\partial \boldsymbol{\sigma}} \right|_{n+1} \right] \\ &= \boldsymbol{\sigma}_{n+1}^{tr} - \mathbf{D}\Delta\lambda \left[ (1 - \gamma) \left. \frac{\partial Q}{\partial \boldsymbol{\sigma}} \right|_n + \gamma \left. \frac{\partial Q}{\partial \boldsymbol{\sigma}} \right|_{n+1} \right] \end{aligned} \quad (2.108)$$

where  $\boldsymbol{\sigma}_{n+1}^{tr}$  is an elastic trial stress that corresponds to the new stress if the step is purely elastic. The trial stress is constant for the whole step.

As the implicit method often performs well on today's computer for static problems, only this method will be further discussed.

## 2.8.2 Newton–Raphson Method

Newton–Raphson method is an iteration method for solving the non-linear equation,  $f(x) = 0$ , for single-variable function  $f$  with a continuous derivative

$f'$ . The method may be expressed as (Kreyszig, 2006):

$$x^{i+1} = x^i - \frac{f(x^i)}{f'(x^i)} \quad (2.109)$$

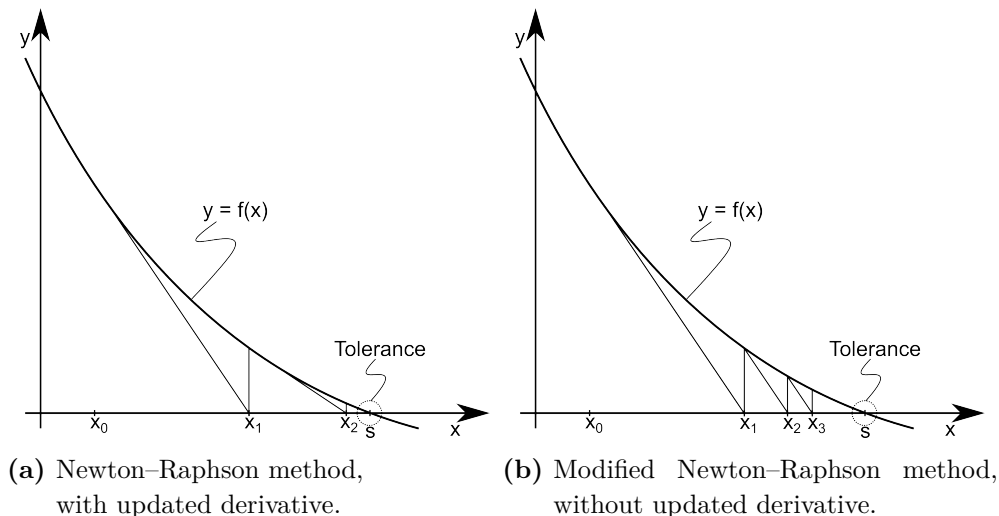


**Figure 2.13:** Two variants of the Newton–Raphson method for a non-linear function  $f(x) = 0$ .

Figure 2.13a shows the original Newton–Raphson method with updated derivatives for all iterations. To reduce computational demanding calculations, the modified Newton–Raphson method, shown in Figure 2.13b, does not update the derivatives, but as a consequence, more iterations are needed.

The iteration method requires a termination criterion or a defined tolerance. When the tolerance is reached, the last solution is accepted as a sufficiently good representation of the real solution. The method does not guarantee convergence, and another stop criterion of how many iterations that may be allowed should be included in any implementation. It may be shown that if certain conditions are fulfilled, the convergence is of second order, giving rapid convergence (Kreyszig, 2006). Thus, if a tolerance  $\text{tol} = 10^{-6}$  may be fulfilled, only one more iteration should be necessary to fulfill a tolerance  $\text{tol} = 10^{-12}$ . An important condition for convergence is that the starting value  $x^0$  is sufficiently close to the real solution  $s$  giving  $f(s) = 0$ .

Now, for a system of linear equations, equation (2.109) may be written as:

$$\mathbf{x}^{i+1} = \mathbf{x}^i - (\mathbf{J}^i)^{-1} \mathbf{f}(\mathbf{x}^i), \quad \text{where } \mathbf{J}^i = \left. \frac{\partial \mathbf{f}}{\partial \mathbf{x}} \right|_{\mathbf{x}=\mathbf{x}^i} \quad (2.110)$$

where  $\mathbf{J}$  is the Jacobian matrix.

In the elasto-plastic domain of the stress space, a plastic corrector, enforcing the stress back to the yield surface is necessary. The set of elasto-plastic equations in equation (2.108) gives the following condition for a finite step with the implicit method ( $\gamma = 1$ ):

$$\boldsymbol{\sigma}_{n+1} - \boldsymbol{\sigma}_{n+1}^{tr} + \Delta\lambda\mathbf{D}\frac{\partial Q}{\partial\boldsymbol{\sigma}} = \mathbf{0} \quad (2.111)$$

Further, the plastic yield function must remain  $F = 0$  during the entire yielding process. For the next step, the stress state contains six unknown cartesian stresses and an unknown plastic multiplier  $\lambda$ . Thus, there are seven equations gathered in a vector  $\mathbf{r}$  and seven unknowns gathered in a vector  $\mathbf{v}_{n+1}$ :

$$\mathbf{r} = \begin{bmatrix} \boldsymbol{\sigma}_{n+1} - \boldsymbol{\sigma}_{n+1}^{tr} + \Delta\lambda\mathbf{D}\frac{\partial Q}{\partial\boldsymbol{\sigma}} \\ F(\boldsymbol{\sigma}_{n+1}) \end{bmatrix} = \mathbf{0} \quad \mathbf{v}_{n+1} = \begin{bmatrix} \sigma_{11} \\ \sigma_{22} \\ \sigma_{33} \\ \sigma_{12} \\ \sigma_{23} \\ \sigma_{31} \\ \lambda \end{bmatrix}_{n+1} \quad (2.112)$$

Using the Newton–Raphson method for systems from equation (2.110) to solve the system of non-linear equations for the unknown in equation (2.112), the following iteration must be executed:

$$\mathbf{v}_{n+1}^{i+1} = \mathbf{v}_{n+1}^i - \left( \frac{\partial\mathbf{r}}{\partial\mathbf{v}_{n+1}} \Big|_i \right)^{-1} \mathbf{r}^i \quad (2.113)$$

Due to small steps and small changes in stresses for a strain increment, a proper starting value for the first iteration for the unknown  $\mathbf{v}_{n+1}$ , may be the known vector  $\mathbf{v}_n$ , such that  $\mathbf{v}_{n+1}^0 = \mathbf{v}_n$ . A possible termination criterion may be when the squared length of the vector  $\mathbf{r}$  is less than a given tolerance:

$$\mathbf{r}^T \mathbf{r} \leq \text{tol} \quad (2.114)$$

To avoid matrix inversion, equation (2.113) may be transformed to a linear system of equation on the form  $\mathbf{A}\mathbf{x} = \mathbf{b}$ . Introducing the incremental change in the vector  $\mathbf{v}_{n+1}$  for two consecutive iterations as  $\Delta\mathbf{v}_{n+1}^{i+1} = \mathbf{v}_{n+1}^{i+1} - \mathbf{v}_{n+1}^i$ , the

system to solve is:

$$\begin{aligned} \Delta \mathbf{v}_{n+1}^{i+1} &= - \left( \frac{\partial \mathbf{r}}{\partial \mathbf{v}_{n+1}} \Big| ^i \right)^{-1} \mathbf{r}^i \\ \left( \frac{\partial \mathbf{r}}{\partial \mathbf{v}_{n+1}} \Big| ^i \right) \Delta \mathbf{v}_{n+1}^{i+1} &= -\mathbf{r}^i \end{aligned} \quad (2.115)$$

Solving the system by Gauss elimination and adding the increment  $\Delta \mathbf{v}_{n+1}^{i+1}$  to the solution from the previous iteration, results in the next iteration. Thus, matrix inversion is avoided, reducing the necessary computation time.

The new stress state  $\boldsymbol{\sigma}_{n+1}$  corresponding to a new strain  $\boldsymbol{\varepsilon}_{n+1}$  is now found, ensuring the condition  $F(\boldsymbol{\sigma}_{n+1}) = 0$ .





## Chapter 3

# Implementation of an Elasto-Plastic Soil Model

The implementation of an elasto-plastic soil model is done by creating a routines in Fortran code, based on presented theory and with great help and effort by Rønningen (2014). In this chapter, the calculation process is first explained, before the implementation is summarized.

### 3.1 Calculation Process

In PLAXIS there is a possibility to implement user-defined soil models by in Fortran-code compiled to dll-files. These constitutive models simulate the soil behavior in a single material point, i.e. the resulting stress increment due to an applied strain increment. The global behavior is governed by the Finite Element Method implementation in PLAXIS.

#### 3.1.1 PLAXIS User-Defined Soil Models

For a given material point at a certain stress level, there are four necessary operations to make the calculation in PLAXIS run (PLAXIS, 2012a):

- Initialization of state variables.
- Calculation of stresses for the given strain increment
- Creation of elastic material stiffness matrix
- Creation of effective material stiffness matrix.

PLAXIS offers a set of parameters as input to the user-defined subroutine, which are previous stresses and state variables, strain and time increments. The routine is expected to return a set of output parameters, the current stresses and state variables.

The subroutine is governed by an input parameter to the subroutine, the `IDTask`-parameter. There are six `IDTasks` defined. For each, PLAXIS assigns different tasks that the global calculation needs at different stages in the calculation process. The two most important is `IDTask 1`, initializing the model and the state variables, and `IDTask 2`, calculating the stress increment for the given strain increment by a constitutive model (PLAXIS, 2012a).

### 3.1.2 The Stress Integration Algorithm

For stress integration at the sampling point, an elastic predictor-plastic corrector method is implemented.

According to Rønningen (2014) and Hopperstad and Børvik (2013), the elastic predictor-plastic corrector method first assumes that the given strain increment  $\Delta\boldsymbol{\varepsilon}_{n+1}$  for the current step, corresponds to pure elastic loading giving a trial state. If so, the plastic parameter will not change, such that the trial state is defined by:

$$\boldsymbol{\sigma}_{n+1}^{tr} = \boldsymbol{\sigma}_n + \mathbf{D}\Delta\boldsymbol{\varepsilon}_{n+1}, \quad \lambda_{n+1}^{tr} = \lambda_n \quad (3.1)$$

Now, if  $F(\boldsymbol{\sigma}_{n+1}^{tr}, \lambda_{n+1}) \leq 0$ , the strain increment is in fact elastic and the trial stress is the real stress for the increment:

$$\boldsymbol{\sigma}_{n+1} = \boldsymbol{\sigma}_{n+1}^{tr}, \quad \lambda_{n+1} = \lambda_{n+1}^{tr} \quad (3.2)$$

However, if  $F(\boldsymbol{\sigma}_{n+1}^{tr}, \lambda_{n+1}) > 0$ , the trial stress is an inadmissible stress state. Newton–Raphson method with Gauss-elimination for the linear system from equation (2.115), reproduced in equation (3.3), should be performed:

$$\left( \frac{\partial \mathbf{r}}{\partial \mathbf{v}_{n+1}} \Big| \right)^i \Delta \mathbf{v}_{n+1}^{i+1} = -\mathbf{r}^i \quad (3.3)$$

$$\mathbf{v}_{n+1}^{i+1} = \mathbf{v}_{n+1}^i + \Delta \mathbf{v}_{n+1}^{i+1} \quad (3.4)$$

until a tolerance criterion is fulfilled:

$$(\mathbf{r}^i)^T \mathbf{r}^i \leq \text{tol} \approx 10^{-12} \quad (3.5)$$

When the tolerance criterion is fulfilled, the very last iteration is taken as the final solution and the output may be extracted from  $\mathbf{v}_{n+1}^{i+1}$ :

$$\boldsymbol{\sigma}_{n+1} = \boldsymbol{\sigma}_{n+1}^{i+1}, \quad \lambda_{n+1} = \lambda_{n+1}^{i+1} \quad (3.6)$$

For pressure dependent yield criteria, another test must also be checked. The mean effective stress are not allowed to be less than the attraction  $a$  if tension is allowed, or less than zero if tension is not allowed. If violating this, the trial stress state should then be returned to the apex point. Thus, if  $p_{n+1}^{tr} < -a$ :

$$\boldsymbol{\sigma}_{n+1} = \sigma_{ij,n+1} = -a \cdot \delta_{ij}, \quad \lambda_{n+1} = \lambda_n \quad (3.7)$$

Thus, the algorithm for a given strain increment  $\Delta\boldsymbol{\varepsilon}_{n+1}$  may be summarized in the following steps (Rønningen, 2014):

1. Calculate trial stress  $\boldsymbol{\sigma}_{n+1}^{tr} = \boldsymbol{\sigma}_n + \mathbf{D}\Delta\boldsymbol{\varepsilon}_{n+1}$
2. If  $F \leq 0$ : Accept trial stress,  $\boldsymbol{\sigma}_{n+1} = \boldsymbol{\sigma}_{n+1}^{tr}$
3. If  $F > 0$ : Perform Newton–Raphson iterations until a tolerance criterion is fulfilled,  $\boldsymbol{\sigma}_{n+1} = \boldsymbol{\sigma}_{n+1}^{i+1}$ .
4. If  $p_{n+1}^{tr} < -a$ : Tension cut-off. Current stress is returned to apex point.

The principle of an algorithm with an elastic predictor-plastic corrector is illustrated in Figure 3.1 for a yield criterion with hardening.

### 3.1.3 Modular Programming

The elasto-plastic soil model is implemented by modular programming as developed by Rønningen (2014) and explained in this section. The structure of the subroutine is separated into three files, containing a number of subroutines, each with a certain designated task. This separation contains the most important advantage of modular programming. Two of the three subroutines are independent of the chosen material model. Thus, it is only one subroutine that needs to be modified if another material model should be considered. The same applies for the inclusion of new features into the code. As an example, a linear elastic-perfect plastic model may be implemented at first. Later, hardening may be introduced causing the need to change only the material model dependent subroutine.

Implementation of a model requires three files of computer code:

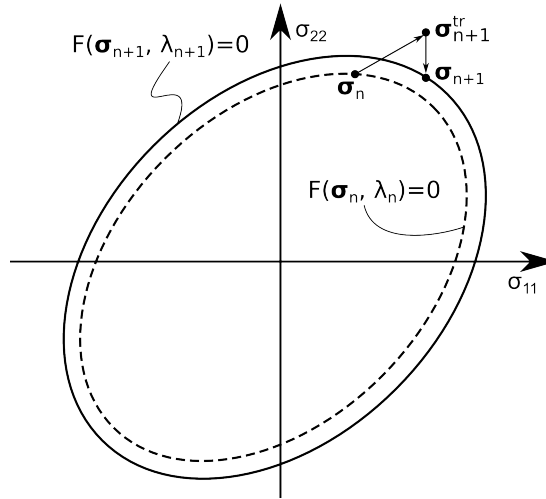


**Figure 3.1:** Elastic predictor-plastic corrector algorithm for a yield criterion with hardening, illustrated in a stress space. (Hopperstad and Børvik, 2013, Figure 7-18)

- Main subroutine, `User_Mod.f`: For each of the six `IDTasks`, the routine calls subroutines that are necessary to calculate the requested output to PLAXIS. The main subroutine is designed to be independent of the chosen constitutive model.
- Material model dependent helper subroutine, `drupra.f`: This contains all material specific operations and subroutines. For the implementation in this thesis it contains what is relevant and specific for a Drucker–Prager constitutive model. Examples of material specific modules is establishing the residual  $\mathbf{r}$  or calculating the Jacobian matrix  $\mathbf{J}$ .
- Material model independent helper subroutine, `helper.f`: This contains all helping routines that are material independent. The most important material independent routine is the Newton–Raphson iteration. When material specific operations are needed, the modules in the material model dependent subroutine are called upon.

The architecture is illustrated in Figure 3.2.

The possibility of analytic differentiation and creation of Fortran code in MATLAB also eases the work needed to add new features to or change the constitutive model. Thus, a large portion of the work in creating the material model dependent subroutine is basically done by altering a few lines of code

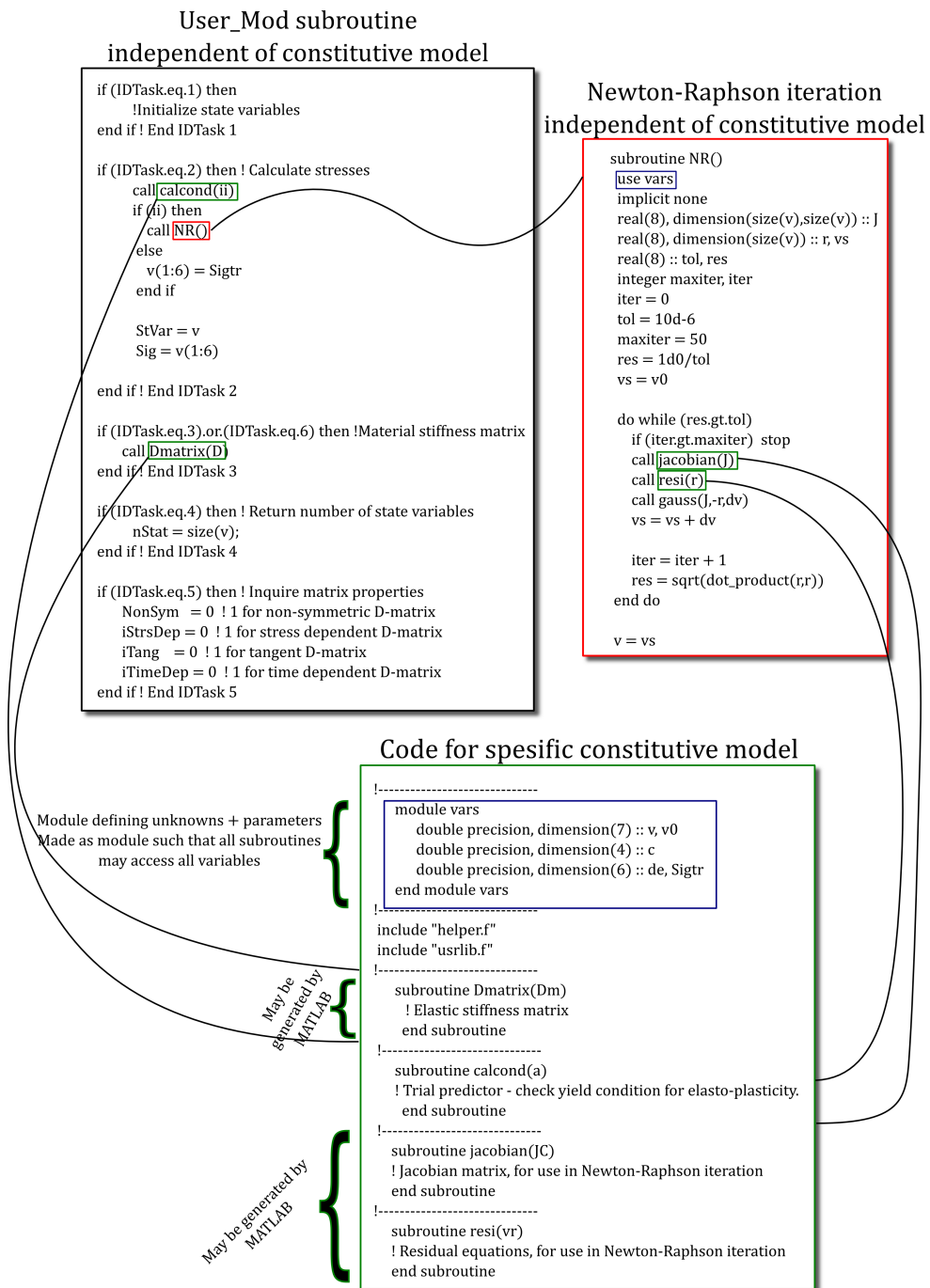


Figure 3.2: The calculation process of the implemented model (Rønningen, 2014).

in a MATLAB script. When the whole system is once built, it is a rather straightforward exercise to include a lot of features in the code (Rønningen, 2014).

Another advantage of this technique is that the main routine file is a more straightforward routine, making it easier for other to read and understand the code. The many smaller, yet necessary operations are put into two helper files, one material dependent and one material independent, and called upon when needed. Hence, it is easier to grasp the calculation process in the routine, without getting into all details at once. Each subroutine may be tested for debugging purposes. This makes it a less overwhelming task to debug the code.

A module, the vars-module, contains all global variables used in the code. Thus, all subroutines that activate this module gains access to the global variable. Any variable declared in the module are remembered and the need to send arrays between subroutines is greatly reduced, giving a cleaner code (Rønningen, 2014).

## 3.2 Material Independent Subroutines

As discussed above, modular programming opens up the possibility to gather everything material independent in separate subroutines. The architecture of the material independent subroutines will be discussed here.

### 3.2.1 Main Subroutine

The main subroutine of the implementation is given in Appendix C.1. The `IDTask` parameter is taken into the code as the first argument in the subroutine. As explained above, this is the argument governing what PLAXIS want as output, taking integer values between 1 and 6. In a calculation, each `IDTask` may be called several times in for each iteration, and the `IDTasks` are not ordered chronologically.

Several more arguments are taken into the main subroutine. The most important for this implementation are:

- `IsUndr`: Input parameter. For an undrained condition, `IsUndr = 1`, while `IsUndr = 0` for drained conditions.
- `Props`: Contains model parameters defined by the user is given as input to the calculation.

- **Sig0**, **Sig**: The previous stresses as an input vector and the requested current stresses as an output vector at current sampling point. Some additional information is given in the **Sig0**-vector.
- **Swp0**, **Swp**: Excess pore pressure given as input at previous step and requested as output for current step.
- **dEps**: Given strain increment for the current step.
- **StVar0**, **StVar**: Arrays containing the state variables at previous step and requested state variables for the current step.
- **iPl**: Plasticity indicator requested as output. **iPl** = 0 for elastic points, **iPl** = 1 for plastic points and **iPl** = 2 for tension cut-off points.

After the argument passing the vars-module is activated. Thus, values stored in parameters in the vars-module may be used by other routines activating the same module. As the arguments in the main subroutine are not accessible in other subroutines, this is useful in modular programming if the relevant arguments are copied to parameters in the vars-module.

In **IDTask 1** the state variables are to be initialized, but it is also possible to initialize the state variables in **IDTask 2**, as done in this implementation. The operations done in **IDTask 1** is calling zero vectors to avoid any troubles with undefined vectors in the calculation. Further, all properties is copied to an array declared in the vars-module.

**IDTask 2** contains the constitutive modeling. The stress state is used as state variables, thus the need to initialize the state variables in **IDTask 2**, as **Sig0** only contains zeroes in **IDTask 1**. **StVar0** is taken as start values for the array **v0**, and strains are copied to accessible arrays and parameters from the vars-module.

Now, the yield condition is calculated for a trial stress. **ipls** is a marker to point out apex point from the trial stress state. If the yield condition for the trial stress state is greater than zero, the trial stress state is in an inadmissible region and the Newton–Raphson routine is executed to obtain the new stress state. If the yield function for the trial stress is less than zero, the step is elastic and the trial stress is the new stress state. If the hydrostatic stress in the trial state is less than the attraction, the stress is sent back to the apex. For undrained conditions, excess pore pressure are calculated from the volumetric strain at the end of **IDTask 2**, giving the pore pressure change:

$$\Delta p_w = K_w \Delta \varepsilon_V \quad (3.8)$$

where  $K_w$  is the bulk modulus for water.

IDTask 3 and IDTask 6 return the effective and the elastic material stiffness matrices respectively, IDTask 4 return the number of state variables and IDTask 5 return some properties of the material stiffness matrix. At the end of the code, all necessary files must be included.

### 3.2.2 Helper Subroutine

In addition to the main subroutine, a helper subroutine is also material independent, given in Appendix C.2. After activation of the vars-module, a set of parameters necessary for the Newton–Raphson iteration are set. The most important are the `tol` parameter, defining the tolerance of the termination criterion from equation (3.5), and that the starting value for the iteration is set. For the implementation the tolerance for the length of the vector is set to  $10^{-6}$ .

The Newton–Raphson iteration implemented first calculates the Jacobian matrix and the residual for the first iteration. Next, Gauss elimination is performed for the system in equation (3.3), giving the incremental change in the unknown vector, which is added to the values of the previous iteration. At last the length of the residual vector is calculated and compared to the tolerance. If equation (3.5) is not fulfilled, the iteration continues.

Due to some difficulties, the Newton–Raphson scheme failed for some calculations. Reasons for the failure will be discussed in section 6.5, but an improvement that proved to work was to include a recursion loop if the tolerance was not fulfilled for a given number of iterations. The recursion loop first splits the strain increment into even smaller increments. Then the Newton–Raphson iteration runs until the tolerance is fulfilled in each substep. If not fulfilled, the strain increment is split once again.

In addition to the termination criterion of the residual, some other termination criteria are necessary. First, if also the recursion loop fail to fulfill the tolerance, a maximum number of iterations are set. Thus, the splitting of strain increment are not allowed to continue infinitely. In addition, a stop criterion is included in the recursion loop, ensuring that the loop is never entered more than one time downstream. In other words, the recursion may only be performed within the first calling upon itself.

At last the result for the unknown vector is sent back as output to the calling statement upstream.

The Gauss elimination routine used in the Newton–Raphson iteration, is



developed by Godunov (2009) solely. The routine solves the system of linear equations in equation (3.3) with scaling and pivoting. Due to lack of time, the routine was downloaded instead of developing it self as a part of the thesis.

### 3.2.3 User Interface Subroutine

Even though the user interface subroutine is not independent of the material, it is briefly described here, as quite little changes between the formulations. The subroutine contains all necessary information for the user interface in PLAXIS to work. This includes the number and name of models in the dll-file, parameter count, names, units and placement. In PLAXIS the user enters the parameters, and these are given to subroutine in the `Props` array. The structure of the interface subroutine is given by PLAXIS (2012a).

## 3.3 Development of Material Dependent Subroutine

The development process of the material dependent subroutine is briefly summarized. Details of the implementation will be presented in subsequent sections. Implementation, testing and evaluation of the model was carried out continuously throughout the semester. In this thesis, these processes is presented separately. The reader may either follow the structure of the thesis or jump between the chapters to follow the iterative development of the model.

### 3.3.1 Linear Elastic-Perfect Plastic Model

At first, the model was implemented as a linear elastic-perfect plastic model, first with associated flow, then with non-associated flow. Details of its implementation is presented in section 3.4. Procedures for testing the model are presented in section 4.1 and the results from the tests are presented in section 5.1. Evaluation and discussion of the results are presented in section 6.2.

### 3.3.2 Strain Hardening and Stress Dependent Dilatancy

Strain hardening and two simple mean stress dependent dilatancy formulations were included next. This was easily done using the advantage of modular programming. Necessary adjustments of the MATLAB script was performed. Details of the implementation is presented in section 3.5. Procedures for testing the model are presented in section 4.2 and the results from the tests are

presented in section 5.2. Evaluation and discussion of the results are presented in section 6.3.

### 3.3.3 Void Ratio Dependent Dilatancy

At last void ratio dependent dilatancy was included. One version with mean stress dependent elastic stiffnesses was also implemented. This only caused the need to add a few lines in the Fortran code. Details of the implementation is presented in section 3.6. Procedures for testing the model are presented in section 4.3 and the results from the tests are presented in section 5.3. Evaluation and discussion of the results are presented in section 6.4

## 3.4 Linear Elastic-Perfect Plastic Model

A linear elastic-perfect plastic model was implemented first. Such models reduce the possibility of errors due to its simplicity. The implementation of the model to be described in section 3.6.2 is shown in Appendix D.1, yet the structure of the subroutines has not changed radically. Even the code used for the linear elastic-perfect plastic model is hence quite similar to the latest version. Two of the subroutines used were established by analytical differentiation in MATLAB. The MATLAB script used for the latest version is given in Appendix D.2. Every version of the material dependent code and the MATLAB script are handed over to the department.

### 3.4.1 Associated Flow

Isotropic, linear elasticity and associated flow were chosen to be implemented at first, keeping the model as simple as possible. This causes the need for only four material parameters, two parameters governing the stiffness and two parameters governing the strength. The material dependent code needs to solve five tasks in the way the main subroutine and the Newton–Raphson iteration are implemented. These five tasks are:

- Establish the 6x6 elastic material stiffness matrix for an isotropic, linear elastic material.
- Check the yield condition for the trial stress state (elastic predictor).
- For the plastic corrector, Newton–Raphson iteration requires the Jacobian matrix.

- For the same reason, the residual vector must be calculated.
- For the residual vector, differentials of the yield condition with respect to stresses are needed.

Elastic material stiffness matrix are calculated in the `Dmatrix`-subroutine. All material parameters are first defined, accounting for a possible  $c$ - $\phi$ -reduction calculation to perform Safety calculations in PLAXIS. The attraction  $a$  is not reduced in the  $c$ - $\phi$ -reduction while the friction angle is reduced in accordance with the method done for the Mohr–Coulomb model in PLAXIS (2012b):

$$\tan \phi_{reduced} = \frac{\tan \phi_{input}}{\Sigma Msf} \quad (3.9)$$

The dilation angle  $\psi$  need to be checked so that it is not greater than the friction angle. This is relevant for safety calculations, such that unphysical behavior is avoided.

The coefficient  $\alpha$  in the Drucker–Prager yield criterion of equation (2.80) may be chosen as one of the expressions in Table 2.1. Further, the elastic stiffness matrix is calculated from Hooke’s law, as written in equation (2.35). The PLAXIS notation of stress and strain vectors are introduced, such that:

$$\begin{aligned} \boldsymbol{\sigma} &= \left( \sigma_{xx} \quad \sigma_{yy} \quad \sigma_{zz} \quad \sigma_{xy} \quad \sigma_{yz} \quad \sigma_{zx} \right)^T \\ \boldsymbol{\varepsilon} &= \left( \varepsilon_{xx} \quad \varepsilon_{yy} \quad \varepsilon_{zz} \quad \gamma_{xy} \quad \gamma_{yz} \quad \gamma_{zx} \right)^T \\ &= \left( \varepsilon_{xx} \quad \varepsilon_{yy} \quad \varepsilon_{zz} \quad 2\varepsilon_{xy} \quad 2\varepsilon_{yz} \quad 2\varepsilon_{zx} \right)^T \end{aligned} \quad (3.10)$$

Thus, the **D**-matrix is:

$$\mathbf{D} = \begin{bmatrix} K + \frac{4}{3}G & K - \frac{2}{3}G & K - \frac{2}{3}G & 0 & 0 & 0 \\ K - \frac{2}{3}G & K + \frac{4}{3}G & K - \frac{2}{3}G & 0 & 0 & 0 \\ K - \frac{2}{3}G & K - \frac{2}{3}G & K + \frac{4}{3}G & 0 & 0 & 0 \\ 0 & 0 & 0 & G & 0 & 0 \\ 0 & 0 & 0 & 0 & G & 0 \\ 0 & 0 & 0 & 0 & 0 & G \end{bmatrix} \quad (3.11)$$

With  $G$  and  $\nu$  as input parameters,  $K$  is calculated internally in the subroutine from equation (2.36) as:

$$K = \frac{K}{G}G = \frac{3(1 - 2\nu)}{2(1 + \nu)}G \quad (3.12)$$

The `Dmatrix`-subroutine gives a 6x6 array as output.

To check the yield criterion, the stress of the trial state is first calculated within the `calcond`-subroutine. Next, stress invariants of the trial state is calculated and then the yield condition for the Drucker–Prager criterion from equation (2.80) is checked, where the relation  $I_1 = 3p$  is used. The scalar value of the yield function is given as output. In addition, the starting values for the Newton–Raphson have been calculated in this subroutine. This is due to some challenges with convergence in the Newton–Raphson routine. The starting have been calculated by the use of a proposed solution by Cook et al. (2002), where a  $\beta$  value were defined as:

$$\beta \approx \frac{F_n}{F_n - F_{\text{trial}}} \quad (3.13)$$

where  $F_n$  and  $F_{\text{trial}}$  is the yield functions at the previous step and the trial state respectively. The starting values  $\boldsymbol{\sigma}_0$  for the stress are now set to:

$$\boldsymbol{\sigma}_0 = \boldsymbol{\sigma}_n + \beta \mathbf{D} \Delta \boldsymbol{\varepsilon} \quad (3.14)$$

This should bring the starting values closer to the yield surface and the final solution. The impact of this adjustment of starting values are greatest when strain increments that are almost pure elastic is imposed to low stress states.

The Jacobian matrix is calculated in the `jacobian`-subroutine. By use of the `fortran`-function in MATLAB, optimized Fortran codes are created in Fortran-files. Thus, efficient codes are easily established by the MATLAB script. The `jacobian`-subroutine gives a 7x7 array as output.

Residuals are gathered in the `r`-vector and calculated in the `resi`-subroutine. This subroutine subtracts trial stresses from the stresses for the current iteration, and then adds the product of the material stiffness and the plastic strain vector for the current iteration, as stated in (2.112). The 7x1 array giving the residual vector is the output of the subroutine. The subroutine could easily have been established from the MATLAB script, but were programmed manually here.

The `differentials`-subroutine calculates the vector giving  $\frac{\partial Q}{\partial \boldsymbol{\sigma}} = \frac{\partial F}{\partial \boldsymbol{\sigma}}$  for associated flow. As the `jacobian`-subroutine this subroutine was created by the MATLAB script. The output is a 6x1 array giving the differentials of the yield function with respect to the stresses, at the given stress state.

### 3.4.2 Non-Associated Flow

Non-associated flow implies that there is defined a plastic potential function that governs the plastic strain increments. The plastic potential function  $Q$

from equation (2.94) is applied, where the coefficient  $\alpha_Q$  is taken as a constant value. Expressions for  $\alpha_Q$  are shown in Table 2.1, but are functions of the dilation angle  $\psi$  rather than the friction angle  $\phi$ . By introducing this angle, the model now requires in total five input parameters, the same parameters as for the standard Mohr–Coulomb model in PLAXIS.

The introduction of a non-associated flow rule implies the need to change the `resi`-subroutine, the `jacobian`-subroutine and the `differentials`-subroutine, as the residual  $\mathbf{r}$  now is dependent on the plastic potential function. Creation of the subroutines is easily done in the MATLAB-script, introducing the potential function as explained.

## 3.5 Strain Hardening and Stress Dependent Dilatancy

To account for a more realistic soil behavior, strain hardening are introduced. Further, dilatancy are made dependent on the current mean stress.

### 3.5.1 Strain Hardening and Stress Dependent Dilation Angle

Taking  $\sin \rho$  as the hardening parameter of the Drucker–Prager model, isotropic friction controlled hardening is related to the yield criterion by making the  $\alpha$ -coefficient of the yield criterion dependent of the mobilized friction. The relation between the accumulated plastic parameter  $\lambda$  and the mobilized friction is defined as a hyperbola:

$$\sin \rho = \frac{H_0 \lambda}{1 + \frac{H_0 \lambda}{\sin \phi}} \quad (3.15)$$

Equation (3.15) fulfills the following properties:

$$\lim_{\lambda \rightarrow \infty} \sin \rho = \sin \phi \quad (3.16a)$$

$$\left. \frac{d \sin \rho}{d \lambda} \right|_{\lambda=0} = H_0 \quad (3.16b)$$

To make the dilation of the soil dependent on the mean stress, a reference mean stress  $p_{ref}$  is defined. As discussed in section 2.6.5, for mean stress levels greater than the reference stress, the soil should contract for undrained situations, and vice versa for stress levels smaller. To fulfill this, a linear

relation between the mean stress and the current dilation angle is defined directly:

$$\sin \psi = \sin \psi_0 \left( 1 - \frac{p}{p_{ref}} \right) \quad (3.17)$$

where  $\psi_0$  and  $p_{ref}$  are user-defined input values. The current dilation angle  $\psi$  gives the coefficient  $\alpha_Q$  in the plastic potential function. This is expected to give vertical effective stress paths at the mean stress level  $p = p_{ref}$ .

Implementing this in the subroutine is done by adapting the new equations in the MATLAB-script and introducing the  $\alpha = \alpha(\lambda)$ -dependency of the yield function and the mean stress dependency of the current dilation angle. Two new parameters need to be defined by the user. The initial "plastic stiffness"  $H_0$ , which may be found from triaxial tests as described in section 2.6.5, and the reference stress  $p_{ref}$ .

One possible interpretation of the mean stress level may be the critical state mean stress level. Several possibilities of such a mean stress level exist. The mean stress that are defined by the critical state line by Been and Jefferies (1985) state parameter described in section 2.7.1 is one interpretation. Another is half the preconsolidation  $p_c$ -stress from the Modified Cam Clay-model. At this mean stress level the Modified Cam Clay-model will neither contract nor dilate for an undrained triaxial test. The reference stress is however not connected to volumetric strains in any way.

### 3.5.2 Strain Hardening and Stress Dependent Dilation Coefficient

For reasons to be discussed in chapter 6.3.1, the dilation angle from equation 3.17 yields contractive and dilative response for undrained situations, above and below a mean stress level  $\approx 0.5p_{ref}$ , respectively, not above and below the intended reference stress  $p_{ref}$ .

Now, the intent of the dilation formulation is to ensure that at the reference stress level, there is no contractive or dilative response for undrained situations, i.e. there is no change in the mean effective stress level and  $dp = 0$ . Some kind of critical state is reached at  $p = p_{ref}$  at large strains. For undrained conditions the volumetric strain is zero, thus:

$$d\varepsilon_V = d\varepsilon_V^e + d\varepsilon_V^p = \frac{dp}{K} + d\lambda \frac{\partial Q}{\partial p} \Big|_{p=p_{ref}} = d\lambda \frac{\partial Q}{\partial p} \Big|_{p=p_{ref}} = 0 \quad (3.18)$$

As the infinitesimal change of the plastic multiplier is greater than zero for

plastic loading, the following must be satisfied:

$$\left. \frac{\partial Q}{\partial p} \right|_{p=p_{ref}} = 0 \quad (3.19)$$

The dilation angle  $\psi$  influence the  $\alpha_Q$ -coefficient in both the nominator and the denominator. Thus, it is an easier task to implement the mean stress dependency of the dilation if the dependency is assumed to be connected to the value of  $\alpha_Q$  itself, rather than through the dilation angle:

$$\alpha_Q = \alpha_{Q0} \left( 1 - \frac{p}{C_p \cdot p_{ref}} \right) \quad (3.20)$$

Here,  $\alpha_{Q0}$  is the calculated value of the coefficient where the user-defined input value  $\psi_0$  is used and  $C_p$  is yet to be determined. Due to the dilation angle influencing the  $\alpha_Q$ -coefficient in both nominator and denominator, this may represent more predictive approach. A mean stress change now affects the change in dilative behavior in the same manner for all stress states, independent of which  $\alpha_Q$ -coefficient used. Further,  $\alpha_Q$  reduces linearly towards the reference stress, not in the non-linear fashion as in previous section. The value of the  $\alpha_{Q0}$  is calculated in the `alfcalc`-subroutine.

Demanding the equation (3.19) to be proportional to  $\alpha_Q$  as in equation (2.95), equation (3.20) may be integrated to find the potential function:

$$\begin{aligned} Q &= \int dQ = f_1(q) \pm \alpha_{Q0} \cdot p \left( 1 - \frac{p}{2 \cdot p_{ref}} \right) \pm C_Q \\ &= f_1(q) - \frac{1}{3} \alpha_{Q0} \cdot I_1 \left( 1 - \frac{p}{2 \cdot p_{ref}} \right) - C_Q \end{aligned} \quad (3.21)$$

The factor of  $\frac{1}{3}$  will govern how fast dilation makes the effective stress path strive to reach the reference mean stress. It may be omitted to make the dilation evolve faster.

By matching this to the plastic potential function in equation (2.94), the coefficient  $C_p = 2$ , and  $\alpha_Q$  needs to be:

$$\alpha_Q = \alpha_{Q0} \left( 1 - \frac{p}{2p_{ref}} \right) \quad (3.22)$$

Now, equation (3.19) is fulfilled. This relation is included in the MATLAB script for updated material dependent subroutines.

The parameters that needs to be defined by the user for an application of the model are still the five parameters of the Mohr–Coulomb model, and in addition the initial plastic "stiffness"  $H_0$  and the reference mean stress  $p_{ref}$ .

### 3.6 Void Ratio Dependent Dilatancy

The reference stress  $p_{ref}$  may be an unfamiliar parameter for the user. Using Been and Jefferies (1985) state parameter, relations connecting the reference stress to the void ratio  $e$  gives the user more familiar parameters to provide, and also accounts for a reference stress that may change with the state of the soil. The elastic stiffness of the soil may also be implemented as mean stress dependent.

#### 3.6.1 Void Ratio Dependency with Constant Elastic Stiffness

The critical state line defined in Figure 2.11 gives state where the structure of the sand is independent of its initial conditions and any shear loading results in no mean stress change,  $dp = 0$ . Using this, a relation between critical state mean stress,  $p_{cr}$ , and a critical void ratio,  $e_{cr}$ , may be written as:

$$e_{cr} - e_{ss} = -\lambda^* \log p_{cr} \quad (3.23)$$

Here  $e_{ss}$  is the critical void ratio at a mean stress level  $p = 1\text{kPa}$  and  $\lambda^*$  is the inclination of the critical state line in a  $e$ - $\log p$ -plot. The Modified Cam Clay model also connects the changes in the void ratio through a logarithmic relation in a similar way.

In the Modified Cam Clay model, a variant of the logarithmic relation is used to calculate the volumetric compression of virgin loading. Now, if used opposite, for undrained situations the critical void ratio need to stay at the initial void ratio since there is no volume change. The critical stress may then be calculated as function of the void ratio parameters. If it is assumed that the reference mean stress is the critical stress of equation (3.23), it is:

$$p_{ref} = 10^{-\frac{e_0 - e_{ss}}{\lambda^*}} \quad (3.24)$$

The user now need to define more parameters than earlier, but they may be more familiar and connects the reference mean stress to the state of the soil.  $e_{ss}$  and  $\lambda^*$  may be obtained from a  $e$ - $\log p$ -plot, and in addition the initial void ratio  $e_0$  of the soil must be given as input. In total, the model now require nine material parameters, the five parameters of the Mohr–Coulomb model, initial plastic stiffness  $H_0$  and the three new parameters of equation (3.24) that defines the reference mean stress. Reference mean stress is calculated in the `Dmatrix`-subroutine by adding a line in the routine, not causing the need for any changes in the MATLAB script.



### 3.6.2 Mean Stress Dependency of Elastic Stiffness

Soil exhibits a mean stress dependent stiffness as discussed in section 2.3.3, even though this dependency introduces thermodynamic challenges. When applied to monotonic increasing load, as in triaxial tests, these challenges are of small concern, as opposed to cyclic loading or unloading/reloading loops. The dependency may be quite significant if the loading range is wide.

This dependency is implemented by relating a reference stiffness  $G^*$  at a reference stress  $p^*$  to the current stiffness  $G$  at current stress  $p$  by:

$$G = G^* \left( \frac{p}{p^*} \right)^m \quad (3.25)$$

As the Poisson's ratio is constant, the bulk modulus change follow the shear modulus change, seen from (3.12). It is more correct to regard it opposite, that the shear stiffness change follow the bulk stiffness change. However, the model were implemented with shear stiffness as one of the input parameter. This is the reason for the mean stress dependency is connected to the shear stiffness. The exponent  $m$  were set to 0.5 as the implementation were intended for sand simulations.

The stress dependency will actually cause the trial stress  $\sigma_{n+1}$  to change within the Newton–Raphson iteration. To avoid that this were a part of the iteration, the previous known mean stress is used as the mean stress level in the implementation. Thus the trial stress are still constant throughout the strain increment. It is assumed that this approximation does not introduce any big errors as the calculation steps are small. The calculation of the stiffness is done in the `Dmatrix`-subroutine. By this assumption the implementation of this does not cause need for any changes in the MATLAB script.



# Chapter 4

## Testing the Model

The procedures and settings used for testing the model are described in this chapter. All settings necessary to verify the results are given.

### 4.1 Linear Elastic-Perfect Plastic Model

To check the simplest version of the model, a number of simulations were run in PLAXIS to verify the model's behavior.

#### 4.1.1 Associated Flow in Single Material Point

The linear elastic-perfect plastic model with associated flow was tested for a single material point in the *SoilTest*-application in PLAXIS. Triaxial compression and extension tests were simulated with the *Triaxial*-module and driven to a strain level  $|\varepsilon_1| = 10\%$ . Plane strain test simulations were carried out in the *General*-module, applying plane strain conditions  $\Delta\sigma_{xx} = 0\text{kPa}$ ,  $\Delta\varepsilon_{yy} = -10\%$ ,  $\Delta\varepsilon_{zz} = 0\%$ ,  $\Delta\gamma_{xy} = 0\%$ . All tests were simulated as drained.

Four different combinations of material parameters and initial stresses were tested and are summarized in Table 4.1. For comparison, all test simulations were also executed by the Mohr–Coulomb model in PLAXIS. The Drucker–Prager model used the  $\alpha$ -coefficient from Table 2.1, coinciding with the Mohr–Coulomb model for the relevant stress states of the simulated tests, i.e.  $\alpha = \alpha_{\text{TXC}}$  for triaxial compression and so on.

**Table 4.1:** Parameter sets for validation of linear elastic-perfect plastic model with associated flow.

	$\mathbf{G}$ [kPa]	$\nu$ [-]	$\phi$ [°]	$\psi$ [°]	$\mathbf{a}$ [kPa]	$\mathbf{K}_0$ [-]	$\sigma_3^{\text{init}}$ [kPa]
Set 1	3000	0.3	30	30	1.73	0.6	100
Set 2	3000	0.3	30	30	1.73	0.8	100
Set 3	3000	0.3	30	30	1.73	1.0	100
Set 4	3000	0.3	20	20	1.73	0.6	100

### 4.1.2 Non-Associated Flow in Single Material Point

The linear elastic-perfect plastic model with non-associated flow was tested as described in section 4.1.1. One combination of material parameters and initial stresses were simulated for drained tests of triaxial compression and triaxial extension. The plane strain conditions with non-associated flow give too complicated effective stress paths for any proper verification. Hence, plane strain test simulations were not performed. The parameter combination used in the tested is given in Table 4.2. For comparison, test simulations were also executed using the Mohr–Coulomb model.

**Table 4.2:** Parameter set for validation of linear elastic-perfect plastic model with non-associated flow.

	$\mathbf{G}$ [kPa]	$\nu$ [-]	$\phi$ [°]	$\psi$ [°]	$\mathbf{a}$ [kPa]	$\mathbf{K}_0$ [-]	$\sigma_3^{\text{init}}$ [kPa]
Set 5	3000	0.3	30	0	1.73	0.6	100

### 4.1.3 Loading and Safety Calculations

Safety calculations were executed to detect any difference between the implemented Drucker–Prager model and the given Mohr–Coulomb model in PLAXIS, both linear elastic-perfect plastic models. Drained loading and the drained factor of safety factor on a foundation were calculated for selected sets of material parameters. The geometry of the foundation is shown in Figure 4.1. The  $\alpha$ -coefficient corresponding to plane strain strength of Mohr–Coulomb was chosen.

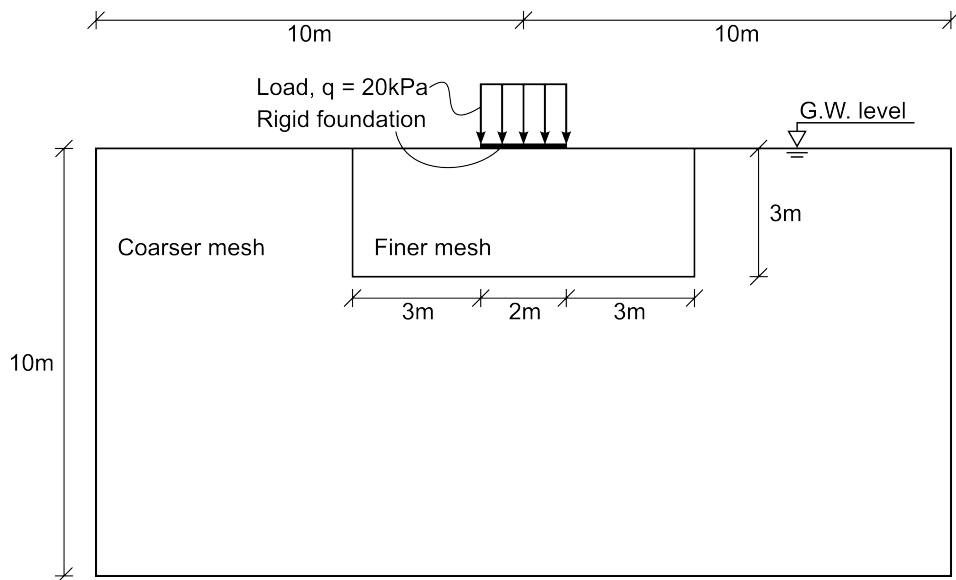


**Figure 4.1:** Geometry of foundation used in the safety calculation.

An evenly distributed load of  $q = 20\text{kPa}$  is applied to a 2m wide weightless, rigid foundation resting on homogenous soil. The soil parameters used in the simulations are summarized in Table 4.3. Different combinations of friction and dilation angles are tested. To obtain comparable results, tensile stresses are allowed for the Mohr–Coulomb model whereas no tension cut-off are implemented in the Drucker–Prager model. As cohesion is given as input in the Mohr–Coulomb model, the attraction in the Drucker–Prager model is modified to correspond to a cohesion  $c = 1\text{kPa}$ .

**Table 4.3:** Material parameters used in safety calculations.

	$\mathbf{G}$ [kPa]	$\nu$ [–]	$\phi$ [°]	$\psi$ [°]	$\mathbf{a}$ [kPa]
Set 6	3000	0.3	30	0	1.732
Set 7	3000	0.3	30	1	1.732
Set 8	3000	0.3	30	2	1.732
Set 9	3000	0.3	30	30	1.732
Set 10	3000	0.3	20	0	2.747
Set 11	3000	0.3	20	20	2.747

The foundation was modeled in PLAXIS. The mesh used in the calculation is shown in Figure 4.2. Characteristic data for the mesh are summarized in

Table 4.4 and coordinates for selected points are shown in Table 4.5.

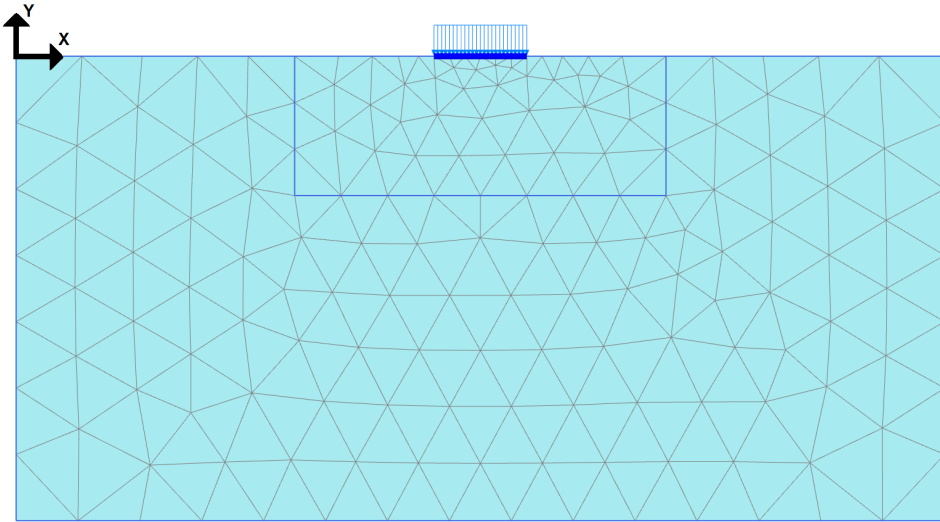


**Figure 4.2:** The mesh used in the calculation.

**Table 4.4:** Characteristic mesh data for the model.

Model	Plane strain
Element type	15-noded triangles
Number of elements	299
Number of nodes	2503
Avg. element size	0.8179m

**Table 4.5:** Coordinates of selected points.

Point	X	Y
A	10.00	0.00
B	9.21	-1.12
K	8.98	-0.03
L	9.11	-1.17

Each parameter set was modeled with four phases, summarized in Table 4.6 with the numerical control parameters for each phase. After the initial phase, a loading phase was defined with application of the full load. Next, a safety calculation was performed with the  $c-\phi$ -reduction option in PLAXIS.

This was done for both the standard Mohr–Colomb model in PLAXIS and the implemented Drucker–Prager model.

To obtain a smoother curve for the implemented Drucker–Prager model in the Safety calculations, the iterative procedure control parameters were adjusted. The desired minimum and maximum number of iterations were set to 2 and 3, respectively, and the over-relaxation factor was set to 1.0. This gives slower convergence, which results in the need for more calculation steps. As a consequence, 1000 additional steps were used. For the Mohr–Colomb model the desired minimum and maximum number of iterations were set to 3 and 4 for the Safety calculations to obtain better correspondence of the two models' results. All other parameters in the Safety calculation and for the loading phase were set to the default parameters.

**Table 4.6:** Numerical control parameters for phases used in the calculation. Non-default values in italic.

Model	Calc. type	Max steps	Over-relaxation factor	Desired min iterations	Desired max iterations
Mohr–Coulomb	Plastic	250	1.2	6	15
	Safety	100	1.2	<i>3</i>	<i>4</i>
Drucker–Prager	Plastic	250	<i>1.0</i>	6	15
	Safety	<i>1000</i>	<i>1.0</i>	<i>2</i>	<i>3</i>

## 4.2 Strain Hardening and Stress Dependent Dilatancy

The strain hardening and stress dependent dilatancy models are tested in PLAXIS.

### 4.2.1 Strain Hardening and Stress Dependent Dilation Angle

To investigate the validity of the stress dependent dilation angle, the model is tested in the *SoilTest*-module in PLAXIS. Undrained triaxial compression tests are performed to see if the model gives dilative and contractive behavior converging to  $p = p_{ref}$ , driven to large strains at  $|\varepsilon_1| = 30\%$ . The material parameters used are summarized in Table 4.7. The triaxial tests are consolidated isotropically to  $\sigma'_3 = 50\text{kPa}$ ,  $\sigma'_3 = 100\text{kPa}$ ,  $\sigma'_3 = 200\text{kPa}$  and  $\sigma'_3 = 400\text{kPa}$ .

For comparison, as far as valid, the Mohr–Coulomb model was also used in simulations.

Some combinations of  $p_{ref}$  and  $\psi_0$  has been tested to find the mean stress at large strains.

#### 4.2.2 Strain Hardening and Stress Dependent Dilation Coefficient

The model is tested as in the last section for undrained triaxial tests with isotropic consolidation to  $\sigma'_3 = 100\text{kPa}$ ,  $\sigma'_3 = 200\text{kPa}$  and  $\sigma'_3 = 400\text{kPa}$ . The parameters used are the same as in last section and are given Table 4.7. For comparison, the linear elastic-perfect plastic Mohr–Coulomb model is tested.

**Table 4.7:** Parameter set for validation of the strain hardening and stress dependent dilation coefficient model.

	<b>G</b> [kPa]	$\nu$ [-]	$\phi$ [°]	$\psi_0$ [°]	<b>a</b> [kPa]	<b>H<sub>0</sub></b> [-]	<b>p<sub>ref</sub></b> [kPa]
Set 12	3000	0.3	30	10	1.73	1000	200

### 4.3 Void Ratio Dependent Dilatancy

Using the initial and critical void ratios to define the dilatancy, the reference mean stress, and hence the dilatancy behavior, may be controlled. The model is used to simulate triaxial tests by Verdugo (1992).

#### 4.3.1 Simulation of Toyoura Sand with Constant Elastic Stiffness

Verdugo (1992) executed a number of undrained triaxial compression tests on Toyoura sand. All tests were consolidated to isotropically to initial mean stresses in the range of  $1\text{kgf/cm}^2$ – $30\text{kgf/cm}^2$ . The unit  $\text{kgf/cm}^2$  correspond to the pressure of 1kg distributed over an area of  $1\text{cm}^2$ , or  $1\text{kgf/cm}^2 = 98.1\text{kPa}$ . In the tests the void ratios are held constant during the shearing process.

The initial void ratio  $e_0$  and the friction angle at steady state  $\phi = 31.5^\circ$  is given by Verdugo (1992, p. 191). The sand is cohesionless. As no dilation angle or Poisson’s ratio is given they had to be assumed. The dilation angle chosen in accordance with equation (2.75) giving  $\psi_0 = 1.5^\circ$ , and a Poisson’s ratio is set to  $\nu = 0.3$  as a proper choice for loading conditions.



Simulations were executed by using *SoilTest*-module in PLAXIS. Undrained triaxial compression tests were, driven to large strains at  $|\varepsilon_1| = 30\%$ .

The steady state line, or critical state line, for the Toyoura sand is reproduced in Figure 4.3. By extrapolation to  $p = 1\text{kPa}$  with the inclination of the lower stress range, it was found that  $e_\lambda = 0.974$  and  $\lambda^* = 0.03$ . However, the assumption of a linear relation does not fit the whole stress range. As a remedy, different sets of  $e_\lambda$  and  $\lambda^*$  are used for the different tests to give the correct reference mean stress. In other words, the parameters are here fitted to obtain the reference stress  $p_{ref}$  at critical state, such that the correct final mean and deviatoric stress are reached.

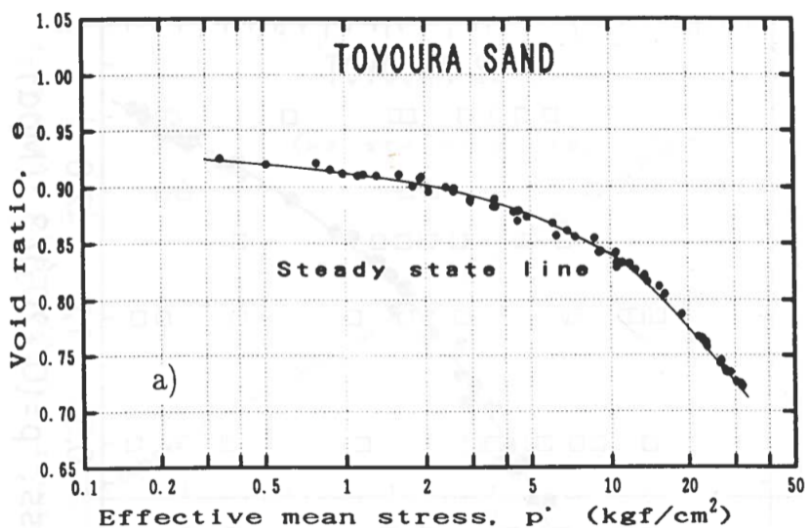


**Figure 4.3:** Void ratio-mean stress critical state line for Toyoura sand (Verdugo, 1992, Figure 4.17a).

To better simulate the triaxial tests, the constant elastic stiffness was adjusted with the initial mean stress  $p_{init}$ . The shear stiffness was adjusted by a reference stiffness  $G^*$  at a reference stress  $p^* = 10\text{kgf/cm}^2 = 981\text{kPa}$  as:

$$G = G^* \sqrt{\frac{p_{init}}{p^*}} \quad (4.1)$$

These parameters and the plastic stiffness  $H_0$  were optimized by trial-and-error to give the best simulation of the triaxial tests. It has been emphasized to keep the values as constant as possible, while still giving a realistic simulation of the tests. Three different void ratios was tested,  $e = 0.735$ ,  $e = 0.833$  and  $e = 0.906 - 908$  by Verdugo (1992). The tests for void ratios  $e = 0.906 - 908$  is

regarded as the same void ratio, but a slight modification of the  $\lambda^*$ -parameter was done for the simulations. All parameters are summarized in Table 4.8

**Table 4.8:** Material parameters for the triaxial tests on Toyoura sand with constant elastic stiffness.

$e_0$ [-]	$\mathbf{G}^*$ [MPa]	$\mathbf{p}^*$ [kPa]	$\nu$ [-]	$\phi$ [°]	$\psi_0$ [°]	$\mathbf{a}$ [kPa]	$\mathbf{H}_0$ [-]	$e_{ss}$ [-]	$\lambda^*$ [-]
0.735	884	981	0.3	31.5	1.5	0	50	0.9740	0.0691
0.833	1387	981	0.3	31.5	1.5	0	50	0.9740	0.0467
0.906 (0.908)	235	981	0.3	31.5	1.5	0	50	0.9740	0.0309 (0.0300)

### 4.3.2 Simulation of Toyoura Sand with Mean Stress Dependent Stiffness

The triaxial tests on Toyoura sand are simulated again when applying the mean stress dependency of the stiffness in equation (3.25). Apart from the reference shear stress  $G^*$  and plastic initial stiffness  $H_0$ , all parameters are the same as in the last section and are summarized in Table 4.9.

**Table 4.9:** Material parameters for the triaxial tests on Toyoura sand with stress dependent elastic stiffness.

$e_0$ [-]	$\mathbf{G}^*$ [MPa]	$\mathbf{p}^*$ [kPa]	$\nu$ [-]	$\phi$ [°]	$\psi_0$ [°]	$\mathbf{a}$ [kPa]	$\mathbf{H}_0$ [-]	$e_{ss}$ [-]	$\lambda^*$ [-]
0.735	1275	981	0.3	31.5	1.5	0	40	0.9740	0.0691
0.833	700	981	0.3	31.5	1.5	0	30	0.9740	0.0467
0.906 (0.908)	235	981	0.3	31.5	1.5	0	40	0.9740	0.0309 (0.0300)

# Chapter 5

## Results from Calculations

Results from the testing procedures described in the last chapter are presented. Relevant plots and selected tables are presented to summarize the behavior of the model.

### 5.1 Linear Elastic-Perfect Plastic Model

Results from the simulations with the linear elastic-perfect plastic model are presented in a range of plots.

#### 5.1.1 Associated Flow

Results from triaxial compression tests are plotted in Figures 5.1 and 5.2. Triaxial extension test results are found in Figures 5.3 and 5.4, while the plane strain tests are plotted in Figures 5.5-5.8. All test simulations are drained.

The projection of the stresses onto the deviatoric plane ( $\Pi$ -plane) are also plotted for a selection of the tests. The triaxial tests of Set 1 is plotted in normalized coordinates in Figure 5.9. Plane strain test of Set 3 is plotted in Figure 5.10 in the  $\Pi$ -plane, while all the plane strain tests are also plotted in normalized coordinates in Figures 5.11 and 5.12. Table 5.1 gives the failure stress state of the drained plane strain test of Set 3 (point F in Figures 5.7 and 5.10). The  $\alpha$ -coefficient for the material is also given in the table.

**Table 5.1:** Stress state at failure point F for the drained plane strain test of Set 3.

<b>Stresses at point F</b>		
$\sigma_1 = 303.47\text{kPa}$	$s_1 = 84.82\text{kPa}$	$p = 218.65\text{kPa}$
$\sigma_2 = 252.48\text{kPa}$	$s_2 = 33.83\text{kPa}$	$\sqrt{J_2} = 105.87\text{kPa}$
$\sigma_3 = 100.00\text{kPa}$	$s_3 = -118.65\text{kPa}$	$\alpha = 0.1601$

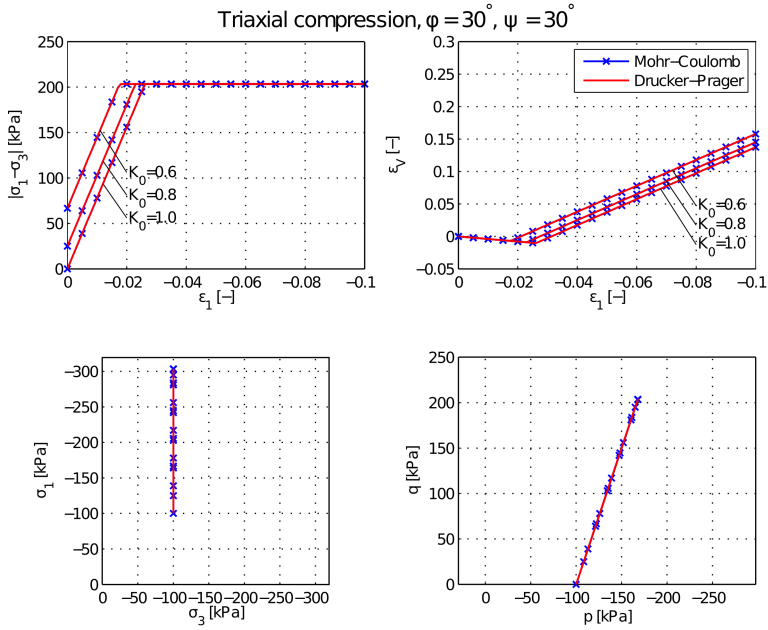


Figure 5.1: Drained triaxial compression tests of Set 1-3.

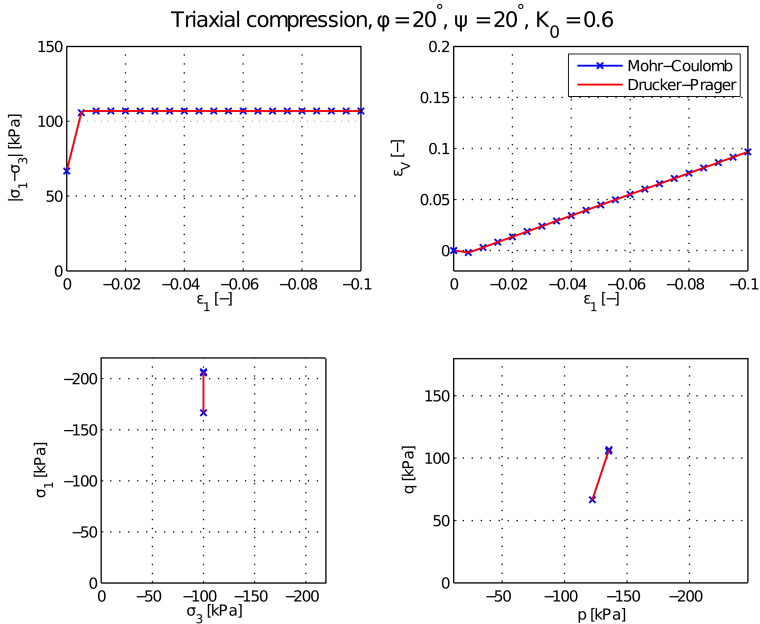


Figure 5.2: Drained triaxial compression tests of Set 4.

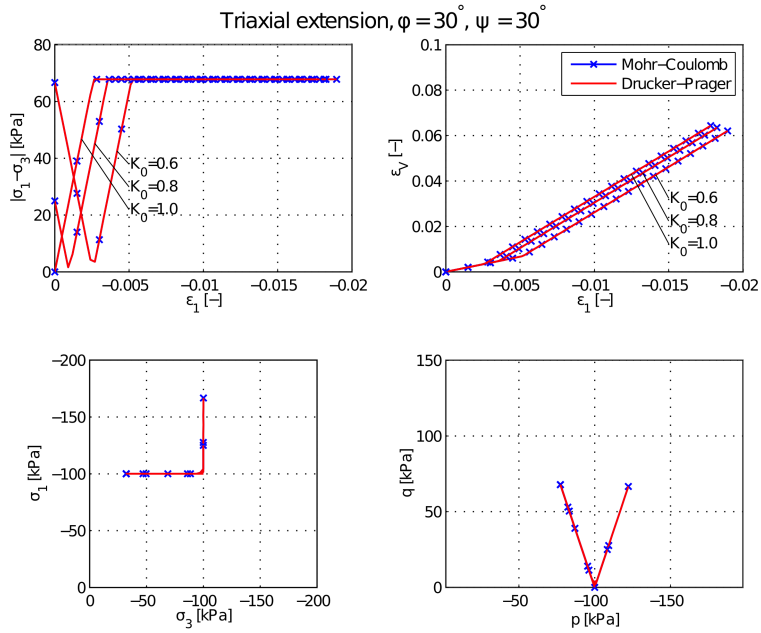


Figure 5.3: Drained triaxial extension tests of Set 1-3.

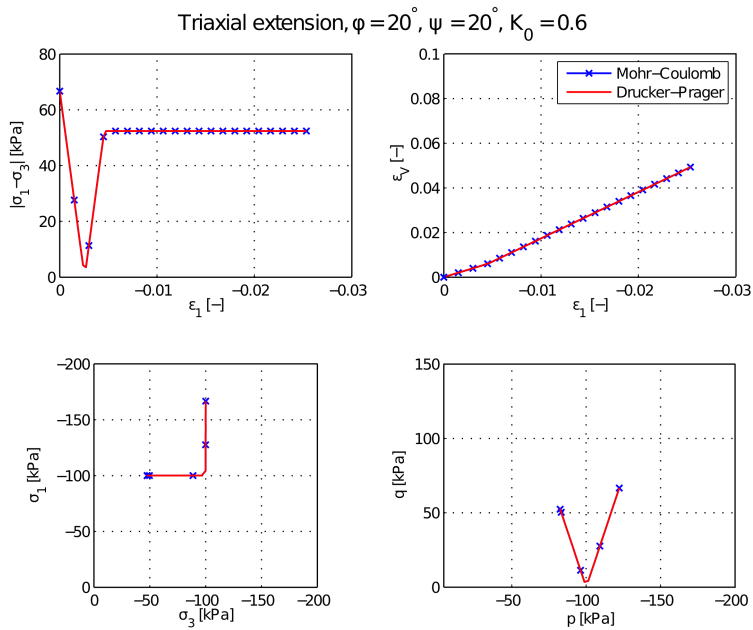


Figure 5.4: Drained triaxial compression tests of Set 4.

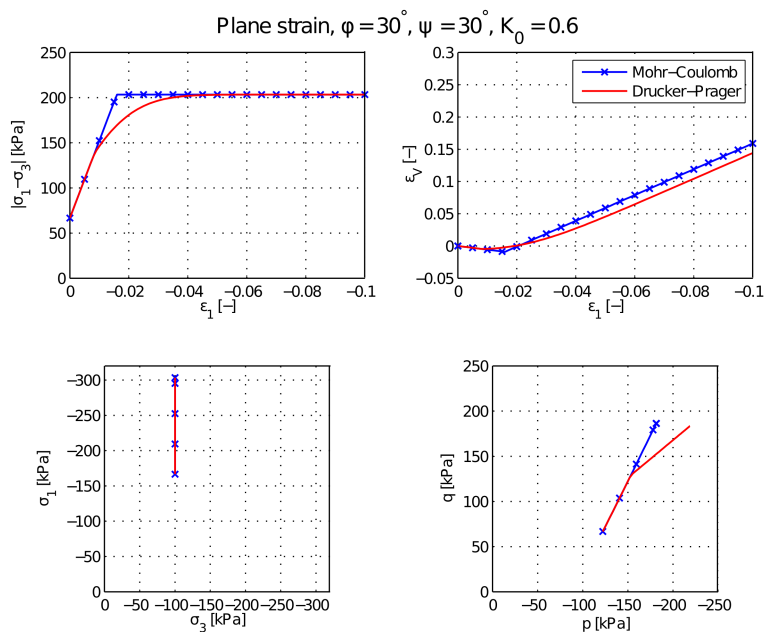


Figure 5.5: Drained plane strain test of Set 1.

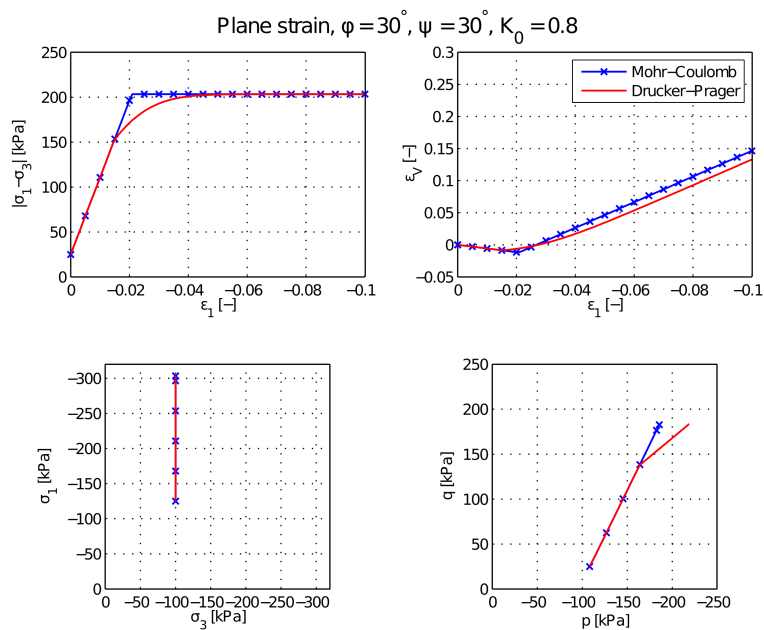


Figure 5.6: Drained plane strain test of Set 2.

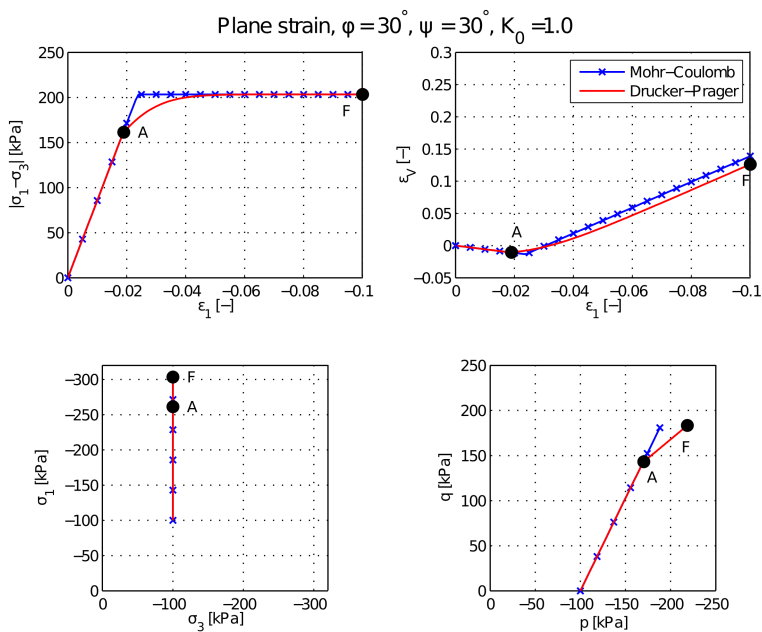


Figure 5.7: Drained plane strain test of Set 3.

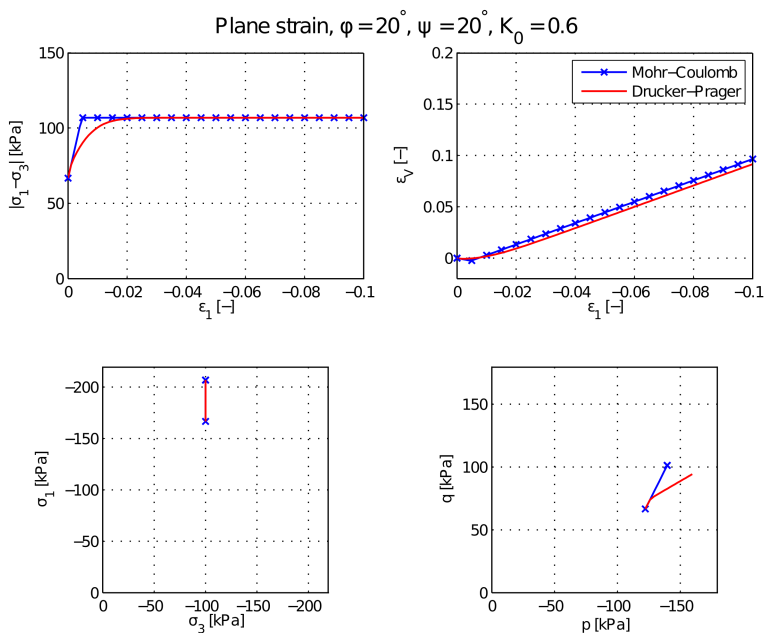
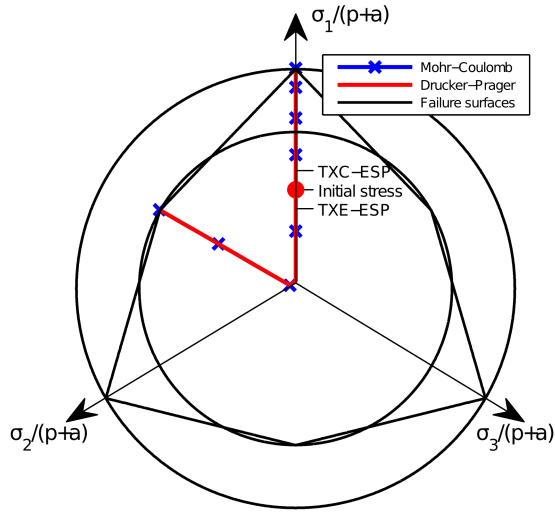
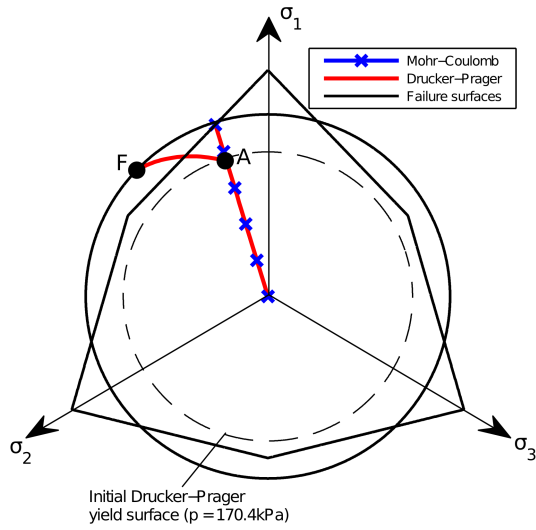


Figure 5.8: Drained plane strain test of Set 4.





**Figure 5.9:** Drained triaxial tests of Set 1 in normalized coordinates in deviatoric plane with the relevant yield surfaces.



**Figure 5.10:** Drained plane strain test of Set 3 in deviatoric plane.

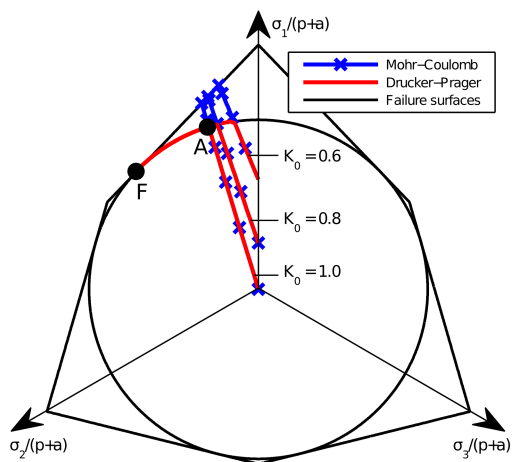


**Figure 5.11:** Drained plane strain test of Set 1-3 in normalized coordinates in deviatoric plane.

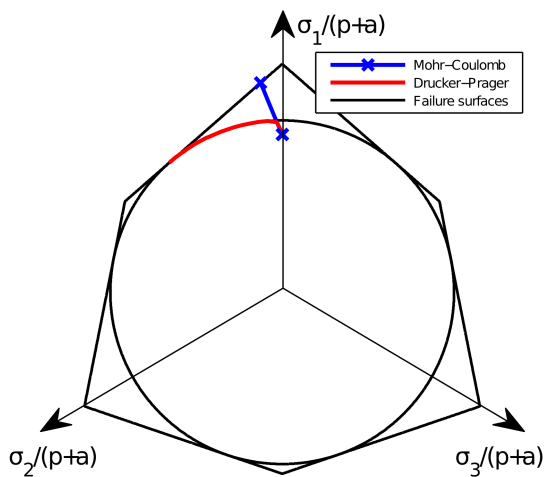


**Figure 5.12:** Drained plane strain test of Set 4 in normalized coordinates in deviatoric plane.

### 5.1.2 Non-Associated Flow

Results from the triaxial compression and extension tests are plotted in Figures 5.13 and 5.14, respectively.

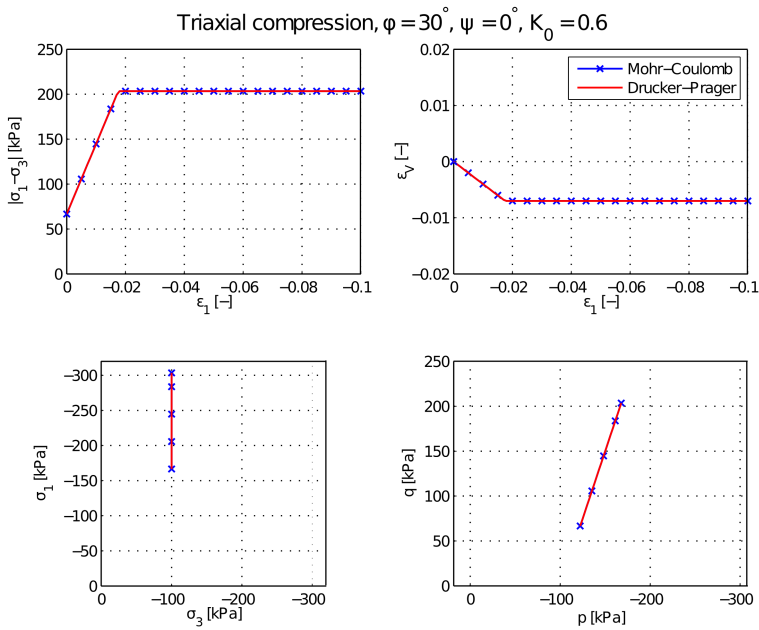


Figure 5.13: Drained triaxial compression tests of Set 5.

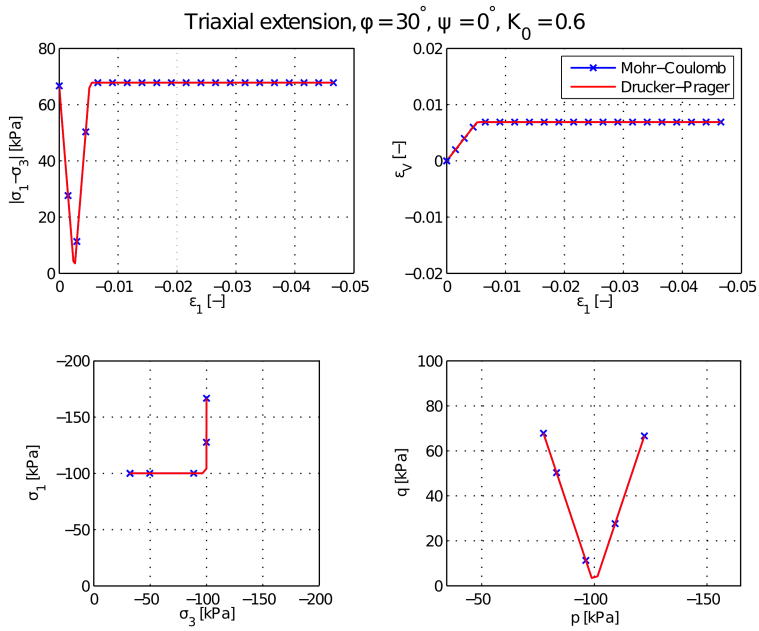


Figure 5.14: Drained triaxial extension tests of Set 1-3.

### 5.1.3 Loading and Safety Calculations

The vertical deformation of point A,  $|u_{y,A}|$ , after the loading phases is tabulated together with the final safety factor of the calculations in Table 5.2. In addition, the relative differences between the models are calculated. For material parameter Set 8 and 9, selected figures are shown. Figures 5.15–5.16 show the absolute value of the vertical deformation of point A plotted versus the  $\Sigma$ Mstage-multiplier for the loading calculations. This gives comparable results for the stiffness of the models.

The total deformation of point A is plotted versus  $\Sigma$ Msf-multiplier, i.e. the factor of safety, in Figures 5.17–5.18 for the same material parameter sets. For full documentation of the results of all material parameter sets, see Appendix E. It should be noted that the Mohr–Coulomb model gives extensive deformations that are way larger than the Drucker–Prager model at failure. The plotted interval does not cover these deformations, in order to see the behavior of the Drucker–Prager model.

**Table 5.2:** Summary of results from loading and safety calculations.

$\phi$ [°]	$\psi$ [°]	Mohr–Coulomb		Drucker–Prager		Deviations	
		$ u_{y,A} $ [mm]	$\Sigma$ Msf [–]	$ u_{y,A} $ [mm]	$\Sigma$ Msf [–]	$ u_{y,A} $ [%]	$\Sigma$ Msf [%]
30	0	7.63	2.33	9.03	2.30	18.3	–1.3
	1	7.62	2.34	8.95	2.32	17.5	–0.9
	2	7.61	2.34	8.87	2.33	16.6	–0.4
	30	7.41	2.34	7.80	2.36	5.3	0.9
20	0	13.84	1.61	17.60	1.59	27.2	–1.2
	20	10.04	1.61	11.72	1.62	16.7	0.6

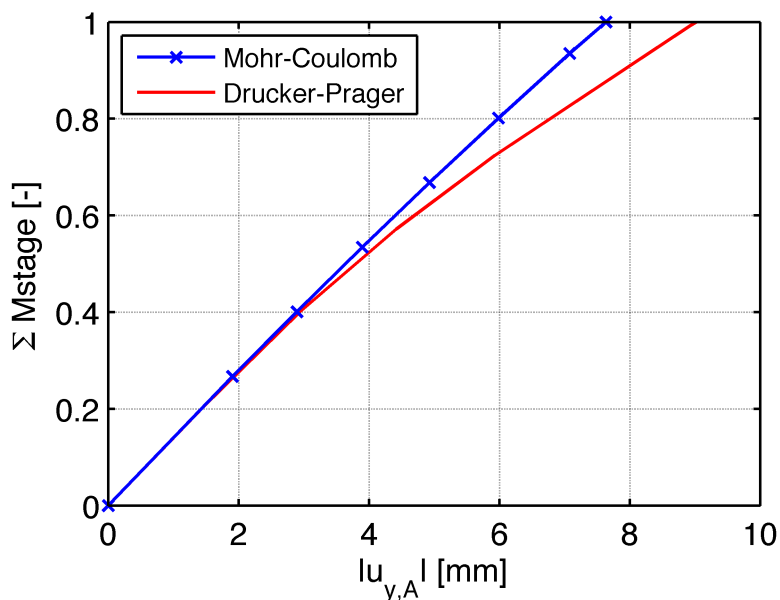


Figure 5.15: Load-deformation curve for material parameter Set 8 ( $\phi = 30^\circ$ ,  $\psi = 2^\circ$ ).

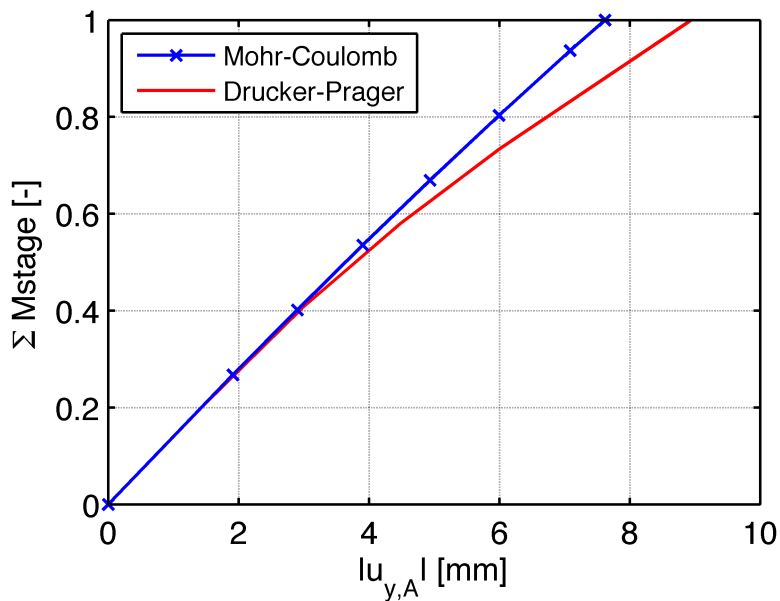


Figure 5.16: Load-deformation curve for material parameter Set 9 ( $\phi = 30^\circ$ ,  $\psi = 30^\circ$ ).

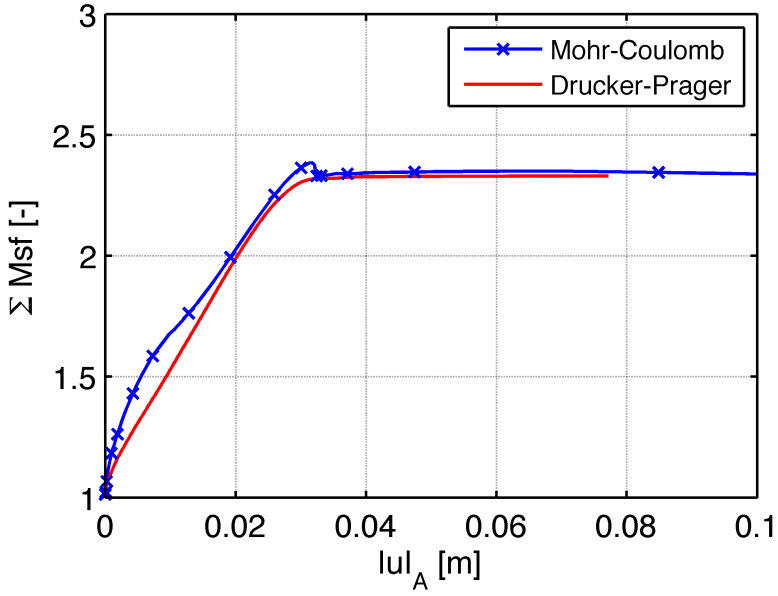


Figure 5.17: Safety factor-deformation curve for parameter Set 8 ( $\phi = 30^\circ$ ,  $\psi = 2^\circ$ ).

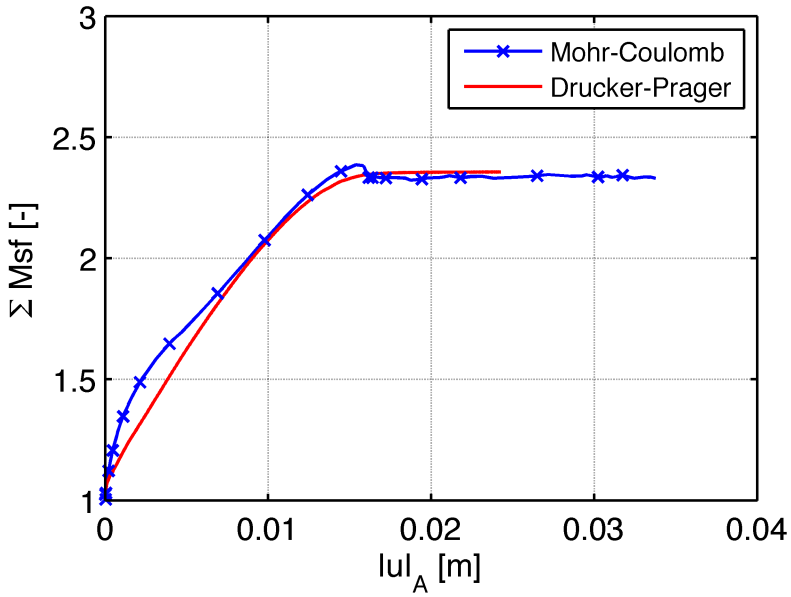
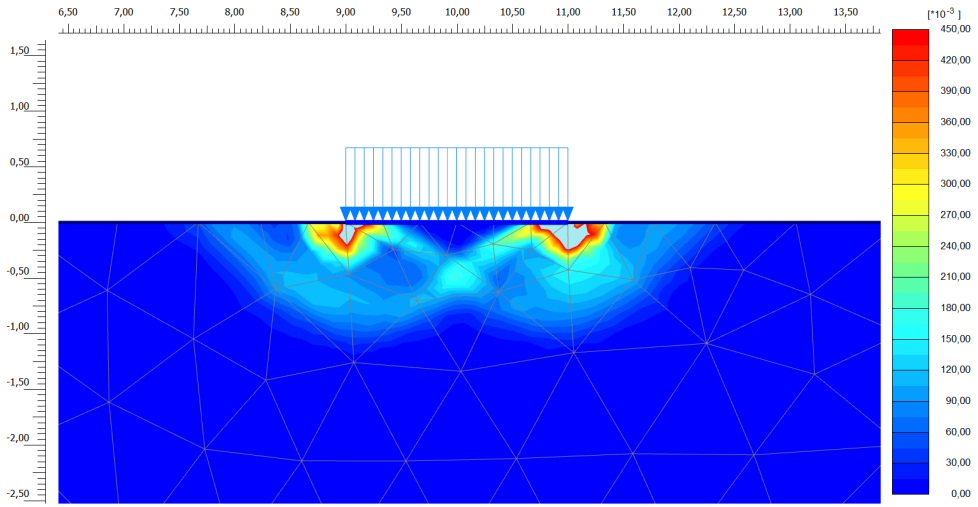
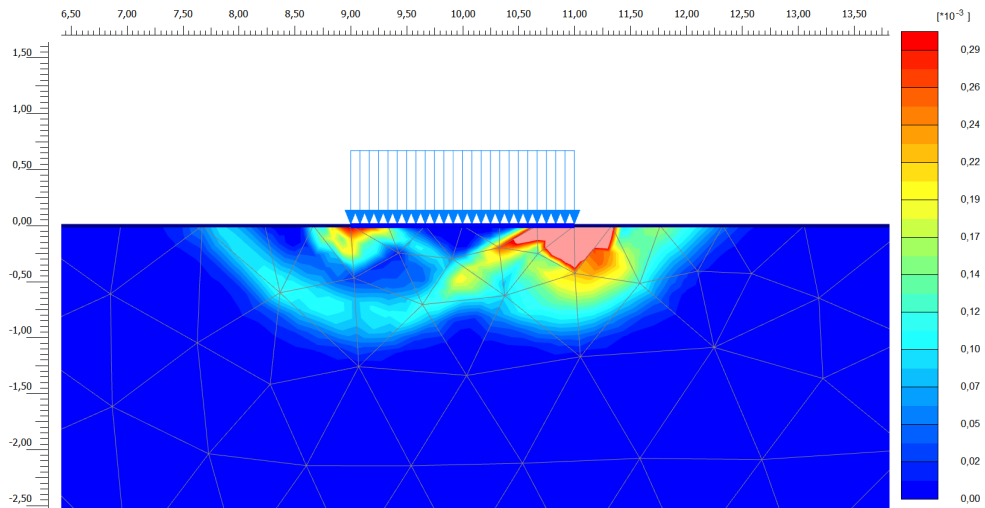


Figure 5.18: Safety factor-deformation curve for parameter Set 9, with friction ( $\phi = 30^\circ$ ,  $\psi = 30^\circ$ ).



**Figure 5.19:** Shadings of incremental shear strains at failure for Mohr–Coulomb model with material parameter Set 8 ( $\phi = 30^\circ$ ,  $\psi = 2^\circ$ ).



**Figure 5.20:** Shadings of incremental shear strains at failure for Drucker–Prager model with material parameter Set 8 ( $\phi = 30^\circ$ ,  $\psi = 2^\circ$ ).



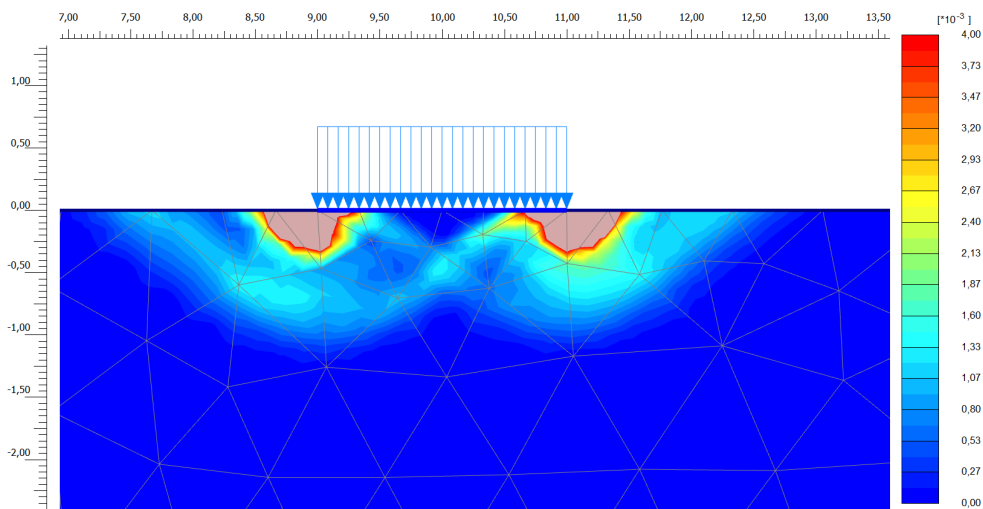


**Figure 5.21:** Shadings of incremental shear strains at failure for Mohr–Coulomb model with material parameter Set 9 ( $\phi = 30^\circ$ ,  $\psi = 30^\circ$ ).

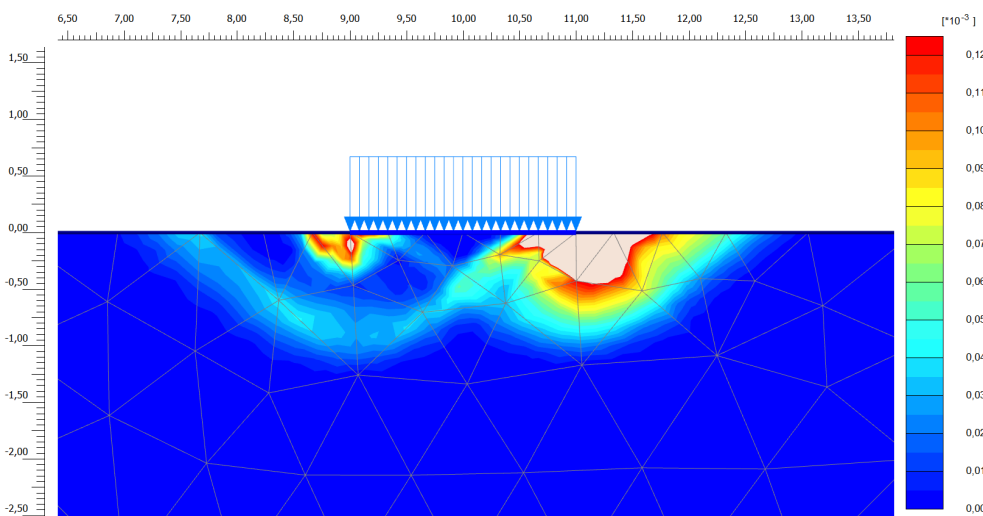


**Figure 5.22:** Shadings of incremental shear strains at failure for Drucker–Prager model with material parameter Set 9 ( $\phi = 30^\circ$ ,  $\psi = 30^\circ$ ).

## 5.2 Strain Hardening and Stress Dependent Dilatancy

The strain hardening and stress dependent dilatancy models are tested in PLAXIS to confirm that the model behaves as expected.

### 5.2.1 Strain Hardening and Stress Dependent Dilation Angle

Plots for the undrained triaxial tests are shown in Figures 5.23-5.26. As the Mohr–Coulomb dilates infinitely, only the parts relevant for comparison are included in the figures. A  $p$ - $q$ -plot showing effective stress paths of all the tests is shown in Figure 5.27. Some combinations of  $p_{ref}$  and  $\psi_0$  has also been tested to find the mean stress at large strains, and are shown in Table 5.3.

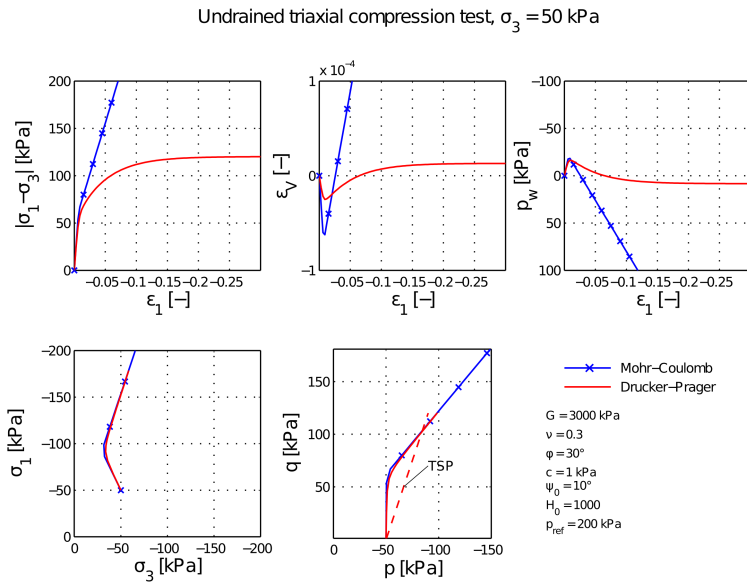


Figure 5.23: Undrained triaxial compression test consolidated to  $\sigma_3 = 50$  kPa.

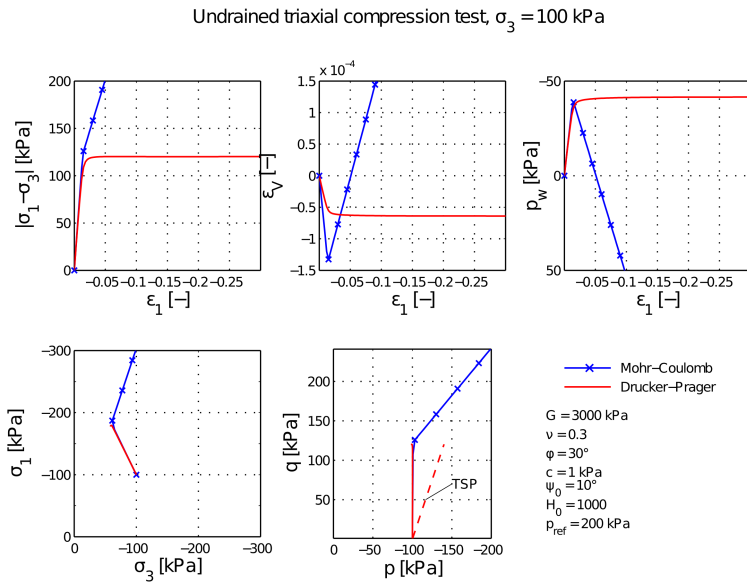


Figure 5.24: Undrained triaxial compression test consolidated to  $\sigma_3 = 100$  kPa.

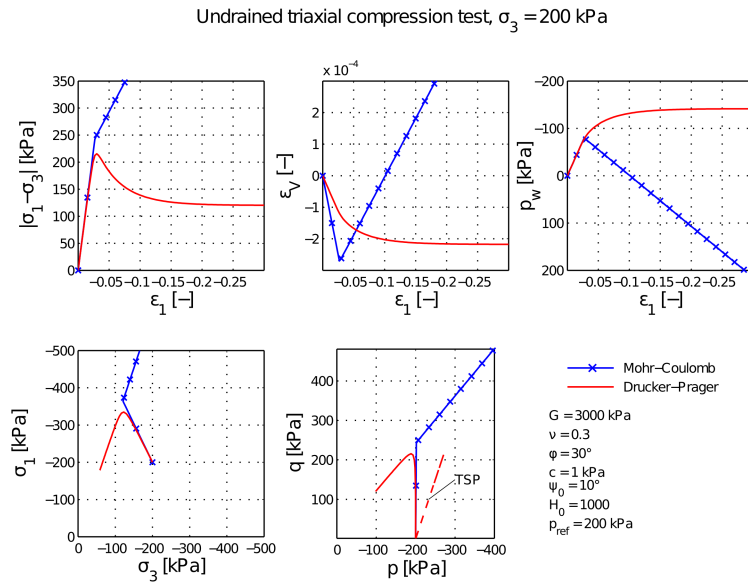


Figure 5.25: Undrained triaxial compression test consolidated to  $\sigma_3 = 200$  kPa.

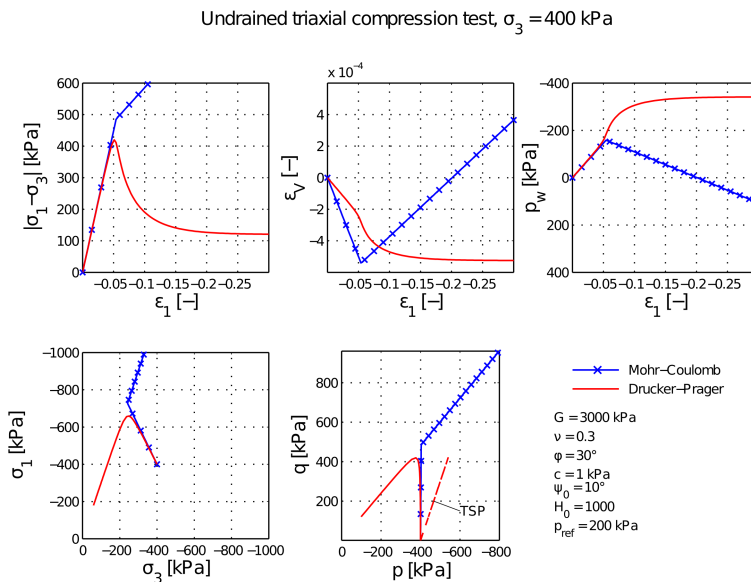
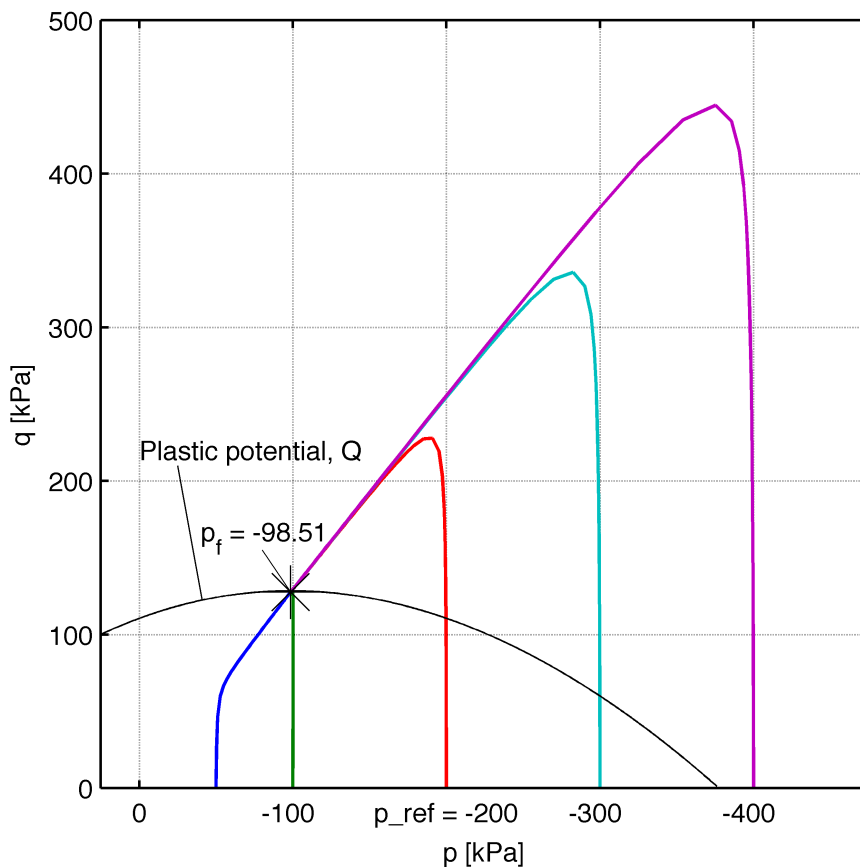


Figure 5.26: Undrained triaxial compression test consolidated to  $\sigma_3 = 400$  kPa.



**Figure 5.27:** Effective stress paths for all undrained triaxial tests with mean stress and plastic potential function  $Q$  at large strains.

**Table 5.3:** Failure mean stress for some reference stresses and dilation angles.

$\mathbf{p}_{ref}$ [kPa]	$\psi_0$ [°]	$\mathbf{p}_f$ [kPa]
50	5	24.82
	10	24.63
100	5	49.71
	10	49.25
200	5	99.31
	10	98.51

## 5.2.2 Strain Hardening and Stress Dependent Dilation Coefficient

Plots for the undrained triaxial tests are shown in Figures 5.28-5.30. As the Mohr–Coulomb dilates infinitely, only the parts relevant for comparison are included in the figures. A  $p$ - $q$ -plot showing the effective stress paths of all the tests is shown in Figure 5.31 and a stress-strain-plot of all the tests is shown in 5.32.

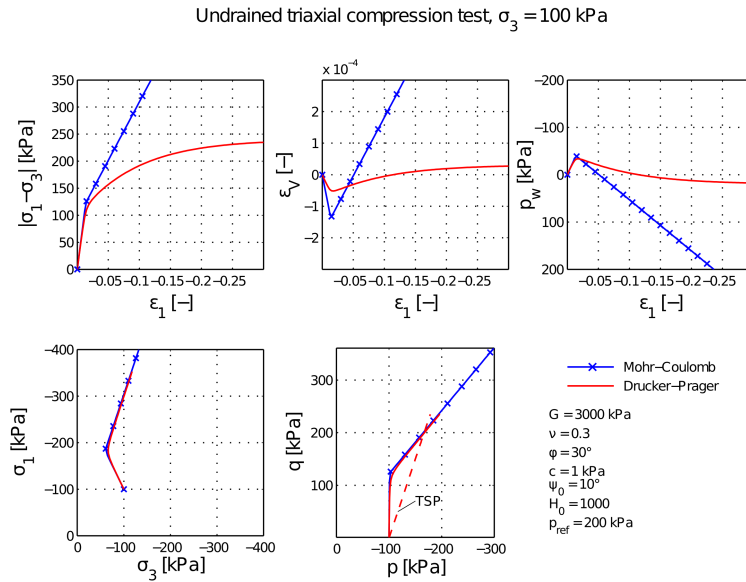


**Figure 5.28:** Undrained triaxial compression test consolidated to  $\sigma_3 = 100$  kPa.

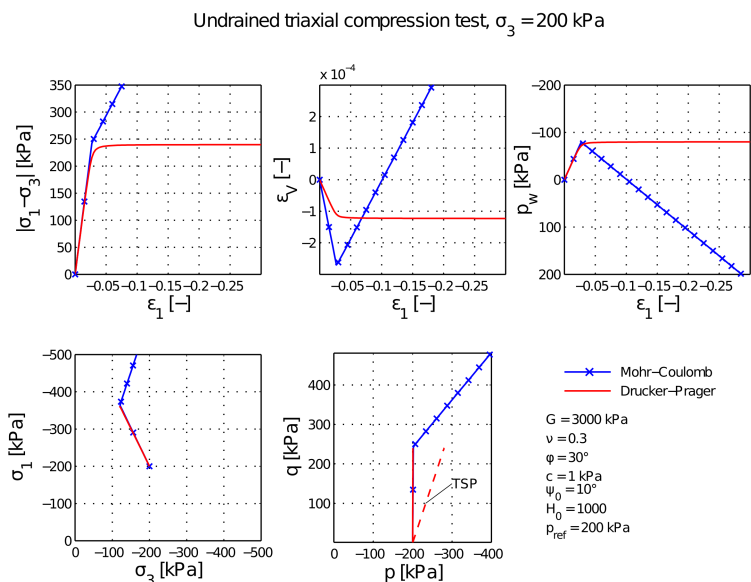


Figure 5.29: Undrained triaxial compression test consolidated to  $\sigma_3 = 200$  kPa.

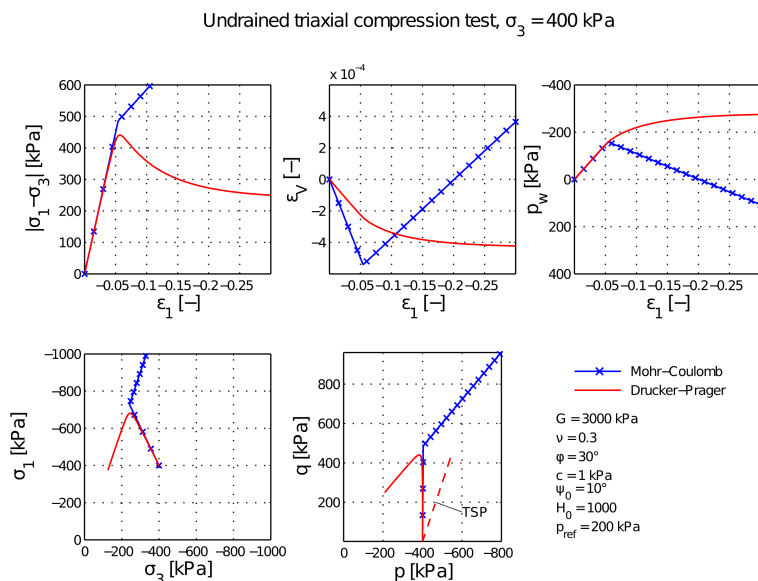
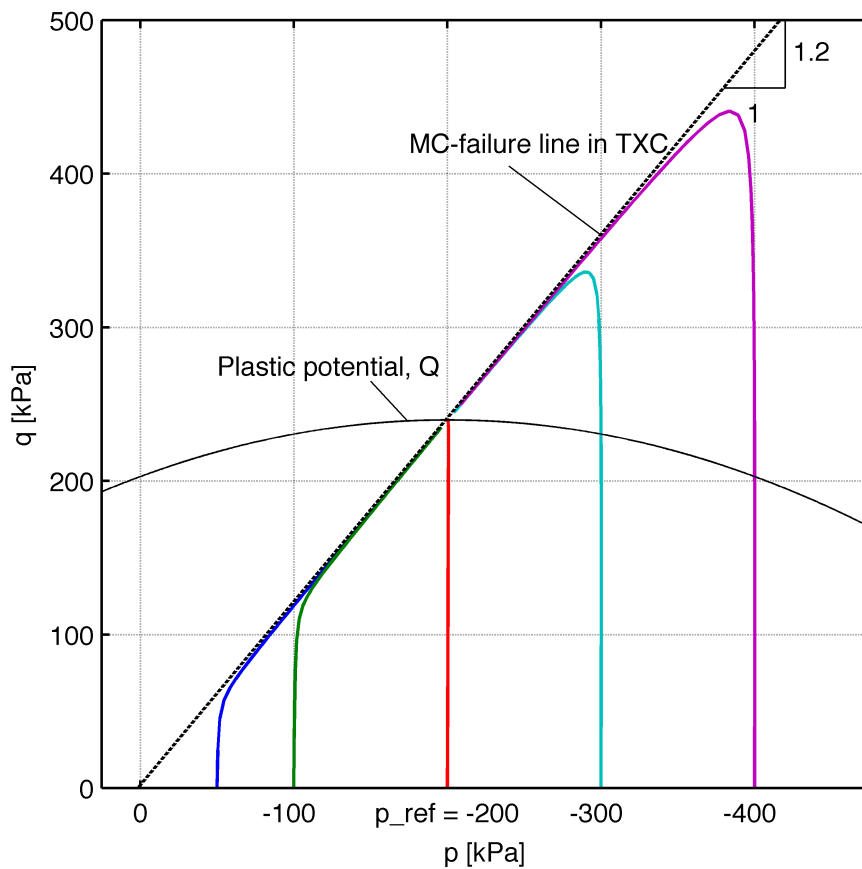


Figure 5.30: Undrained triaxial compression test consolidated to  $\sigma_3 = 400$  kPa.



**Figure 5.31:** Effective stress paths for all undrained triaxial tests with mean stress and plastic potential function  $Q$  at large strains.



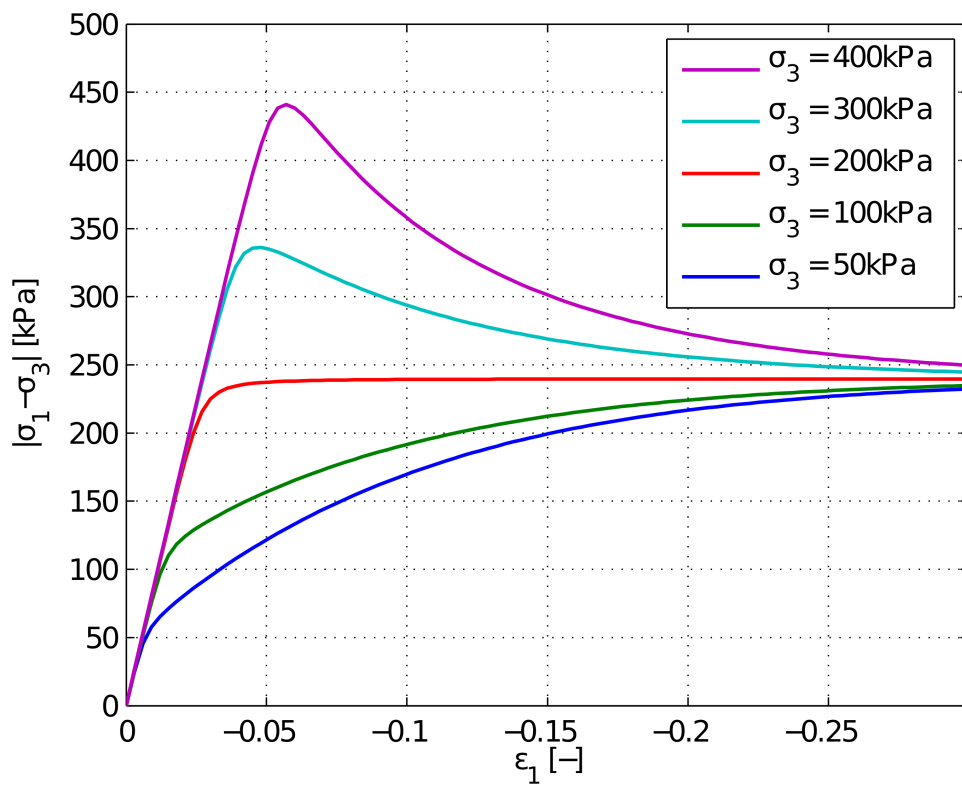


Figure 5.32: Stress-strain-plot for all undrained triaxial tests.

### 5.3 Void Ratio Dependent Dilatancy

The triaxial tests by Verdugo (1992) were simulated with the model.

#### 5.3.1 Simulation of Toyoura Sand with Constant Elastic Stiffness

Simulations from the *SoilTest*-application in PLAXIS are shown in Figures 5.33-5.38, plotted over the original tests by Verdugo (1992). The reader should be aware of that the figures from Verdugo (1992) are somewhat modified. First, the figures are stretched to obtain kPa as unit rather than kgf/cm<sup>2</sup>, second, the  $p$ - $q$ -plots are scaled in order to make the axes equal.

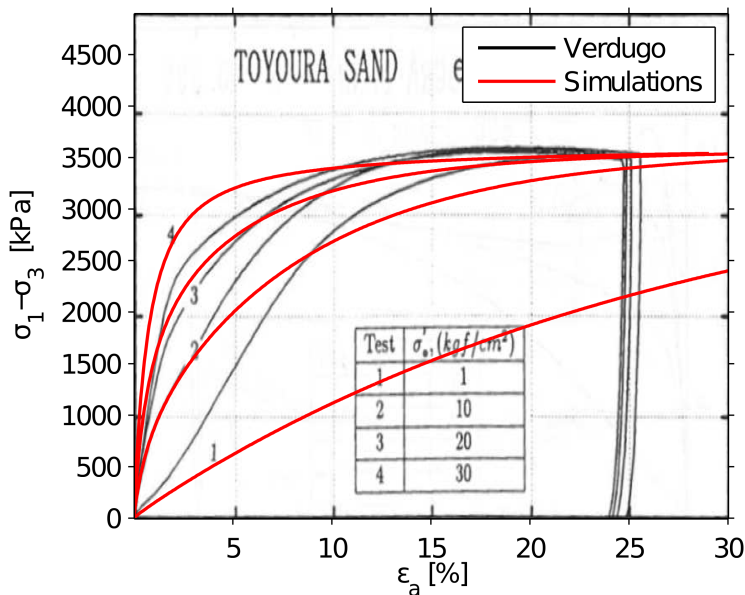


**Figure 5.33:** Stress-strain curves of undrained triaxial tests on sand with void ratio  $e = 0.735$  (Verdugo, 1992, Figure 4.11a).

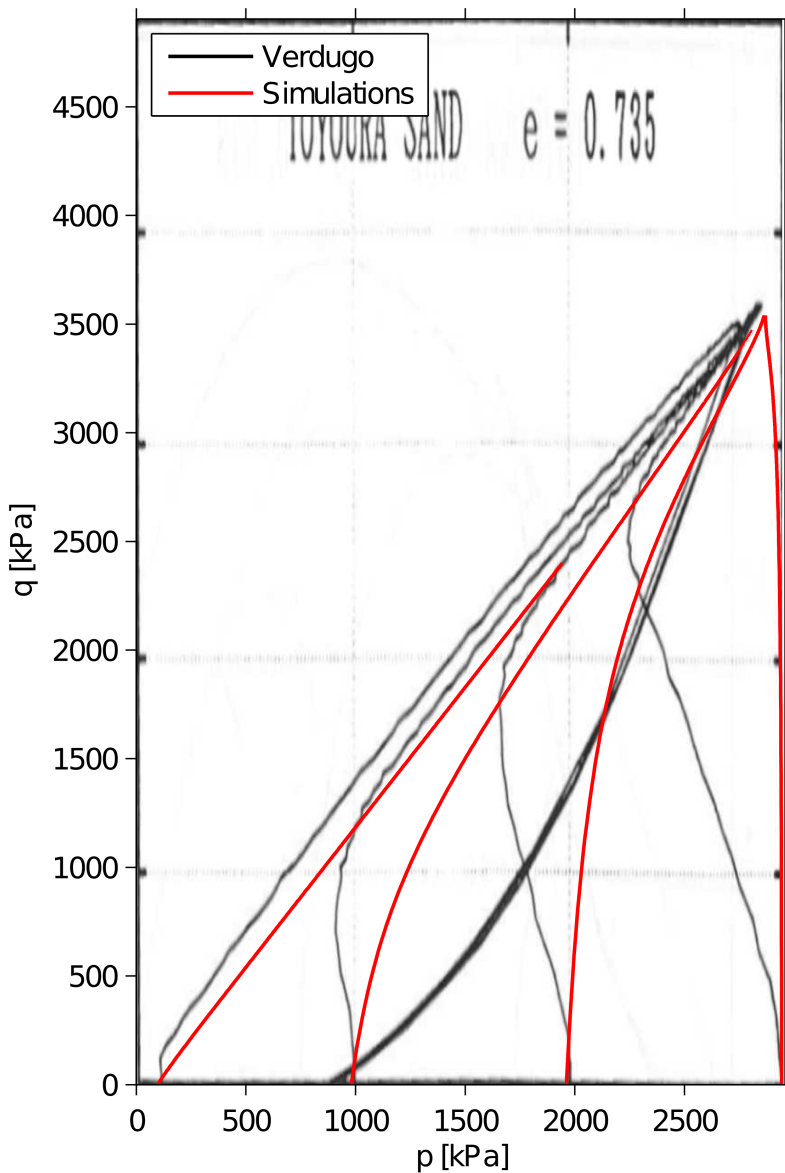


**Figure 5.34:** Effective stress paths of undrained triaxial test on sand with void ratio 0.735 (Verdugo, 1992, Figure 4.11b ).

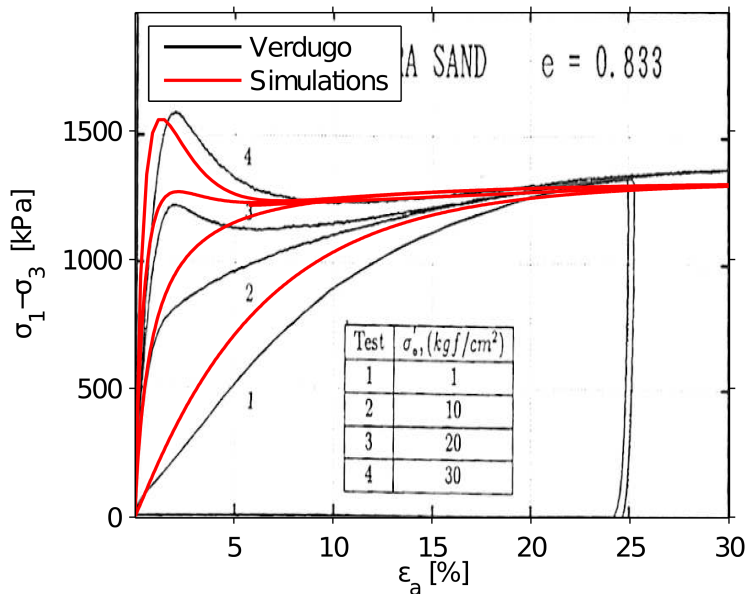


**Figure 5.35:** Stress-strain curves of undrained triaxial tests on sand with void ratio  $e = 0.833$  (Verdugo, 1992, Figure 4.10a).

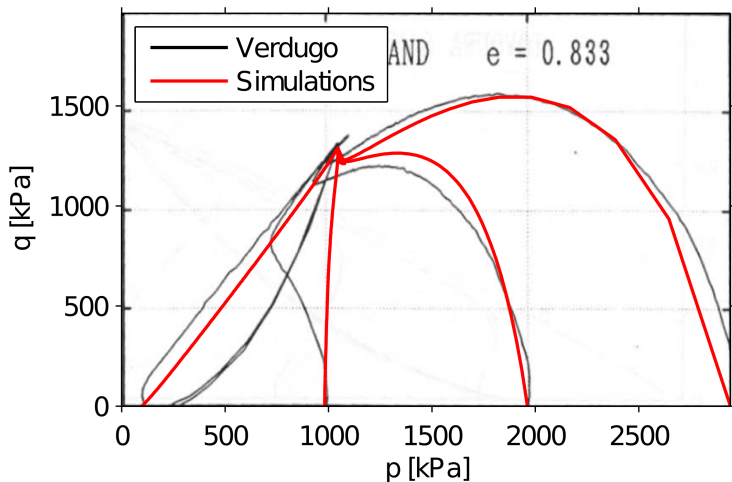


**Figure 5.36:** Effective stress paths of undrained triaxial test on sand with void ratio 0.833 (Verdugo, 1992, Figure 4.10b).

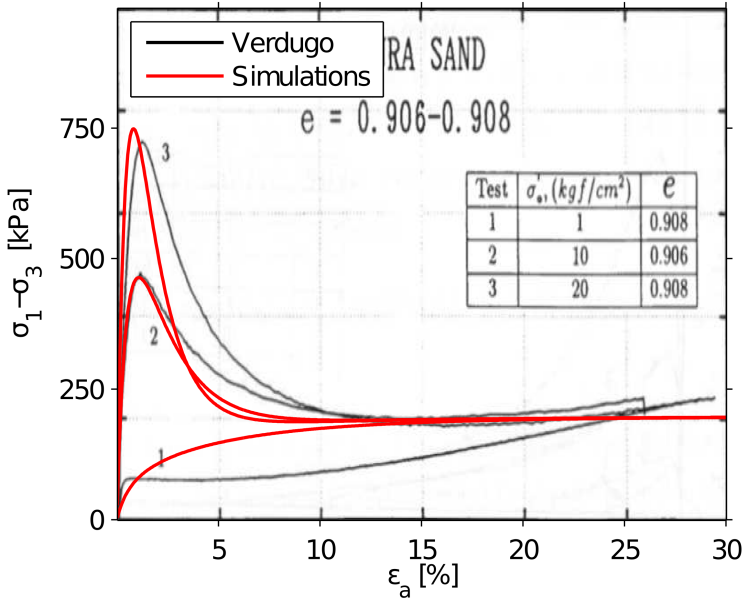


**Figure 5.37:** Stress-strain curves of undrained triaxial tests on sand with void ratio  $e = 0.906-0.908$  (Verdugo, 1992, Figure 4.9a) .

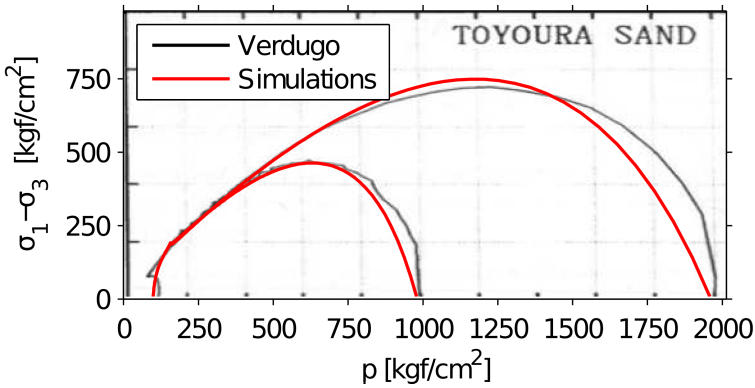


**Figure 5.38:** Effective stress paths of undrained triaxial test on sand with void ratio  $e = 0.906-0.908$  (Verdugo, 1992, Figure 4.9b) .

### 5.3.2 Simulation of Toyoura Sand with Mean Stress Dependent Stiffness

Simulations from the *SoilTest*-application in PLAXIS are shown in Figures 5.39-5.44, plotted over the original tests by Verdugo (1992). The reader should be aware of that the figures are still modified as described in last section.

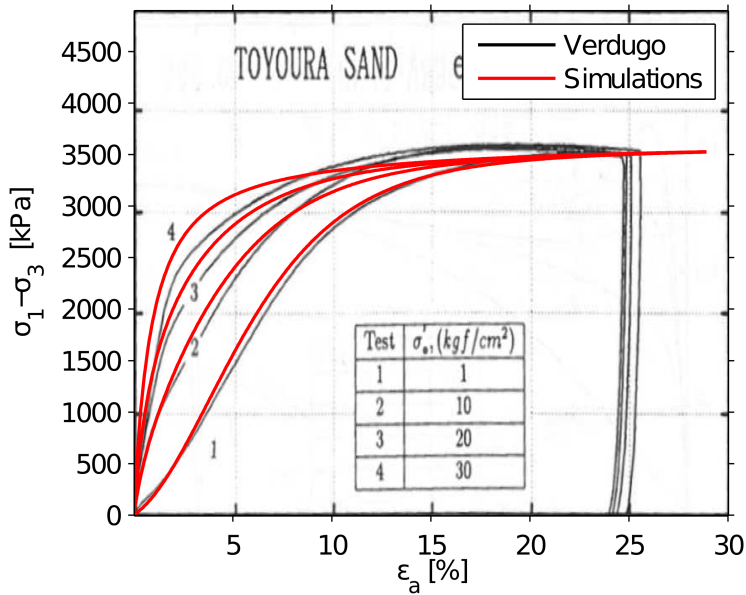


**Figure 5.39:** Stress-strain curves of undrained triaxial tests on sand with void ratio  $e = 0.735$  (Verdugo, 1992, Figure 4.11a ).

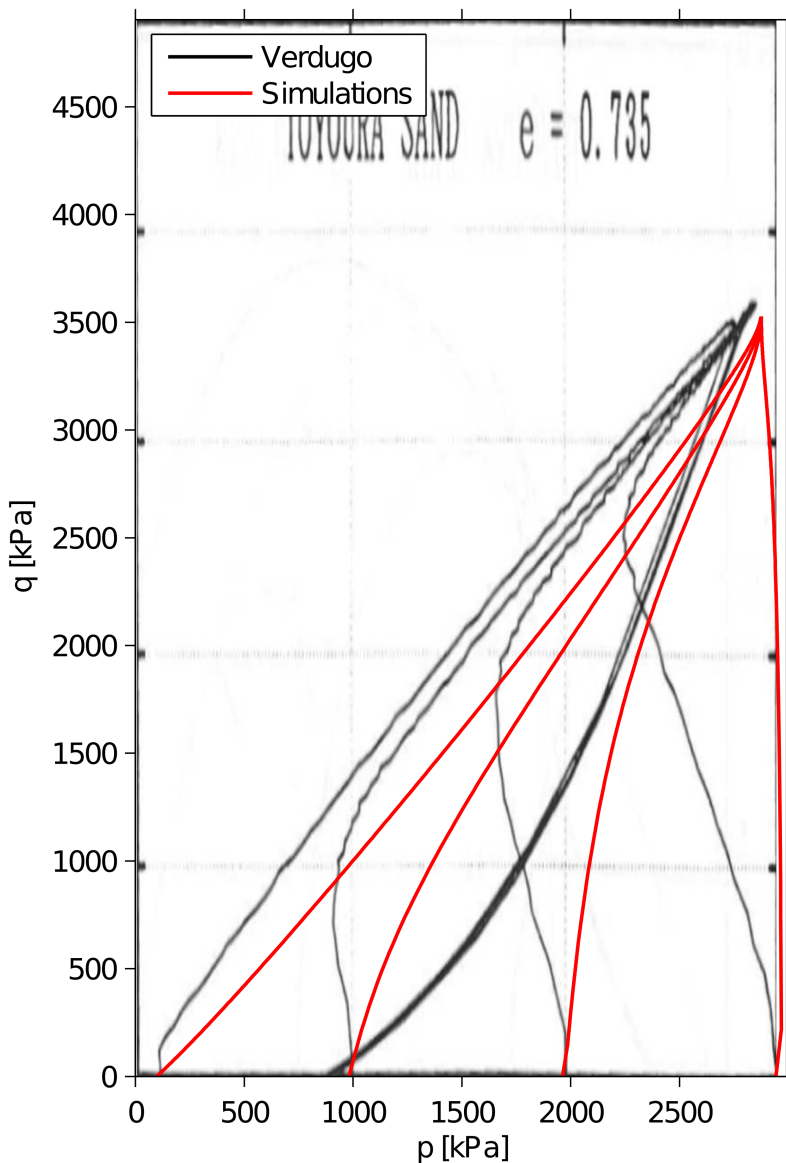


**Figure 5.40:** Effective stress paths of undrained triaxial test on sand with void ratio 0.735 (Verdugo, 1992, Figure 4.11b ).

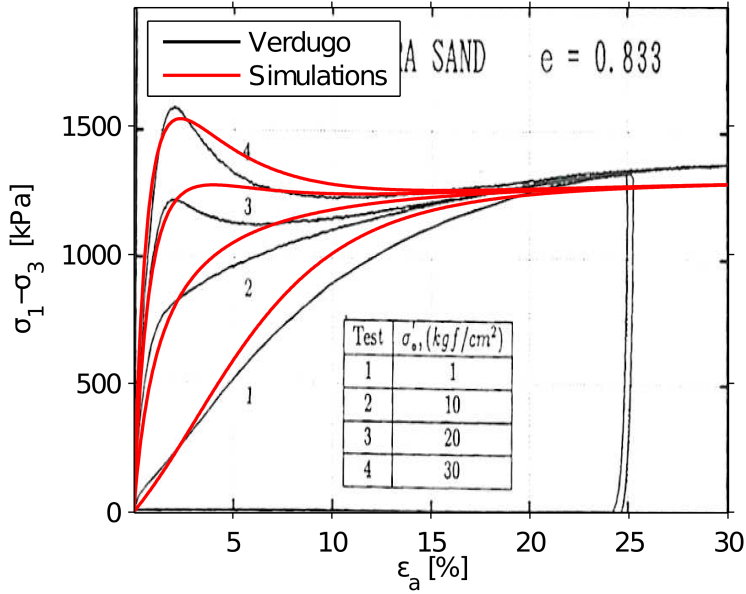


**Figure 5.41:** Stress-strain curves of undrained triaxial tests on sand with void ratio  $e = 0.833$  (Verdugo, 1992, Figure 4.10a).

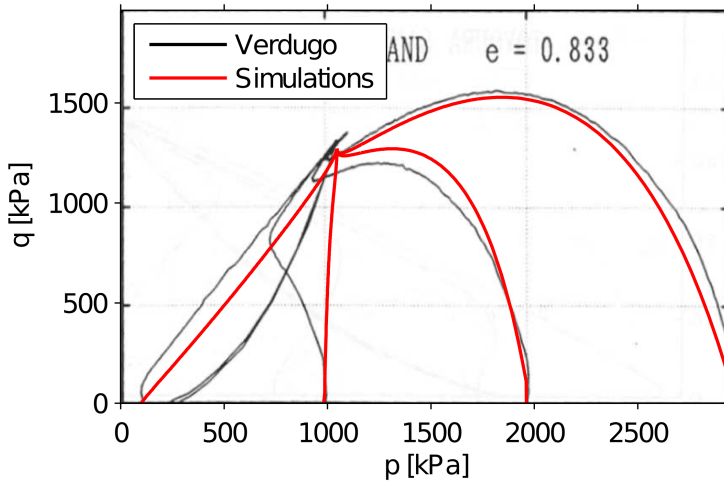


**Figure 5.42:** Effective stress paths of undrained triaxial test on sand with void ratio 0.833 (Verdugo, 1992, Figure 4.10b).



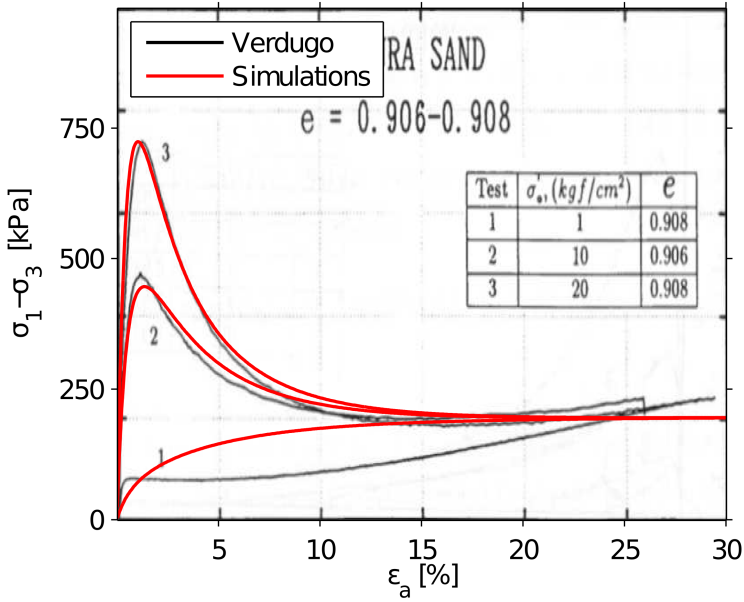


**Figure 5.43:** Stress-strain curves of undrained triaxial tests on sand with void ratio  $e = 0.906-0.908$  (Verdugo, 1992, Figure 4.9a) .

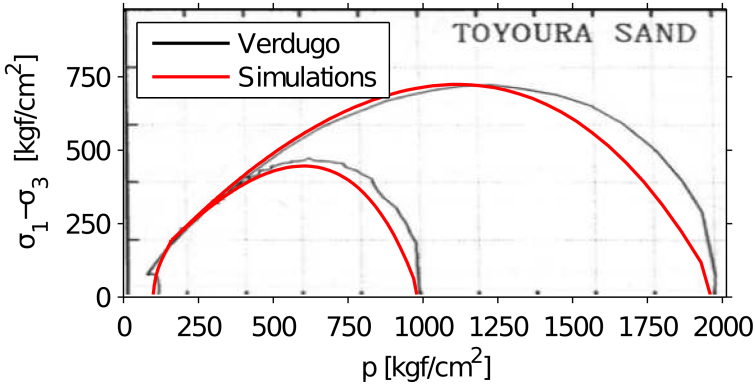


**Figure 5.44:** Effective stress paths of undrained triaxial test on sand with void ratio  $e = 0.906-0.908$  (Verdugo, 1992, Figure 4.9b) .



## Chapter 6

# Conclusions and Recommendations for Further Work

The results from the calculations are discussed and summarized in this chapter. A summary with the conclusions is given first. Results from testing are further analyzed. In light of this discussion, it is possible to consider the concept of modular programming. Recommendations for further work are given at the end of the chapter.

### 6.1 Summary and Conclusions

The Drucker–Prager model was implemented by the use of modular programming. First, a linear elastic-perfect plastic model was implemented, thus fulfilling the first objective. Triaxial test simulations gave perfect match between the implemented model and the standard Mohr–Coulomb model. The Drucker–Prager model is thus shown to perfectly represent the Mohr–Coulomb criterion in triaxial conditions. In plane strain tests, the Drucker–Prager model exhibit an initial yield with a subsequent slide along the yield surface. The effective stress path aims for the point where the strength and plastic flow direction coincide with the Mohr–Coulomb model. The behavior of the Drucker–Prager is a little softer close to failure in plane strain, resulting in larger pre-failure deformations.

To test the model further, load application and safety calculations are performed for a rigid, weightless foundation with even distributed load. Calculations gives greater deformations from loading for the Drucker–Prager model

than for the Mohr–Coulomb model. This is due to the softer pre-failure behavior for material points close to the foundation. The safety calculations give the same factor of safety for the two model, as expected due to the models giving equal strength.

Two dilatancy formulations were implemented. Both formulations gave curved potential functions  $Q$ , but the first gave turning point in approximately  $0.5p_{ref}$ , resulting in unintended behavior. The latter formulation performed as intended and the reference mean stress was reached in the critical state.

Finally, concepts originating from Been and Jefferies (1985) state parameter were applied in a reversed way, connecting the reference stress to the void ratio parameters. Stress dependent stiffness was included at last. Together with the inclusion of strain hardening and stress dependent dilatancy, the second objective is fulfilled.

Undrained tests on Toyoura sand by Verdugo (1992) were simulated for both constant and stress dependent stiffness. In both cases, important aspects of undrained behavior of sand are captured, yet the stress dependent stiffness version is superior in correctly simulating the tests. The simulations are a very good representation of the real tests for strain levels up to 2–3% and above 10%.

During the development of the model, continuous testing has been executed, meeting the last objective. The concept of modular programming by Rønningsen (2014) has shown to perform well. After establishing the first framework with material dependent and independent routines, the inclusion of new features, or even changing constitutive model, is a manageable and quite straightforward task. The concept yields a good tool for implementing and developing constitutive models of soils. A refinement of the numerical methods should be considered to ensure converging solutions for all combinations of stress states and strain increments.

## 6.2 Linear Elastic-Perfect Plastic Model

The simple concept of a linear elastic-perfect model makes it attractive for first implementation with subsequent testing of the performance.

### 6.2.1 Associated Flow in Single Material Point

Associated flow represent the simplest variant of the linear elastic-perfect plastic soil model.

**Triaxial conditions** As can be seen from the Figures 5.1-5.4, the implemented Drucker–Prager model simulates the exact same behavior for the tested sets of material parameters and initial conditions, as the standard Mohr–Coulomb model in PLAXIS. There is a perfect match between the models with respect to both stiffness and strength. This may be seen from the stress paths and pre-failure stress-strain plots in the figures. Further, a representative ESP is plotted in normalized  $\Pi$ -plane in Figure 5.9. In addition to the ESP, the Mohr–Coulomb and the Drucker–Prager surfaces for the triaxial compression and extension states are plotted. This clearly shows that up to failure, the paths coincide and behaves as expected, following a Lode angle of  $\theta = 0^\circ$  for triaxial compression and  $\theta = 60^\circ$  for triaxial extension.

The direction of the plastic flow may also be shown to coincide. This may be seen from the post-failure volumetric strains, by comparing theoretical solution from equation (2.74) and inclination of the strain curve in Figures 5.1. The inclination is equal to the theoretical solution for a drained triaxial compression test, that for a dilation angle  $\psi = \phi = 30^\circ$  is:

$$\frac{d\varepsilon_V^p}{d\varepsilon_1^p} = \frac{2 \sin 30^\circ}{1 - \sin 30^\circ} = 2 \quad (6.1)$$

This adds up to that the Drucker–Prager model gives a perfect fit with the Mohr–Coulomb model in triaxial conditions when the proper  $\alpha$ -coefficient are used. There are no results from the performed calculations that give reasons to doubt that the implemented model behaves correctly, as it coincides with the well-tested Mohr–Coulomb model.

**Plane strain conditions** Figures 5.5-5.8 showing the behavior of plane strain tests, demonstrate some differences between the two models. While triaxial tests are simulated with a perfect fit, the stress-strain curve and the ESP of the Drucker–Prager model bends off at an initial yield point A, seen in Figures 5.7 and 5.10. The Drucker–Prager model exhibit a softer behavior from point A up to the failure point F. On the contrary, the Mohr–Coulomb model exhibit constant stiffness as expected of a linear elastic-perfect plastic model.

Reasons for the behavior are as follows. The plastic strain increment is

given by the yield surface due to associated flow. Thus:

$$d\boldsymbol{\varepsilon}^p = d\lambda \begin{bmatrix} \frac{\partial F}{\partial \sigma_1} \\ \frac{\partial F}{\partial \sigma_2} \\ \frac{\partial F}{\partial \sigma_3} \end{bmatrix} = d\lambda \begin{bmatrix} \frac{s_1}{2\sqrt{J_2}} - \alpha \\ \frac{s_2}{2\sqrt{J_2}} - \alpha \\ \frac{s_3}{2\sqrt{J_2}} - \alpha \end{bmatrix} \quad (6.2)$$

The  $\alpha$ -coefficient of the Drucker–Prager criterion is earlier correlated in equation (2.84), such that for plane strain it is:

$$\alpha = \frac{s_{22}}{2\sqrt{J_2}} \quad (6.3)$$

For the simulated stress situation, see section 4.1.1 for description of details, the cartesian planes coincides with the principal stress planes due to no shear stresses. In the equation above,  $s_{22}$  is hence simply  $s_2$ . As a consequence of this, the plastic strain vector from equation (6.2) cannot have any component in  $\sigma_2$ -direction at failure. It is seen from the deviatoric plane plots in Figures 5.10-5.12 that for the Drucker–Prager model at failure, the ESP reaches one of the only two points on the yield surface that is normal to the  $\sigma_2$ -axis. The failure point is where the Mohr–Coulomb surface is tangent to Drucker–Prager surface. The strength of the models is thus equal. This sliding along the yield surface out of the hydrostatic plane is the reason for the softer pre-failure behavior.

The latter part of the volumetric strain curves for the models are parallel. This shows that the direction of the plastic flow for the two models coincide. Table 5.1 show the stress state at point F in Figures 5.7 and 5.10, and the  $\alpha$ -coefficient for the material. The stress state confirms that the plastic strain vector at point F for the Drucker–Prager model is parallel to the plastic strain vector at failure for the Mohr–Coulomb model:

$$d\boldsymbol{\varepsilon}_{\text{DP}}^p = d\lambda \frac{\partial F}{\partial \boldsymbol{\sigma}} = d\lambda \begin{bmatrix} 0.24 \\ 0.00 \\ -0.72 \end{bmatrix} \implies \boldsymbol{\varepsilon}_{\text{DP}}^p \parallel \boldsymbol{\varepsilon}_{\text{MC}}^p \quad (6.4)$$

$$d\boldsymbol{\varepsilon}_{\text{MC}}^p = d\lambda \frac{\partial F}{\partial \boldsymbol{\sigma}} = d\lambda \begin{bmatrix} 1 \\ 0 \\ -3 \end{bmatrix}$$

### 6.2.2 Non-Associated Flow in Single Material Point

Also the test simulations with non-associated flow gives perfect fit between the models for the triaxial conditions. As expected, no plastic volumetric strains arise. Plane strain tests are not simulated, due to complicated stress paths as a result of non-associated flow and plane strain requirements.

### 6.2.3 Loading and Safety Calculations

When performing loading and safety calculations, a major number of different combinations of strain increments and stress states are calculated. The robustness of the model is then challenged.

**Load application** Results from the loading phases show that for the parameter sets calculated, the Drucker–Prager model gives vertical deformations of the foundation that are between 5% and 27% greater than for the Mohr–Coulomb model. Even though the deformations themselves are of small order, the difference between the models is considerable.

The differences likely occur due to softer behavior close to failure for plane strain situations, as discussed above. The region close to the foundation is subjected to a stress increase that causes yielding and eventually failure in some points. As the Drucker–Prager model is shown to give softer response close to failure, greater strains develop at these yielding points before the full strength is mobilized. This is supported by the load-deformation curves in Figure 5.15-5.16. The Drucker–Prager curves bend off moderately for the latter load increments, which would be the increments driving the material points above the yield limit into plastic deformations.

For the friction angle  $\phi = 20^\circ$ , the difference between the models is greater than for the friction angle  $\phi = 30^\circ$ . This supports the argument above, as a lower friction angle should result in a bigger region being affected by the load application. Thus, the soil volume is driven to larger plastic strains resulting in larger deformations.

**Safety calculations** As opposed to the load application, the safety calculations do not reveal significant differences between the models. In fact, differences in the factor of safety are in the order of 1% and can be regarded as negligible. These differences are within the continuous adjustment of the factor of safety at failure. As the strength of the Drucker–Prager model is correlated to the Mohr–Coulomb model, the ultimate strength at large strains should be equal for the models. The strength of the material is reduced in accordance to

equation (3.9). This gives a reduced friction angle  $\phi_{reduced}$  with corresponding reduced strength. As the correlation of the  $\alpha$ -coefficient is set to give equal strengths, they coincide for all friction angles. The failure surfaces shown by shadings of incremental shear strain in Figures 5.19-5.22 demonstrate that the failure mechanisms found should be regarded as the same.

It should be noted that a tremendously higher number of steps with few iterations is necessary for the Drucker–Prager model to give the factor of safety resulting in the failure state. PLAXIS models, like the Mohr–Coulomb, should be expected to perform computationally better and faster compared to a user defined soil model, as the latter has not been tested and refined for years. The results give reason to believe that the implemented model behaves reliable and is stable for calculations for load application and factor of safety.

## 6.3 Strain Hardening and Stress Dependent Dilatancy

Strain hardening and stress dependent dilatancy represent important improvements of the model’s ability to simulate soil behavior.

### 6.3.1 Strain Hardening and Stress Dependent Dilation Angle

The results for the two different dilatancy formulations presented generally show the same behavior, with one important exception of the ultimate mean stress level. General comments of the behavior for both formulations are presented in section 6.3.2, while only the ultimate mean stress level is considered here.

**Ultimate mean stress level** It is evident from Figure 5.27 that the ultimate mean stress  $p_f$  for undrained tests is not to the reference stress  $p_{ref}$ , as was intended. The dilatancy formulation of equation (3.17), giving a dilation angle  $\psi = 0^\circ$  at the reference stress, was expected to give a vertical effective stress path such that  $dp = 0$ . However, the ultimate mean stress is seen from Table 5.3, reproduced as  $p_{f,PLAXIS}$  in Table 6.1, to be approximately  $0.5p_{ref}$ . Reasons for this behavior are discussed in the following.

When the material reaches the ultimate mean stress, the material has reached some kind of critical state or steady state. Applying the condition of no volumetric strains for an undrained state and no mean stress change at



the critical state, the following requirement is obtained:

$$d\varepsilon_V = d\varepsilon_V^e + d\varepsilon_V^p = \frac{dp}{K} + d\lambda \frac{\partial Q}{\partial p} = 0 \implies \frac{\partial Q}{\partial p} = 0 \quad (6.5)$$

Using the  $\alpha$ -expression of triaxial compression from Table 2.1 to introduce the dilatancy formulation, yields the plastic potential function  $Q$ :

$$\begin{aligned} Q &= \sqrt{J_2} - \alpha_Q I_1 - C = \sqrt{J_2} - \frac{2 \sin \psi}{\sqrt{3}(3 - \sin \psi)} I_1 - C \\ &= \frac{q}{\sqrt{3}} - \frac{2\sqrt{3} \sin \psi_0 (p_{ref} p - p^2)}{(3 - \sin \psi_0) p_{ref} + p \sin \psi_0} - C = 0 \end{aligned} \quad (6.6)$$

Now, the plastic potential function may be differentiated with respect to the mean stress  $p$ . As the requirement of equation (6.5) must be fulfilled by the numerator, only this is calculated:

$$\begin{aligned} &2\sqrt{3} \sin \psi_0 (p_{ref} - 2p) ((3 - \sin \psi_0) p_{ref} + p \sin \psi_0) \\ &\quad - 2\sqrt{3} \sin \psi_0 (p_{ref} p - p^2) \sin \psi_0 = 0 \\ \implies &-\sin \psi_0 p^2 + (2 \sin \psi_0 - 6) p_{ref} p + (3 - \sin \psi_0) p_{ref}^2 = 0 \end{aligned} \quad (6.7)$$

Finally, solving the quadratic equation for the unknown reference mean stress  $p = p_f$  yields two solutions, of which only one has a physical relevance:

$$p_f = p = \frac{\sin \psi_0 - 3 + \sqrt{3(3 - \sin \psi_0)}}{\sin \psi_0} p_{ref} \approx 0.5 p_{ref} \quad (6.8)$$

The results from the PLAXIS calculations and the analytic solutions of the ultimate mean stress level from equation (6.8) are shown in Table 6.1.

**Table 6.1:** Mean stress at failure for different reference mean stress levels and input dilation angles.

$\mathbf{p}_{ref}$ [kPa]	$\psi_0$ [°]	$\mathbf{p}_{f,PLAXIS}$ [kPa]	$\mathbf{p}_{f,ANALYTIC}$ [kPa]
50	5	24.82	24.82
	10	24.63	24.63
100	5	49.71	49.63
	10	49.25	49.25
200	5	99.31	99.26
	10	98.51	98.51

The dilatancy formulation from equation (3.17) fails to simulate the intended behavior. The small discrepancies between the PLAXIS calculations and analytical solution in Table 6.1 for dilation angle  $\psi_0 = 5^\circ$ , are most likely a result lower dilation angle causing a slower strive towards the ultimate mean stress level. For any practical application they represent the same mean stress level.

This dilatancy formulation demonstrate the importance of keeping track of dependent and independent variables. The idea of the formulation was to use the mean stress level to describe the state of the material relative to the reference mean stress. However, this caused the plastic potential function to be a curved surface with its turning point at the mean stress level given by equation (6.8), as may be seen in Figure 5.27. Introducing the mean stress dependency of the dilation angle causes the current mean stress level to predict the change in itself. This is not an uncommon practice and is actually the aim of the idea, yet caution must be paid in order to obtain constitutive models that perform as intended.

Further, the formulation has one more drawback. Due to the current dilatancy entering the calculation of the  $\alpha_Q$ -coefficient in both numerator and denominator, change in mean stress level causes a non-linear approach of the dilatancy coefficient. This may or may not represent a good physical representation of the material behavior, but the effects of a change is hard for the user to predict and validate. A simpler approach or an approach based on behavior from laboratory results would both be preferred.

### 6.3.2 Strain Hardening and Stress Dependent Dilation Coefficient

Except for the ultimate mean stress level, the principal behavior of the two formulations were the same.

**Ultimate mean stress level** The stress dependent dilation coefficient  $\alpha_Q$  was set to fulfill the requirements presented in section 3.5.2. Hence, the problem of reaching another mean stress level than intended is avoided. Figure 5.31 shows that the material tries to reach the reference mean stress for large strains, and corresponding deviatoric stress is shown in Figure 5.32. The dilatative behavior performs as intended.

**General behavior** Figures 5.28-5.30 yield no reasons for concern regarding the performance of the model. Even Figures 5.23-5.26 for the discarded dilatancy formulation show satisfying behavior, except for the ultimate mean stress

level. The initial part of the Mohr–Coulomb and the implemented Drucker–Prager model generally coincide, which must be regarded as satisfying. The volumetric strains are small, as expected for undrained simulations. Further, the development of the volumetric strain change slowly approaches zero. This is in accordance with the dilatancy formulation.

One issue with the model is that the ESP bends off too little, in spite of an input dilation angle of  $\psi_0 = 10^\circ$ . The development of plastic strains is governed by the initial value of the plastic stiffness,  $H_0$ . Interaction between  $\psi_0$  and  $H_0$  have not been investigated, yet there should be expected that other choices of initial stiffness gives another dilative and contractive response. The choice of a stiffness  $H_0 = 1000$  may be an unrealistic value, and a comparison to laboratory tests should be done for further validation of the model.

The model behaves as intended, even though further investigation of its performance should be carried out. A proper calibration of the plastic stiffness according to the procedure described in section 2.6.4, is of special interest to see how the model behaves for realistic values of  $H_0$ .

## 6.4 Void Ratio Dependent Dilatancy

By introducing the void ratio relations to the reference mean stress level, the concept of the model is improved.

### 6.4.1 Simulation of Toyoura Sand with Constant Elastic Stiffness

Constant elastic stiffness is simpler and does not violate thermodynamic laws, yet it lacks an important effect of soil behavior.

**General behavior** Generally, the model is capable of simulating important aspects of the behavior of the undrained triaxial tests by Verdugo (1992) on Toyoura sand well. Effects like softening is captured surprisingly well, with relative few and simple elements from constitutive soil modeling. By introducing the void ratio-parameters, variables that may be more familiar to practicing engineers are used. Even though the overall performance of the model is good, it is seen from Figures 5.33-5.38 that trade-offs must be made in matching the paths. In general, the behavior is captured, but discrepancies remain.

**Ultimate strength** The ultimate mean strength is determined by the friction angle, attraction, initial void ratio and the critical state line in the  $e$ - $\log p$ -plot. For undrained situations the void ratio is always the initial void ratio

and defines if dilation or contraction occur. The material will seek towards the mean stress level that is critical for the initial void ratio, and this mean stress defines the available strength.

As a consequence of this, which relation chosen to represent the  $e$ - $\log p$ -relation is vital for defining the strength. The assumption of a linear relation is a crude assumption for the Toyoura sand, as may be seen from Figure 4.3. A bilinear or curved relation would be more suited, yet it require the user to define more parameters. The stress range of the tests are quite wide, and for a building project the stresses range are likely far smaller and the linear relation may be a better fit.

**Challenges with constant parameters** Even though capturing important aspects of the behavior well, the model simulates a quite different stress-strain curve for sand consolidated to lower pressure in Figure 5.33. The choice of using constant parameters makes it hard to obtain a good fit for all simulations. A constant elastic stiffness represents another crude assumption causing great differences between the real stress-strain behavior and the tests. Further, other stress dependencies may exist and the parameters used should hence be regarded as a curve adaption for best fit, rather than strict physical parameters.

**Dilatancy behavior** The dilatancy formulation simulates real soil behavior quite well. However, the effect of contracting behavior for low mobilization, even for mean stress levels below the reference stress, is not caught. This is seen from the  $p$ - $q$ -plots in Figures 5.40, 5.42 and 5.44. An inclusion of this effect would give an even better representation of reality.

#### 6.4.2 Simulation of Toyoura Sand with Mean Stress Dependent Stiffness

The introduction of stress dependent stiffness causes a more realistic behavior. However, problems with violation of thermodynamic laws arise for cyclic loads or un-/reloading loops. For triaxial compression tests the loading is monotonic, thus the problems are avoided and improve the simulations.

**General behavior** By including the stress dependent stiffness, the model performs even better, seen from Figures 5.39-5.44. This appears to give a major improvement for initial void ratio  $e = 0.735$ , yet improvement is seen for all densities. Up to strain levels of 2–3%, which is most relevant for building purposes, the representation is very good. Above strain levels of approximately 10% the simulations are also performing well. The main differences between

the real tests and the simulations occur at strain levels between 2–3% up to 10%.

A likely reason for the discrepancy is the lack of a contracting effect for low mobilizations, as discussed above. For these strain levels the difference between real and simulated mean stress levels are greatest. This also implies that the soil should not gain the increased stiffness due to increased mean stress as fast as the model simulates. A softer behavior for medium strain ranges would give a more appropriate simulation. The differences are still of small order and the model simulates the Toyoura sand well.

## 6.5 Implemented Routines

This thesis has shown that the concept of modular programming as proposed by Rønningen (2014) has been implemented and performs well. Discrepancies discussed in sections above are due to the formulation of constitutive model. Some challenges with the numerical methods was encountered and should be considered refined.

### 6.5.1 Modular programming

The concept of modular programming allows for continuous development of the model. This makes it easier to consecutively add features and refine the model. During implementation and development of the Drucker–Prager model presented, this is proved to be a good approach that allows for testing and validation of each feature when added.

The discussion above illustrate that drawbacks and lacks in simulations are explained by the limitations in the formulations of the model. Using modular programming is an advantage, as improvements regarding the mentioned limitations may be implemented quite easily. This allows the developer to focus on improving the constitutive model and its behavior, rather than the programming and implementation in itself. The operations done by the MATLAB script greatly reduces the work necessary to add features. Once the framework is established for a model, further development is a quite straightforward exercise.

### 6.5.2 Numerical methods

For some strain increments the Newton–Raphson iteration failed to converge due to oscillation between two points. For a one-dimensional problem such os-

cillation occur for the following situation. Starting at the first point  $(x_1, f(x_1))$ , the root of the tangent function defines the next point of the iteration in  $(x_2, 0)$ . If the tangent of this next point  $(x_2, f(x_2))$  has its root in  $(x_1, 0)$ , this causes oscillation as these two points,  $x_1$  and  $x_2$ , give each other as solutions. The same phenomena have been seen during calculations for some unfavorable combinations of strain increments and stress levels for the seven-dimensional problem.

The convergence problem was solved by recursion, thus the Newton–Raphson iteration calls upon itself for a smaller increment when the iteration counter exceeds a predefined limit. A more sound and stable solution to the convergence problem may be successive overrelaxation (SOR), that may ensure convergence to cases where the implemented Newton–Raphson iteration fails (Kreyszig, 2006). SOR introduces an overrelaxation factor  $\omega$  by some mathematical manipulation. Different choices of  $\omega$  may give faster convergence or ensure convergence for diverging or oscillating iterations.

## 6.6 Recommendations for Further Work

The Mohr–Coulomb model give different strength limits for triaxial compression and extension, thus a Lode angle dependency exist. The implemented Drucker–Prager strength criterion does not depend on the Lode angle, giving the same strength for all stress situations. To obtain correlation to the Mohr–Coulomb model, the user needs to define what  $\alpha$ -coefficient to use. A Lode angle dependency should be included to better simulate the strength of the soil. A failure surface that includes a Lode angle dependency, but is smooth, would be an improvement of the model. Such surfaces has been proposed and may be found in literature.

Mobilization dependency of the dilatancy formulation would improve the ability to simulate behavior of soil, giving more reliable load-displacement curves. Further, the numerical scheme should be improved. Even though the recursion loop has improved the stability of the Newton–Raphson iteration, a more sound method that is unconditionally stable should be implemented. FEM-calculations require all iterations to succeed, and even one failed iteration of thousands breaks the FEM-routine.

Simulations of Toyoura sand has given promising results of the capability of modeling undrained behavior of sands. However, only a few of the material parameters were given by Verdugo (1992). Most of them were optimized to give a best fit. An interpretation of all parameters from laboratory tests with

subsequent simulations using the model would be of great interest in order to see how it behaves when parameters are not optimized. If it is possible to use parameters from laboratory tests to predict the behavior of sand in other stress situations, the predictive capacity of model is good. If not, any application to practical problems is harder, if possible at all. More tests over both narrow and wider stress range would be of interest.

A comparison between the implemented model and other models that are capable of simulating similar behavior, for instance the Severn Trent model described in section 2.7.2, should give findings that may improve the model. The state parameter by Been and Jefferies (1985) give a sound approach to the critical state and could be included better. This would improve the theoretical basis for the implemented model.

## Bibliography

- Been, K. and Jefferies, M. G. (1985), 'A state parameter for sands', Géotechnique **35**(2), 99–112(13).
- Cook, R., Malkus, D., Plesha, M. and Witt, R. (2002), Concepts and applications of finite element analysis, fourth edn, Wiley, New York.
- Drucker, D. C. and Prager, W. (1952), 'Soil mechanics and plastic analysis or limit design', Quarterly of applied mathematics **10**(2), 157–165.
- Gajo, A. and Muir Wood, D. (1999a ), 'A kinematic hardening constitutive model for sands: the multiaxial formulation', International Journal for Numerical and Analytical Methods in Geomechanics **23**(9), 925–965.
- Gajo, A. and Muir Wood, D. (1999b ), 'Severn–trent sand: a kinematic-hardening constitutive model: the q–p formulation', Géotechnique **49**(5), 595–614.
- Godunov, A. L. (2009), 'Fortran code. Gaussian elimination with scaling and pivoting (Gauss\_2.f90). [Computer program]. Department of Physics, Old Dominion University, Norfolk, VA. Available at: <http://ww2.odu.edu/~godunov/>. [Accessed 24 february 2014]'.
- Hopperstad, O. and Børvik, T. (2013), Lecture Notes, TKT4135 Material Mechanics, Part 1, Insitutt for konstruksjonsteknikk, NTNU.
- Kreyszig, E. (2006), Advanced engineering mathematics, number 9th ed., Wiley, Hoboken, N.J.
- Muir Wood, D. (1990), Soil Behaviour and Critical State Soil Mechanics, Cambridge University Press, Cambridge.
- Muir Wood, D., Belkheir, K. and Liu, D. F. (1994), 'Strain softening and state parameter for sand modelling', Geotechnique **44**(2), 335–339.
- Nordal, S. (2012a), Lecture Notes, BA8304 Soil Modelling, Insitutt for bygg, anlegg og transport, NTNU.
- Nordal, S. (2012b), TBA4116 Geotechnical Engineering Advanced Course, Lecture notes and background material, Insitutt for bygg, anlegg og transport, NTNU.



PLAXIS (2012a), PLAXIS 2D. Material Models Manual., Plaxis bv.

PLAXIS (2012b), PLAXIS 2D. Reference Manual., Plaxis bv.

Rønningen, J. A. (2014), Personal correpondance.

Tadesse, S. and Nordal, S. (2002), Simulating sand behaviour using a state parameter model, in 'NUMGE 2002: 5th European Conference Numerical Methods in Geotechnical Engineering : Paris, 4-6 September 2002', LCPC, Paris, pp. 163–168.

Verdugo, R. L. (1992), Characterization of sandy soil behavior under large deformation, PhD thesis, University of Tokyo.

# List of Figures

2.1	Principal stress space. . . . .	11
2.2	Decomposition of total strains into elastic and plastic strains. For simplicity perfect plasticity is illustrated. (Nordal, 2012b, Figure 6.1b) . . . . .	14
2.3	Sketch of a yield surface. (Hopperstad and Børvik, 2013, Figure 7-1) . . . . .	17
2.4	Mohr–Coulomb yield surfaces. . . . .	23
2.5	Sketch of a $\sigma_1$ - $\sigma_3$ -plot showing associated flow rule and non-associated flow rule connected to a plastic potential function where the dilation angle controls the flow. (Nordal, 2012b, Figure 6.3), (Nordal, 2012b, Figure 6.4) . . . . .	26
2.6	Drucker–Prager yield surface. . . . .	28
2.7	Yield surfaces of Drucker–Prager with the different $\alpha$ -coefficients, along with the Mohr–Coulomb yield surfaces. . . . .	32
2.8	Detailed view of the yield surfaces. . . . .	32
2.9	Sketch of accumulated plastic strains plotted against mobilized friction for a drained triaxial test. (Nordal, 2012a, Figure 6.21) . . . . .	34
2.10	Sketch of a possible mean stress dependent dilation formulation. . . . .	35
2.11	Illustration of the state parameter $\psi^*$ (Been and Jefferies, 1985, Figure 2). . . . .	37
2.12	Figure showing typical drained triaxial compression tests on sand for (1) dense sand at low stress level, (2) dense sand at medium stress level and (3) loose sand at low stress level (Muir Wood et al., 1994, Figure 1). . . . .	39
2.13	Two variants of the Newton–Raphson method for a non-linear function $f(x) = 0$ . . . . .	41
3.1	Elastic predictor-plastic corrector algorithm for a yield criterion with hardening, illustrated in a stress space. (Hopperstad and Børvik, 2013, Figure 7-18) . . . . .	48
3.2	The calculation process of the implemented model (Rønningen, 2014). . . . .	49

4.1	Geometry of foundation used in the safety calculation. . . . .	65
4.2	The mesh used in the calculation. . . . .	66
4.3	Void ratio-mean stress critical state line for Toyoura sand (Verdugo, 1992, Figure 4.17a) ). . . . .	69
5.1	Drained triaxial compression tests of Set 1-3. . . . .	73
5.2	Drained triaxial compression tests of Set 4. . . . .	73
5.3	Drained triaxial extension tests of Set 1-3. . . . .	74
5.4	Drained triaxial compression tests of Set 4. . . . .	74
5.5	Drained plane strain test of Set 1. . . . .	75
5.6	Drained plane strain test of Set 2. . . . .	75
5.7	Drained plane strain test of Set 3. . . . .	76
5.8	Drained plane strain test of Set 4. . . . .	76
5.9	Drained triaxial tests of Set 1 in normalized coordinates in deviatoric plane with the relevant yield surfaces. . . . .	77
5.10	Drained plane strain test of Set 3 in deviatoric plane. . . . .	77
5.11	Drained plane strain test of Set 1-3 in normalized coordinates in deviatoric plane. . . . .	78
5.12	Drained plane strain test of Set 4 in normalized coordinates in deviatoric plane. . . . .	78
5.13	Drained triaxial compression tests of Set 5. . . . .	80
5.14	Drained triaxial extension tests of Set 1-3. . . . .	80
5.15	Load-deformation curve for material parameter Set 8 ( $\phi = 30^\circ$ , $\psi = 2^\circ$ ). . . . .	82
5.16	Load-deformation curve for material parameter Set 9 ( $\phi = 30^\circ$ , $\psi = 30^\circ$ ). . . . .	82
5.17	Safety factor-deformation curve for parameter Set 8 ( $\phi = 30^\circ$ , $\psi = 2^\circ$ ). . . . .	83
5.18	Safety factor-deformation curve for parameter Set 9, with friction ( $\phi = 30^\circ$ , $\psi = 30^\circ$ ). . . . .	83
5.19	Shadings of incremental shear strains at failure for Mohr–Coulomb model with material parameter Set 8 ( $\phi = 30^\circ$ , $\psi = 2^\circ$ ). . . . .	84
5.20	Shadings of incremental shear strains at failure for Drucker–Prager model with material parameter Set 8 ( $\phi = 30^\circ$ , $\psi = 2^\circ$ ). . . . .	84
5.21	Shadings of incremental shear strains at failure for Mohr–Coulomb model with material parameter Set 9 ( $\phi = 30^\circ$ , $\psi = 30^\circ$ ). . . . .	85

5.22	Shadings of incremental shear strains at failure for Drucker-Prager model with material parameter Set 9 ( $\phi = 30^\circ$ , $\psi = 30^\circ$ ).	85
5.23	Undrained triaxial compression test consolidated to $\sigma_3 = 50\text{kPa}$ .	87
5.24	Undrained triaxial compression test consolidated to $\sigma_3 = 100\text{kPa}$ .	87
5.25	Undrained triaxial compression test consolidated to $\sigma_3 = 200\text{kPa}$ .	88
5.26	Undrained triaxial compression test consolidated to $\sigma_3 = 400\text{kPa}$ .	88
5.27	Effective stress paths for all undrained triaxial tests with mean stress and plastic potential function $Q$ at large strains. . . . .	89
5.28	Undrained triaxial compression test consolidated to $\sigma_3 = 100\text{kPa}$ .	90
5.29	Undrained triaxial compression test consolidated to $\sigma_3 = 200\text{kPa}$ .	91
5.30	Undrained triaxial compression test consolidated to $\sigma_3 = 400\text{kPa}$ .	91
5.31	Effective stress paths for all undrained triaxial tests with mean stress and plastic potential function $Q$ at large strains. . . . .	92
5.32	Stress-strain-plot for all undrained triaxial tests. . . . .	93
5.33	Stress-strain curves of undrained triaxial tests on sand with void ratio $e = 0.735$ (Verdugo, 1992, Figure 4.11a) ). . . . .	94
5.34	Effective stress paths of undrained triaxial test on sand with void ratio 0.735 (Verdugo, 1992, Figure 4.11b) ). . . . .	95
5.35	Stress-strain curves of undrained triaxial tests on sand with void ratio $e = 0.833$ (Verdugo, 1992, Figure 4.10a) ). . . . .	96
5.36	Effective stress paths of undrained triaxial test on sand with void ratio 0.833 (Verdugo, 1992, Figure 4.10b) ). . . . .	96
5.37	Stress-strain curves of undrained triaxial tests on sand with void ratio $e = 0.906\text{--}0.908$ (Verdugo, 1992, Figure 4.9a) ). . . . .	97
5.38	Effective stress paths of undrained triaxial test on sand with void ratio $e = 0.906\text{--}0.908$ (Verdugo, 1992, Figure 4.9b) ). . . . .	97
5.39	Stress-strain curves of undrained triaxial tests on sand with void ratio $e = 0.735$ (Verdugo, 1992, Figure 4.11a) ). . . . .	98
5.40	Effective stress paths of undrained triaxial test on sand with void ratio 0.735 (Verdugo, 1992, Figure 4.11b) ). . . . .	99
5.41	Stress-strain curves of undrained triaxial tests on sand with void ratio $e = 0.833$ (Verdugo, 1992, Figure 4.10a) ). . . . .	100
5.42	Effective stress paths of undrained triaxial test on sand with void ratio 0.833 (Verdugo, 1992, Figure 4.10b) ). . . . .	100
5.43	Stress-strain curves of undrained triaxial tests on sand with void ratio $e = 0.906\text{--}0.908$ (Verdugo, 1992, Figure 4.9a) ). . . . .	101

5.44	Effective stress paths of undrained triaxial test on sand with void ratio $e = 0.906\text{--}0.908$ (Verdugo, 1992, Figure 4.9b) . . . .	101
E.1	Load-deformation curve for material parameter Set 6 ( $\phi = 30^\circ$ , $\psi = 0^\circ$ ). . . . .	159
E.2	Load-deformation curve for material parameter Set 7 ( $\phi = 30^\circ$ , $\psi = 1^\circ$ ). . . . .	160
E.3	Load-deformation curve for material parameter Set 8 ( $\phi = 30^\circ$ , $\psi = 2^\circ$ ). . . . .	160
E.4	Load-deformation curve for material parameter Set 9 ( $\phi = 30^\circ$ , $\psi = 30^\circ$ ). . . . .	161
E.5	Load-deformation curve for material parameter Set 10 ( $\phi = 20^\circ$ , $\psi = 0^\circ$ ). . . . .	161
E.6	Load-deformation curve for material parameter Set 11 ( $\phi = 20^\circ$ , $\psi = 20^\circ$ ). . . . .	162
E.7	Safety factor-deformation curve for material parameter Set 6 ( $\phi = 30^\circ$ , $\psi = 0^\circ$ ). . . . .	163
E.8	Safety factor-deformation curve for material parameter Set 7, with friction ( $\phi = 30^\circ$ , $\psi = 1^\circ$ ). . . . .	164
E.9	Safety factor-deformation curve for material parameter Set 8 ( $\phi = 30^\circ$ , $\psi = 2^\circ$ ). . . . .	164
E.10	Safety factor-deformation curve for material parameter Set 9, with friction ( $\phi = 30^\circ$ , $\psi = 30^\circ$ ). . . . .	165
E.11	Safety factor-deformation curve for material parameter Set 6 ( $\phi = 20^\circ$ , $\psi = 0^\circ$ ). . . . .	165
E.12	Safety factor-deformation curve for material parameter Set 9, with friction ( $\phi = 20^\circ$ , $\psi = 20^\circ$ ). . . . .	166
E.13	Shadings of incremental shear strains at failure for Mohr–Coulomb model with material parameter Set 6 ( $\phi = 30^\circ$ , $\psi = 0^\circ$ ). . . . .	167
E.14	Shadings of incremental shear strains at failure for Drucker–Prager model with material parameter Set 6 ( $\phi = 30^\circ$ , $\psi = 0^\circ$ ). . . . .	167
E.15	Shadings of incremental shear strains at failure for Mohr–Coulomb model with material parameter Set 7 ( $\phi = 30^\circ$ , $\psi = 1^\circ$ ). . . . .	168
E.16	Shadings of incremental shear strains at failure for Drucker–Prager model with material parameter Set 7 ( $\phi = 30^\circ$ , $\psi = 1^\circ$ ). . . . .	168
E.17	Shadings of incremental shear strains at failure for Mohr–Coulomb model with material parameter Set 8 ( $\phi = 30^\circ$ , $\psi = 2^\circ$ ). . . . .	169

---

E.18	Shadings of incremental shear strains at failure for Drucker–Prager model with material parameter Set 8 ( $\phi = 30^\circ$ , $\psi = 2^\circ$ ).	169
E.19	Shadings of incremental shear strains at failure for Mohr–Coulomb model with material parameter Set 9 ( $\phi = 30^\circ$ , $\psi = 30^\circ$ ).	. . . 170
E.20	Shadings of incremental shear strains at failure for Drucker–Prager model with material parameter Set 9 ( $\phi = 30^\circ$ , $\psi = 30^\circ$ ).	170
E.21	Shadings of incremental shear strains at failure for Mohr–Coulomb model with material parameter Set 10 ( $\phi = 20^\circ$ , $\psi = 0^\circ$ ).	. . . 171
E.22	Shadings of incremental shear strains at failure for Drucker–Prager model with material parameter Set 10 ( $\phi = 20^\circ$ , $\psi = 0^\circ$ ).	171
E.23	Shadings of incremental shear strains at failure for Mohr–Coulomb model with material parameter Set 11 ( $\phi = 20^\circ$ , $\psi = 20^\circ$ ).	. . . 172
E.24	Shadings of incremental shear strains at failure for Drucker–Prager model with material parameter Set 11 ( $\phi = 20^\circ$ , $\psi = 20^\circ$ ).	172

# List of Tables

2.1	Coefficients of the Drucker–Prager criterion matching the Mohr–Coulomb-model for different stress states. . . . .	31
4.1	Parameter sets for validation of linear elastic-perfect plastic model with associated flow. . . . .	64
4.2	Parameter set for validation of linear elastic-perfect plastic model with non-associated flow. . . . .	64
4.3	Material parameters used in safety calculations. . . . .	65
4.4	Characteristic mesh data for the model. . . . .	66
4.5	Coordinates of selected points. . . . .	66
4.6	Numerical control parameters for phases used in the calculation. Non-default values in italic. . . . .	67
4.7	Parameter set for validation of the strain hardening and stress dependent dilation coefficient model. . . . .	68
4.8	Material parameters for the triaxial tests on Toyoura sand with constant elastic stiffness. . . . .	70
4.9	Material parameters for the triaxial tests on Toyoura sand with stress dependent elastic stiffness. . . . .	70
5.1	Stress state at failure point F for the drained plane strain test of Set 3. . . . .	72
5.2	Summary of results from loading and safety calculations. . . . .	81
5.3	Failure mean stress for some reference stresses and dilation angles. . . . .	89
6.1	Mean stress at failure for different reference mean stress levels and input dilation angles. . . . .	109

# List of Symbols and Abbreviations

## Latin letters:

$A$	Area	$I_3$	Third full stress invariant
$A$	Plastic resistance number	$I_1^\varepsilon$	First full strain invariant
$A$	Severn Trent constant	$I_2^\varepsilon$	Second full strain invariant
$a$	Attraction	$I_3^\varepsilon$	Third full strain invariant
<b>B</b>	Deformation matrix	<b>J</b>	Jacobi matrix
$B$	Severn Trent constant	$J_1$	First deviatoric stress invariant
$b$	Stress ratio	$J_2$	Second deviatoric stress invariant
$C$	Drucker–Prager dilation coefficient	$J_3$	Third deviatoric stress invariant
$c$	Cohesion	$J_1^\varepsilon$	First deviatoric strain invariant
<b>D</b>	Constitutive matrix	$J_2^\varepsilon$	Second deviatoric strain invariant
$D_{ep}$	Elastic-plastic constitutive matrix	$J_3^\varepsilon$	Third deviatoric strain invariant
$D_{ijkl}$	Constitutive matrix	$K$	Bulk modulus
$E$	Young’s modulus	$K_w$	Water bulk modulus
$E_u$	Undrained Young’s modulus	$K_0$	Stress ratio
$E'$	Drained Young’s modulus	$K'$	Drained bulk modulus
$e$	Deviatoric strain vector	<b>k</b>	Element stiffness matrix
$e_{ij}$	Deviatoric strain vector	$k$	Drucker–Prager coefficient
$e$	Void ratio	$k$	Severn Trent constant
$e_{ss}$	Reference void ratio	$M$	Mohr–Coulomb inclination
$e_\lambda$	Reference void ratio	$M_{cr}$	Critical state stress ratio
$e_0$	Initial void ratio	$M_p$	Available peak stress ratio
$F$	Yield surface	$m$	Stress exponent
$G$	Shear modulus	<b>N</b>	Shape functions
$G^*$	Reference shear stiffness	$N_f$	Mohr–Coulomb inclination
$H_0$	Initial plastic stiffness		
<b>I</b>	Identity matrix		
$I_1$	First full stress invariant		
$I_2$	Second full stress invariant		





$\gamma_{oct}$	Octahedral shear strain	$\lambda$	Plastic parameter
$\delta$	Differentiation operator	$\lambda^*$	Inclination of critical state line
$\delta_{ij}$	Kronecker delta	$\mu$	Bulk ratio
$\varepsilon$	Strain vector	$\nu$	Poisson's ratio
$\varepsilon^e$	Elastic strain vector	$\nu_u$	Undrained Poisson's ratio
$\varepsilon^p$	Plastic strain vector	$\nu'$	Drained Poisson's ratio
$\varepsilon_n$	Previous strain vector	$\xi$	Mean stress coordinate
$\varepsilon_{n+1}$	Next strain vector	$\rho$	Deviatoric coordinate
$\varepsilon_{ij}$	Strain vector	$\rho$	Mobilized friction angle
$\varepsilon$	Strain	$\Sigma M_s f$	Factor of safety
$\varepsilon^e$	Elastic strain scalar	$\sigma$	Stress vector
$\varepsilon^p$	Plastic strain scalar	$\sigma'$	Effective stress vector
$\varepsilon_V$	Volumetric strain	$\sigma_n$	Previous stress vector
$\varepsilon_{11}$	Normal strain on $x_1$ -surface	$\sigma_{n+1}$	Next stress vector
$\varepsilon_{22}$	Normal strain on $x_2$ -surface	$\sigma_{n+1}^{tr}$	Trial stress vector
$\varepsilon_{33}$	Normal strain on $x_3$ -surface	$\sigma_w$	Pore pressure vector
$\varepsilon_{12}$	Shear strain on $x_1$ - and $x_2$ -surfaces	$\sigma_{ij}$	Stress vector
$\varepsilon_{23}$	Shear strain on $x_2$ - and $x_3$ -surfaces	$\dot{\sigma}_{ij}$	Stress rate vector
$\varepsilon_{31}$	Shear strain on $x_3$ - and $x_1$ -surfaces	$\sigma'_{ij}$	Effective stress vector
$\varepsilon_1$	First/greatest principal strain	$\dot{\sigma}'_{ij}$	Effective stress rate vector
$\varepsilon_2$	Second/intermediate principal strain	$\sigma$	Stress
$\varepsilon_3$	Third/smallest principal strain	$\sigma_{11}$	Normal stress on $x_1$ -surface
$\dot{\varepsilon}_{xx}$	Normal strain rate in x-direction	$\sigma_{22}$	Normal stress on $x_2$ -surface
$\dot{\varepsilon}_{yy}$	Normal strain rate on in y-direction	$\sigma_{33}$	Normal stress on $x_3$ -surface
$\dot{\varepsilon}_{zz}$	Normal strain rate in z-direction	$\sigma_{12}$	Shear stress on $x_1$ - and $x_2$ -surfaces
$\eta$	Stress ratio	$\sigma_{23}$	Shear stress on $x_2$ - and $x_3$ -surfaces
$\theta$	Lode angle	$\sigma_{31}$	Shear stress on $x_3$ - and $x_1$ -surfaces
$\kappa$	Hardening parameter	$\sigma_1$	First/greatest principal stress
		$\sigma_2$	Second/intermediate principal stress
		$\sigma_3$	Third/smallest principal stress

---

$\sigma_3^{\text{init}}$	Initial minimum stress
$\sigma_a$	Axial stress
$\sigma_e$	Von Mises stress
$\sigma_r$	Radial stress
$\tau_f$	Failure shear stress
$\phi$	Friction angle
$\phi_{\text{input}}$	Input friction angle
$\phi_{\text{reduced}}$	Reduced friction angle
$\psi$	Dilation angle
$\psi_0$	Input dilation angle
$\psi^*$	Been and Jefferies' state parameter
$\omega$	Over-relaxation factor

**Abbreviations:**

DOF	Degree of freedom
DP	Drucker–Prager
ESP	Effective stress path
FEA	Finite element analysis
FEM	Finite element method
MC	Mohr–Coulomb
PS	Plane strain
SOR	Successive over-relaxation
TXC	Triaxial compression
TXE	Triaxial extension



# Appendices



# Appendix A

## Task Description

Signed version inserted on next page.

**MASTER DEGREE THESIS**

Spring 2014

for

Vegard Gavel-Solberg

**Development and Implementation of Effective Stress Soil Models****BACKGROUND**

As part of the ongoing research project GeoFuture, an effective stress soil model for soft Scandinavian clays is developed by PhD Candidate Jon A. Rønningen at NTNU.

In this development various formulations and implementation procedures are considered. When implementing models in computer code one approach is to use modular programming in creation of subroutines. The approach makes it easy to change, extend or adjust formulations in the model. In order to further develop and test these principles it is desirable to implement constitutive models using the suggested modular approach.

**TASK**

The task is to study constitutive modeling of soil within the framework of elasto-plasticity. This shall be carried out by implementation of an elastic-plastic soil model into an existing computer program. The principles of modular programming shall be used. Validation of the model shall be executed by comparison to existing models.

**Task description**

The candidate shall obtain the required knowledge of constitutive soil modeling to implement a constitutive model. A simple linear elastic-perfect plastic effective stress based model shall be implemented as a user-defined soil model into PLAXIS, using MATLAB and the programming language FORTRAN. The Drucker-Prager strength criterion may be a relevant model for implementation. Validation of the model shall be executed by comparison to the standard models in PLAXIS.

If possible, further development of the model should be considered. Features like hardening, simple dilatancy formulations or stress dependent stiffness could be relevant for subsequent implementation.

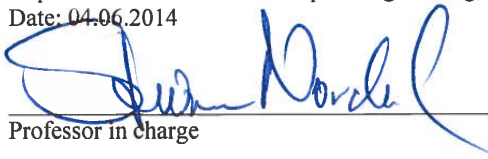
The student will work closely with PhD student Jon A. Rønningen.

**Professor in charge:** Steinar Nordal

**Other supervisors:** Gustav Grimstad and Jon A. Rønningen

Department of Civil and Transport Engineering, NTNU

Date: 04.06.2014



Professor in charge



# Appendix B

## Mathematical Derivations

### B.1 Lode Angle

A derivation of these coordinates with the sine function is done by Nordal (2012a). Here the derivation makes use of the cosine function. Inserting  $J_1 \equiv 0$  into equation (2.15) gives:

$$s^3 - J_2 s - J_3 = 0 \quad (\text{B.1})$$

The sine and cosine functions has the following properties:

$$\sin(\alpha \pm \beta) = \sin \alpha \cos \beta \pm \cos \alpha \sin \beta \quad (\text{B.2a})$$

$$\cos(\alpha \pm \beta) = \cos \alpha \cos \beta \mp \sin \alpha \sin \beta \quad (\text{B.2b})$$

Using this, a trigonometric identity may be derived, relating some angle  $\theta$  in a similar manner as the principal stress  $s$  in equation (B.1).

$$\begin{aligned} \cos(\theta + 2\theta) &= \cos \theta \cos(\theta + \theta) - \sin \theta \sin(\theta + \theta) \\ &= \cos \theta (\cos^2 \theta - \sin^2 \theta) - \sin \theta \cdot 2 \sin \theta \cos \theta \\ &= \cos^3 \theta - 3 \sin^2 \theta \cos \theta = 4 \cos^3 \theta - 3 \cos \theta \\ \implies \cos^3 \theta - \frac{3}{4} \cos \theta - \frac{1}{4} \cos(3\theta) &= 0 \end{aligned} \quad (\text{B.3})$$

A vector in the  $\Pi$ -plane will be the deviatoric part of the stress state, hence must the magnitude of a deviatoric vector be:

$$\rho = \sqrt{\mathbf{s} \cdot \mathbf{s}} = \sqrt{s_1^2 + s_2^2 + s_3^2} = \sqrt{2J_2} \quad (\text{B.4})$$

Expressed in polar coordinates,  $s$  must be on the form  $s = r \cos \theta$ . Inserted into equation (B.1) results in:

$$\cos^3 \theta - \frac{J_2}{r^2} \cos \theta - \frac{J_3}{r^3} = 0 \quad (\text{B.5})$$

Finally, balancing the coefficients of equations (B.3) and (B.5), expressions for  $r$  and  $\theta$  are obtained:

$$r = 2\sqrt{\frac{J_2}{3}} = \sqrt{\frac{2}{3}} \cdot \rho \quad (\text{B.6})$$

$$\cos 3\theta = \frac{4J_3}{r^3} = \frac{3\sqrt{3} \cdot J_3}{2\sqrt{J_2^3}} \quad (\text{B.7})$$

The expression for  $\cos 3\theta$  may be verified to always be within the interval  $[-1, 1]$  for all values of  $J_2$  and  $J_3$  (Nordal, 2012a). Hence, all solutions of equation (B.7) give  $3\theta \in [0, \pi]$ . As the cosine function is periodic,  $3\theta + 2\pi n$  are all solutions of equation (B.7). Thus,  $\theta + 2\pi n/3$  are all solutions resulting in different values for  $\cos \theta$ . Ordered according to  $\sigma_1 > \sigma_2 > \sigma_3$  and substituting  $s = r \cos \theta$ , the following relation between principal stresses and Haigh-Westergaard coordinates are obtained:

$$\begin{bmatrix} \sigma_1 \\ \sigma_2 \\ \sigma_3 \end{bmatrix} = 2\sqrt{\frac{J_2}{3}} \begin{bmatrix} \cos \theta \\ \cos(\theta - \frac{2\pi}{3}) \\ \cos(\theta + \frac{2\pi}{3}) \end{bmatrix} + \frac{I_1}{3} \begin{bmatrix} 1 \\ 1 \\ 1 \end{bmatrix}, \quad \text{for } \theta \in [0, \pi/3] \quad (\text{B.8})$$

Another scaled version of the invariant  $I_1$  may also be seen as the longitudinal coordinate,  $\xi = I_1/\sqrt{3}$ , such that the relations between the Haigh-Westergaard coordinates in stress space,  $(\xi, \rho, \theta)$ , and the principal stresses are:

$$\begin{bmatrix} \sigma_1 \\ \sigma_2 \\ \sigma_3 \end{bmatrix} = \frac{\xi}{\sqrt{3}} \begin{bmatrix} 1 \\ 1 \\ 1 \end{bmatrix} + \rho\sqrt{\frac{2}{3}} \begin{bmatrix} \cos \theta \\ \cos(\theta - \frac{2\pi}{3}) \\ \cos(\theta + \frac{2\pi}{3}) \end{bmatrix}, \quad \text{for } \theta \in [0, \pi/3] \quad (\text{B.9})$$

For the presented definition of the Lode angle  $\theta$ ,  $\theta = 0^\circ$  correspond to triaxial compression conditions (along the projection of the  $\sigma_1$ -axis), while  $\theta = 60^\circ$  correspond to triaxial extension conditions (along the projection negative extension of the  $\sigma_3$ -axis).

## B.2 Mohr–Coulomb Yield Surfaces in Haigh–Westergaard Coordinates

If the principal stress are not ordered, the Mohr–Coulomb criterion of equation (2.53) is defined by six surfaces:

$$\pm \frac{\sigma_1 - \sigma_2}{2} = \frac{\sigma_1 + \sigma_2}{2} \sin \phi + a \sin \phi \quad (\text{B.10a})$$

$$\pm \frac{\sigma_2 - \sigma_3}{2} = \frac{\sigma_2 + \sigma_3}{2} \sin \phi + a \sin \phi \quad (\text{B.10b})$$

$$\pm \frac{\sigma_3 - \sigma_1}{2} = \frac{\sigma_3 + \sigma_1}{2} \sin \phi + a \sin \phi \quad (\text{B.10c})$$

$$\sigma_1(\pm 1 - \sin \phi) - \sigma_2(\pm 1 + \sin \phi) = 2a \sin \phi \quad (\text{B.11a})$$

$$\implies \sigma_2(\pm 1 - \sin \phi) - \sigma_3(\pm 1 + \sin \phi) = 2a \sin \phi \quad (\text{B.11b})$$

$$\sigma_3(\pm 1 - \sin \phi) - \sigma_1(\pm 1 + \sin \phi) = 2a \sin \phi \quad (\text{B.11c})$$

In equation (B.9) the principal stresses are given as functions of the Haigh–Westergaard coordinates. Inserting this into the Mohr–Coulomb criterion gives:

$$\begin{aligned} & \left( \frac{1}{\sqrt{3}}\xi + \sqrt{\frac{2}{3}}\rho \cos \theta \right) (\pm 1 - \sin \phi) \\ & - \left( \frac{1}{\sqrt{3}}\xi + \sqrt{\frac{2}{3}}\rho \cos \left( \theta - \frac{2}{3}\pi \right) \right) (\pm 1 + \sin \phi) = 2a \sin \phi \quad (\text{B.12a}) \end{aligned}$$

$$\begin{aligned} & \left( \frac{1}{\sqrt{3}}\xi + \sqrt{\frac{2}{3}}\rho \cos \left( \theta - \frac{2}{3}\pi \right) \right) (\pm 1 - \sin \phi) \\ & - \left( \frac{1}{\sqrt{3}}\xi + \sqrt{\frac{2}{3}}\rho \cos \left( \theta + \frac{2}{3}\pi \right) \right) (\pm 1 + \sin \phi) = 2a \sin \phi \quad (\text{B.12b}) \end{aligned}$$

$$\begin{aligned} & \left( \frac{1}{\sqrt{3}}\xi + \sqrt{\frac{2}{3}}\rho \cos \left( \theta + \frac{2}{3}\pi \right) \right) (\pm 1 - \sin \phi) \\ & - \left( \frac{1}{\sqrt{3}}\xi + \sqrt{\frac{2}{3}}\rho \cos \theta \right) (\pm 1 + \sin \phi) = 2a \sin \phi \quad (\text{B.12c}) \end{aligned}$$

After gathering of terms, this may be expressed as:

$$\begin{aligned} \pm \rho \left[ \cos \left( \theta + \frac{2}{3}\pi \right) - \cos \theta \right] - \rho \sin \phi \left[ \cos \left( \theta + \frac{2}{3}\pi \right) + \cos \theta \right] \\ = \sqrt{6}a \sin \phi + \sqrt{2}\xi \sin \phi \quad (\text{B.13a}) \end{aligned}$$

$$\begin{aligned} \pm \rho \left[ \cos \left( \theta - \frac{2}{3}\pi \right) - \cos \left( \theta + \frac{2}{3}\pi \right) \right] - \rho \sin \phi \left[ \cos \left( \theta - \frac{2}{3}\pi \right) + \cos \left( \theta + \frac{2}{3}\pi \right) \right] \\ = \sqrt{6}a \sin \phi + \sqrt{2}\xi \sin \phi \quad (\text{B.13b}) \end{aligned}$$

$$\begin{aligned} \pm \rho \left[ \cos \theta - \cos \left( \theta - \frac{2}{3}\pi \right) \right] - \rho \sin \phi \left[ \cos \theta + \cos \left( \theta - \frac{2}{3}\pi \right) \right] \\ = \sqrt{6}a \sin \phi + \sqrt{2}\xi \sin \phi \quad (\text{B.13c}) \end{aligned}$$

To simplify the expression some trigonometric relations are used:

$$\cos \alpha + \cos \beta = 2 \cos \frac{\alpha + \beta}{2} \cos \frac{\alpha - \beta}{2} \quad (\text{B.14a})$$

$$\cos \alpha - \cos \beta = -2 \sin \frac{\alpha + \beta}{2} \sin \frac{\alpha - \beta}{2} \quad (\text{B.14b})$$

Thus, the following following simplifications can be made:

$$\cos \theta + \cos \left( \theta + \frac{2}{3}\pi \right) = \cos \left( \theta + \frac{\pi}{3} \right) \quad (\text{B.15a})$$

$$\cos \theta - \cos \left( \theta + \frac{2}{3}\pi \right) = \sqrt{3} \sin \left( \theta + \frac{\pi}{3} \right) \quad (\text{B.15b})$$

$$\cos \left( \theta - \frac{2}{3}\pi \right) + \cos \left( \theta + \frac{2}{3}\pi \right) = -\cos \theta \quad (\text{B.15c})$$

$$\cos \left( \theta - \frac{2}{3}\pi \right) - \cos \left( \theta + \frac{2}{3}\pi \right) = -\sqrt{3} \sin \theta \quad (\text{B.15d})$$

$$\cos \left( \theta - \frac{2}{3}\pi \right) + \cos \theta = \cos \left( \theta - \frac{\pi}{3} \right) \quad (\text{B.15e})$$

$$\cos \left( \theta - \frac{2}{3}\pi \right) - \cos \theta = \sqrt{3} \sin \left( \theta - \frac{\pi}{3} \right) \quad (\text{B.15f})$$

Inserting the trigonometric relations and gathering  $\rho = \rho(\xi, \theta)$  on the left hand side, the expressions for the Mohr–Coulomb surfaces in Haigh–Westergaard

coordinates are obtained as:

$$\rho(\xi, \theta) = \frac{\sqrt{6}a \sin \phi + \sqrt{2}\xi \sin \phi}{\pm\sqrt{3} \sin(\theta + \frac{\pi}{3}) - \cos(\theta + \frac{\pi}{3}) \sin \phi} \quad (\text{B.16a})$$

$$\rho(\xi, \theta) = \frac{\sqrt{6}a \sin \phi + \sqrt{2}\xi \sin \phi}{\pm\sqrt{3} \sin \theta + \cos \theta \sin \phi} \quad (\text{B.16b})$$

$$\rho(\xi, \theta) = \frac{\sqrt{6}a \sin \phi + \sqrt{2}\xi \sin \phi}{\pm\sqrt{3} \sin(\theta - \frac{\pi}{3}) - \cos(\theta - \frac{\pi}{3}) \sin \phi} \quad (\text{B.16c})$$



# Appendix C

## Material Independent Subroutines

### C.1 Main Subroutine

```
1      Subroutine User_Mod ( IDTask, iMod, IsUndr ,
2      *                    iStep , iTer , iEl , Int ,
3      *                    X, Y, Z,
4      *                    Time0, dTime,
5      *                    Props , Sig0 , Swp0, StVar0 ,
6      *                    dEps, D, BulkW,
7      *                    Sig , Swp, StVar, ipl ,
8      *                    nStat , NonSym, iStrsDep , iTimeDep ,
9      *                    iTang , iPrjDir , iPrjLen , iAbort )
10     use vars
11     Implicit Double Precision (A-H,O-Z)
12
13     Integer :: IDTask , iMod , IsUndr , iStep , iter , iel , Int
14     Real(8) :: X, Y, Z, Time0, dTime, Props(50), Sig0(20),
15     &          Swp0, StVar0(nStat), dEps(12)
16     Real(8) :: D(6,6), BulkW
17     Real(8) :: Sig(6), Swp, StVar(nStat)
18     Integer :: NonSym, iStrsDep , iTimeDep , iTang , iAbort
19     Integer :: nStat
20     Integer :: iPrjDir(iPrjLen), iPrjLen
21
22     if(IDTask.eq.1) then
23         call CopyRVec(Props , c , size(c))
24         call MZeroR(StVar0 , 7)
25         call MZeroR(v0 , 7)
26         call MZeroR(v , 7)
```

```

27     end if !End IDTask 1
28
29     if(IDTask.eq.2) then
30     ipls = 0 ! Resetting tension point marker
31
32     ! Activate internal parameters and start values
33     if(ALL(StVar0(1:6).eq.0d0)) then
34         call CopyRVec(-Sig0 ,StVar0(1:6) ,6)
35         call CopyRVec(StVar0 ,v0 ,7)
36     else
37         call CopyRVec(StVar0 ,v0 ,7)
38     end if
39
40     ! Activate strains
41     call CopyRVec(dEps(1:6) ,de ,6)
42     epsV=dEps(1)+dEps(2)+dEps(3)+dEps(7)+dEps(8)+dEps(9)
43
44     ! Calculate trial stresses and yield condition
45     vs(7) = v0(7)
46     call calcond(f)
47
48     ! Find correct stress , Sig
49     if (ipls.eq.2) then !Apex point
50         v = (/ -a,-a,-a,0d0,0d0,0d0,StVar0(7)/) ! Calculating v
51         call CopyRVec(v,StVar,7) ! Storing v in StVar
52         call MulVec(v,-1d0,7) ! Due to sign convention
53         call CopyRVec(v(1:6),Sig,6)
54         ipl = 2 ! Tension cut-off point
55     elseif(f.ge.1d-6) then ! Plastic increment
56         call NR(v) ! Calculating v
57         nrabort = 1
58         call CopyRVec(v,StVar,7) ! Storing v in StVar
59         call MulVec(v,-1d0,7) ! Due to sign convention
60         call CopyRVec(v(1:6),Sig,6) ! Stress = NR-solution
61         ipl = 1 ! Failure
62     else !Elastic increment
63         call CopyRVec(Sigtr ,v(1:6) ,6) ! "Calculating" v
64         v(7) = StVar0(7) ! No change
65         call CopyRVec(v,StVar,7) ! Storing v in StVar
66         call MulVec(Sigtr,-1d0,6) ! Due to sign convention
67         call CopyRVec(Sigtr ,Sig ,6) ! Stress = trial stress
68         ipl = 0 ! Elastic
69     end if
70

```



```
71     if (IsUndr.eq.1) then
72         Swp = Swp0 + BulkW*(dEps(1)+dEps(2)+dEps(3))
73     else
74         Swp = Swp0
75     end if
76
77     end if !End IDTask 2
78
79
80     if(IDTask.eq.3) then
81     if (Sig0(15).gt.1d-2)then !Avoid dividing by 0
82         Msf = Sig0(15)
83     end if
84     call Dmatrix(D)
85     end if !End IDTask 3
86
87     if(IDTask.eq.4) then
88     nStat = size(v)
89     end if !End IDTask 4
90
91     if(IDTask.eq.5) then
92     NonSym = 0 ! 1 for non-symmetric D-matrix
93     iStrsDep = 0 ! 1 for stress dependent D-matrix
94     iTang = 0 ! 1 for tangent D-matrix
95     iTimeDep = 0 ! 1 for time dependent D-matrix
96     end if !End IDTask 5
97
98     if(IDTask.eq.6) then
99     if (Sig0(15).gt.1d-2)then !Avoid dividing by 0
100         Msf = Sig0(15)
101     end if
102     call Dmatrix(D)
103     end if !End IDTask 6
104
105     end subroutine
106
107
108     include 'vars.f'
109     include 'helper.f'
110     include 'drupra.f'
111     include 'usr_add.f'
112     include 'usr_lib.f'
```

## C.2 Helper Subroutine

```

1      recursive subroutine NR(vo)
2          use vars
3          Implicit Double Precision (A-H,O-Z)
4          double precision , intent(out) :: vo(7)
5          double precision :: dv(7)           ! Temporary vector
6          double precision :: Jac(7,7)
7          double precision :: tol , dotprod , fac , fp , res
8          integer :: itr , maxitr , cnt , nc , recuritr
9
10         ! Initializing subroutine variable
11         itr = 0
12         tol = 1d-6
13         res = 1/tol
14         recuritr = 50
15         maxitr = recuritr +5
16         call CopyRVec(vs0 , vs , 7)
17         call MZeroR(r , 7)
18         call MZeroR(dv , 7)
19         cnt = 1
20
21         ! NR-routine
22         do while(res.gt.tol)
23             if (itr.le.recuritr) then
24                 call jacobian(Jac)
25                 call resi(r)
26                 call gauss(Jac,-r,dv,size(dv))
27                 call AddVec(vs,dv,1d0,1d0,7,vs)
28
29                 itr = itr+1
30                 dotprod = DInProd(r,r,size(r))
31                 res = sqrt(dotprod)
32             else if (itr.gt.recuritr) then ! Recursion loop
33                 call prI(nrabort)
34                 if(nrabort.gt.5) then
35                     stop
36                 end if
37                 cnt = 2*cnt
38                 fac = 1d0/real(cnt,8)
39                 call MulVec(de,fac,size(de))
40
41                 do nc =1,cnt
42                     ipls = 0

```

```
43         call calcond(fp)
44         if (fp.gt.1d-6) then
45             call NR(vs)
46         else
47             call CopyRVec(Sigtr , vs(1:6) ,6)
48             vs(7) = vs0(7)
49         end if
50         call CopyRVec(vs , vs0 , size(vs))
51         call CopyRVec(vs , v0 , size(vs))
52     end do
53
54     nrabort = nrabort+1
55     itr = itr+1
56     dotprod = DInProd(r , r , size(r))
57     res = sqrt(dotprod)
58     else if (itr.gt.maxitr) then
59         stop
60     end if
61 end do
62
63 ! Storing the result vs to the output vector vo
64 call CopyRVec(vs , vo , size(vs))
65
66     end subroutine
67
68     subroutine gauss(a,b,x,n)
69
70 ! Comment, VGS, February 24, 2014:
71 !This subroutine has been downloaded from
72 !http://ww2.odu.edu/~agodunov/computing/programs/index.html
73 !Credits: Alexander L Godunov, Department of Physics ,
74 !             Old Dominion University , Norfolk , VA
75
76 

---



---


77 ! Solutions to a system of linear equations A*x=b
78 ! Method: Gauss elimination (with scaling and pivoting)
79 ! Alex G. (November 2009)
80 

---


81 ! input ...
82 ! a(n,n) – array of coefficients for matrix A
83 ! b(n)   – array of the right hand coefficients b
84 ! n      – number of equations (size of matrix A)
85 ! output ...
86 ! x(n)   – solutions
```

```

87 | ! comments ...
88 | ! the original arrays a(n,n) and b(n) will be destroyed
89 | ! during the calculation
90 | =====
91 |     implicit none
92 |     integer n
93 |     double precision a(n,n), b(n), x(n)
94 |     double precision s(n)
95 |     double precision c, pivot, store
96 |     integer i, j, k, l
97 |
98 |     ! step 1: begin forward elimination
99 |     do k=1, n-1
100 |
101 |         ! step 2: "scaling"
102 |         ! s(i) will have the largest element from row i
103 |         do i=k,n          ! loop over rows
104 |             s(i) = 0.0
105 |             do j=k,n      ! loop over elements of row i
106 |                 s(i) = max(s(i),abs(a(i,j)))
107 |             end do
108 |         end do
109 |
110 |         ! step 3: "pivoting 1"
111 |         ! find a row with the largest pivoting element
112 |         pivot = abs(a(k,k)/s(k))
113 |         l = k
114 |         do j=k+1,n
115 |             if(abs(a(j,k)/s(j)) > pivot) then
116 |                 pivot = abs(a(j,k)/s(j))
117 |                 l = j
118 |             end if
119 |         end do
120 |
121 |         ! Check if the system has a singular matrix
122 |         if(pivot == 0.0) then
123 |             call prC("The matrix is singular")
124 |             return
125 |         end if
126 |
127 |         ! step 4: "pivoting 2" interchange
128 |         !                               rows k and l (if needed)
129 |         if (l /= k) then
130 |             do j=k,n

```

```
131         store = a(k,j)
132         a(k,j) = a(1,j)
133         a(1,j) = store
134     end do
135     store = b(k)
136     b(k) = b(1)
137     b(1) = store
138 end if
139
140 ! step 5: the elimination
141 !                               (after scaling and pivoting)
142     do i=k+1,n
143         c=a(i,k)/a(k,k)
144         a(i,k) = 0.0
145         b(i)=b(i)- c*b(k)
146         do j=k+1,n
147             a(i,j) = a(i,j)-c*a(k,j)
148         end do
149     end do
150 end do
151
152 ! step 6: back substiturion
153 x(n) = b(n)/a(n,n)
154 do i=n-1,1,-1
155     c=0.0
156     do j=i+1,n
157         c= c + a(i,j)*x(j)
158     end do
159     x(i) = (b(i)- c)/a(i,i)
160 end do
161
162 end subroutine gauss
```



# Appendix D

## Material Dependent Codes

Due to readability, the code below is slightly modified from the actual code. The code is written in fixed form due to the GNU compiler used does not support free format. Thus, the first six columns are reserved for special purposes. Below, the first five columns are removed and some comments are shortened.

### D.1 Fortran Subroutine

```
1  subroutine alfcalc ()
2  use vars
3  Implicit Double Precision (A-H,O-Z)
4  double precision :: sinrho
5
6  sinrho = (H0*vs(7))/(1d0+H0*vs(7)/sin(phirad))
7  alpha=(2d0*sinrho)/((sqrt(3d0))*(3d0-sinrho)) !TXC
8  !alpha=(2d0*sinrho)/((sqrt(3d0))*(3d0+sinrho)) !TXE
9  !alpha=sinrho/((sqrt(3d0))*(sqrt(3d0+sinrho**2))) !PS
10 xky = 3d0*alpha*a
11
12 end subroutine
13
14 subroutine Dmatrix (D)
15 use vars
16 Implicit Double Precision (A-H,O-Z)
17 Real(8) :: D(6,6), e,p0
18
19 p0 = (v0(1)+v0(2)+v0(3))/3d0
20 if (p0.lt.1d0) then
21   p0 = 1d0
22 end if
23 xG = c(1) * sqrt(p0/c(10))
```

```

24 BFac = (2d0*(1d0+c(2)))/(3d0*(1-2d0*c(2))) ! K/G
25 a = c(3)
26 phirad = c(4)*pi/180d0 ! Friction angle in radians
27 phirad = atan(tan(phirad)/Msf)
28 psirad = c(5)*pi/180d0 ! Dilation angle in radians
29 if (psirad.gt.phirad) then ! Necessary for Safety-calculations
30     psirad = phirad
31 end if
32 sinpsi0 = sin(psirad)
33 H0 = c(6)
34 e0 = c(7)
35 elam = c(8)
36 xlams = c(9)
37 e = (e0+epsV)/(1-epsV)
38 pref = 1d1**((elam-e)/xlams)
39
40 do i =1,6
41     do j = 1,6
42         Dm(i,j) =0d0
43     end do
44 end do
45 do i =1,3
46     do j = 1,3
47         Dm(i,j) = (BFac - 2d0/3d0)*xG
48     end do
49     Dm(i,i) = (BFac + 4d0/3d0)*xG
50     Dm(i+3,i+3) = xG
51
52 end do
53 D = Dm
54
55 end subroutine
56
57 subroutine calcstrinv(Si)
58 use vars
59 Implicit Double Precision (A-H,O-Z)
60 real(8) :: Si1, Si2, Si3, xN1(3), xN2(3), xN3(3)
61 real(8), dimension(6), intent(in) :: Si
62 integer iOpt
63
64 iOpt = 0
65 call PrnSig(iOpt, Si, xN1, xN2, xN3, Si1, Si2, Si3, p, q)
66 if (p .lt.(-a)) then
67     ipls = 2

```



```

68  end if
69  xJ2=((Si1-Si2)**2d0+(Si2-Si3)**2d0+(Si3-Si1)**2d0)*1d0/6d0
70
71  subroutine calcond(fs)
72    use vars
73    Implicit Double Precision (A-H,O-Z)
74    double precision, intent(out) :: fs
75    double precision :: dSigtr(6), f0, beta
76
77    call calcstrinv(v0(1:6))
78    f0 = sqrt(xJ2)-alpha*(p)*3d0-xky ! yield criterion using I1=3p
79
80    call MatVec(Dm,6,de,6,dSigtr) ! Elastic stress increment
81    call AddVec(v0(1:6),dSigtr,1d0,-1d0,6,Sigtr) ! Trial stress.
82    call calcstrinv(Sigtr)
83    fs = sqrt(xJ2)-alpha*(p)*3d0-xky ! yield criterion using I1=3p
84
85    if (fs.gt.1d-6) then
86      if (f0.lt.-1d-6) then
87        beta = f0/(f0-fs)
88        call MulVec(dSigtr,beta,size(dSigtr))
89        call AddVec(v0(1:6),dSigtr,1d0,-1d0,6,vs0(1:6))
90        vs0(7) = v0(7)
91      else
92        call CopyRVec(v0,vs0,7)
93      end if
94    end if
95  end subroutine
96
97  subroutine differentials(A0)
98    use vars
99    Implicit Double Precision (A-H,O-Z)
100   double precision, dimension(6), intent(out) :: A0
101   double precision :: sig11,sig22,sig33,sig12,sig23,sig31
102   double precision :: t2,t3,t4,t5,t6,t7,t8,t9,t10,t11,t12
103   double precision :: t13,t14,t15,t16,t17,t18,t19,t20,t21,t22
104   double precision :: t23,t24,t25,t26,t27,t28,t29,t30,t31
105
106   call MZeroR(A0,6)
107   sig11 = vs(1)
108   sig22 = vs(2)
109   sig33 = vs(3)
110   sig12 = vs(4)
111   sig23 = vs(5)

```

```

112   sig31 = vs(6)
113   xlam = vs(7)
114
115   t2 = sig22*(1.0D0/3.0D0)
116   t4 = sig11*(1.0D0/3.0D0)
117   t15 = sig33*(2.0D0/3.0D0)
118   t3 = t2+t4-t15
119   t5 = sig33*(1.0D0/3.0D0)
120   t14 = sig22*(2.0D0/3.0D0)
121   t6 = t4+t5-t14
122   t20 = sig11*(2.0D0/3.0D0)
123   t7 = t2+t5-t20
124   t8 = sqrt(3.0D0)
125   t9 = 1.0D0/pref
126   t10 = sinpsi0**2
127   t11 = t10+3.0D0
128   t12 = 1.0D0/sqrt(t11)
129   t13 = t2+t4+t5
130   t16 = t3**2
131   t17 = t16*(1.0D0/2.0D0)
132   t18 = t6**2
133   t19 = t18*(1.0D0/2.0D0)
134   t21 = t7**2
135   t22 = t21*(1.0D0/2.0D0)
136   t23 = sig12**2
137   t24 = sig23**2
138   t25 = sig31**2
139   t26 = t17+t19+t22+t23+t24+t25
140   if (t26.lt.1d-6) then
141     t26 = 1d-6! t26 = xJ2, avoid dividing by zero
142   end if
143   t27 = 1.0D0/sqrt(t26)
144   t28 = t9*t13*(1.0D0/2.0D0)
145   t29 = t28-1.0D0
146   t30 = sinpsi0*t8*t12*t29*(1.0D0/9.0D0)
147   t31 = sinpsi0*t8*t9*t12*t13*(1.0D0/1.8D1)
148   A0(1) = t30+t31-t7*t27*(1.0D0/2.0D0)
149   A0(2) = t30+t31-t6*t27*(1.0D0/2.0D0)
150   A0(3) = t30+t31-t3*t27*(1.0D0/2.0D0)
151   A0(4) = sig12*t27
152   A0(5) = sig23*t27
153   A0(6) = sig31*t27
154
155 end subroutine

```

```

156
157 subroutine resi(rr)
158 use vars
159 Implicit Double Precision (A-H,O-Z)
160 double precision, dimension(6) :: depspl, diffsigsigtr
161 double precision, dimension(6) :: deltasig, dqdsig
162 double precision, dimension(7), intent(out) :: rr
163
164 call MZeroR(rr,7)
165 call MZeroR(diffsigsigtr,6)
166 call MZeroR(dqdsig,6)
167 call MZeroR(depspl,6)
168 call MZeroR(deltasig,6)
169
170 call AddVec(vs(1:6), Sigtr,1d0,-1d0,6, diffsigsigtr)
171 call differentials(dqdsig)
172 call MatVec(Dm,6,dqdsig,6,depspl)
173 call MulVec(depspl,(vs(7)-v0(7)),6)
174 call AddVec(diffsigsigtr,depspl,1d0,1d0,6,rr(1:6))
175 call calcstrinv(vs(1:6))
176 call alfcalc()
177 rr(7) = sqrt(xJ2)-alpha*(p)*3d0-xky ! I1 = 3p
178
179 end subroutine
180
181 subroutine jacobian(A0)
182 use vars
183 Implicit Double Precision (A-H,O-Z)
184 double precision, dimension(7,7), intent(out) :: A0
185 double precision :: sig11,sig22,sig33,sig12,sig23,sig31,xK
186 double precision :: xlam,xlam0
187 double precision :: t2,t3,t4,t5,t6,t7,t8,t9,t10,t11,t12
188 double precision :: t13,t14,t15,t16,t17,t18,t19,t20,t21,t22
189 double precision :: t23,t24,t25,t26,t27,t28,t29,t30,t50,t31
190 double precision :: t32,t33,t34,t53,t35,t36,t37,t56,t38,t39
191 double precision :: t40,t41,t42,t43,t44,t45,t46,t47,t48,t49
192 double precision :: t51,t52,t54,t55,t57,t58,t59,t60,t61,t62
193 double precision :: t63,t64,t65,t66,t67,t68,t69,t70,t71,t72
194 double precision :: t73,t74,t75,t76,t77,t78,t79,t80,t81,t82
195 double precision :: t83,t84,t85,t86,t87,t88,t89,t90
196
197 sig11 = vs(1)
198 sig22 = vs(2)
199 sig33 = vs(3)

```

```

200 sig12 = vs(4)
201 sig23 = vs(5)
202 sig31 = vs(6)
203 xlam = abs(vs(7))
204 xlam0 = abs(v0(7))
205 xK = BFac*xG
206 sinphi = sin(phirad)
207
208 t3 = sig11*(1.0D0/3.0D0)
209 t5 = sig22*(1.0D0/3.0D0)
210 t8 = sig33*(2.0D0/3.0D0)
211 t2 = t3+t5-t8
212 t6 = sig33*(1.0D0/3.0D0)
213 t12 = sig22*(2.0D0/3.0D0)
214 t4 = t3+t6-t12
215 t9 = sig11*(2.0D0/3.0D0)
216 t7 = t5+t6-t9
217 t10 = t2**2
218 t11 = t10*(1.0D0/2.0D0)
219 t13 = t4**2
220 t14 = t13*(1.0D0/2.0D0)
221 t15 = t7**2
222 t16 = t15*(1.0D0/2.0D0)
223 t17 = sig12**2
224 t18 = sig23**2
225 t19 = sig31**2
226 t20 = t11+t14+t16+t17+t18+t19 ! t20 = xJ2
227 if (t20.lt.1d-6) then
228     t20 = 1d-6
229 end if
230 t21 = xG*(2.0D0/3.0D0)
231 t22 = t21-xK
232 t23 = 1.0D0/sqrt(t20)
233 t24 = t23*(1.0D0/6.0D0)
234 t25 = 1.0D0/t20**(3.0D0/2.0D0)
235 t26 = sqrt(3.0D0)
236 t27 = 1.0D0/pref
237 t28 = sinpsi0**2
238 t29 = t28+3.0D0
239 t30 = 1.0D0/sqrt(t29)
240 t31 = xlam-xlam0
241 t32 = t23*(1.0D0/3.0D0)
242 t33 = sinpsi0*t26*t27*t30*(1.0D0/2.7D1)
243 t34 = xG*(4.0D0/3.0D0)

```

```
244 t35 = t34+xK
245 t36 = t4*t7*t25*(1.0D0/4.0D0)
246 t37 = t2*t7*t25*(1.0D0/4.0D0)
247 t38 = t2*t4*t25*(1.0D0/4.0D0)
248 t39 = t24-t33+t38
249 t40 = t3+t5+t6
250 t41 = t27*t40*(1.0D0/2.0D0)
251 t42 = t41-1.0D0
252 t43 = sinpsi0*t26*t30*t42*(1.0D0/9.0D0)
253 t44 = sinpsi0*t26*t27*t30*t40*(1.0D0/1.8D1)
254 t58 = t15*t25*(1.0D0/4.0D0)
255 t45 = t32+t33-t58
256 t46 = t24-t33+t36
257 t47 = t35*t46
258 t48 = t24-t33+t37
259 t62 = t13*t25*(1.0D0/4.0D0)
260 t49 = t32+t33-t62
261 t66 = t10*t25*(1.0D0/4.0D0)
262 t50 = t32+t33-t66
263 t51 = t22*t50
264 t52 = sig12*t2*t22*t25*(1.0D0/2.0D0)
265 t53 = sig23*t2*t22*t25*(1.0D0/2.0D0)
266 t54 = sig31*t2*t22*t25*(1.0D0/2.0D0)
267 t74 = t4*t23*(1.0D0/2.0D0)
268 t55 = t43+t44-t74
269 t73 = t2*t23*(1.0D0/2.0D0)
270 t56 = t43+t44-t73
271 t75 = t7*t23*(1.0D0/2.0D0)
272 t57 = t43+t44-t75
273 t59 = t22*t45
274 t60 = t35*t48
275 t61 = t22*t46
276 t63 = t22*t49
277 t64 = t35*t39
278 t65 = t22*t39
279 t67 = sig12*t4*t22*t25*(1.0D0/2.0D0)
280 t68 = sig12*t7*t22*t25*(1.0D0/2.0D0)
281 t69 = sig23*t4*t22*t25*(1.0D0/2.0D0)
282 t70 = sig23*t7*t22*t25*(1.0D0/2.0D0)
283 t71 = sig31*t4*t22*t25*(1.0D0/2.0D0)
284 t72 = sig31*t7*t22*t25*(1.0D0/2.0D0)
285 t76 = t23*t31*xG
286 t77 = 1.0D0/sin(phirad)
287 t78 = H0*t77*xlam
```

```

288 t79 = t78+1.0D0
289 t80 = 1.0D0/t79
290 t81 = H0**2
291 t82 = xlam**2
292 t83 = 1.0D0/t79**2
293 t84 = t81*t82*t83
294 t85 = t84+3.0D0
295 t86 = 1.0D0/sqrt(t85)
296 t87 = 1.0D0/t85**(3.0D0/2.0D0)
297 t88 = t81*t83*xlam*2.0D0
298 t89 = 1.0D0/t79**3
299 t90 = t88-H0*t77*t81*t82*t89*2.0D0
300 A0(1,1)=t31*(t35*t45+t22*(t24+t36-sinpsi0*t26*t27*t30*(1.0D0/2.7
301 +D1))+t22*(t24+t37-sinpsi0*t26*t27*t30*(1.0D0/2.7D1)))+1.0D0
302 A0(1,2) = -t31*(t47+t63-t22*t39)
303 A0(1,3) = -t31*(t51+t60-t22*t39)
304 A0(1,4) = -t31*(t52+t67-sig12*t7*t25*t35*(1.0D0/2.0D0))
305 A0(1,5) = -t31*(t53+t69-sig23*t7*t25*t35*(1.0D0/2.0D0))
306 A0(1,6) = -t31*(t54+t71-sig31*t7*t25*t35*(1.0D0/2.0D0))
307 A0(1,7) = -t22*t55-t22*t56+t35*t57
308 A0(2,1) = -t31*(t47+t59-t22*t48)
309 A0(2,2) = t31*(t61+t65+t35*t49)+1.0D0
310 A0(2,3) = -t31*(t51+t64-t22*t48)
311 A0(2,4) = -t31*(t52+t68-sig12*t4*t25*t35*(1.0D0/2.0D0))
312 A0(2,5) = -t31*(t53+t70-sig23*t4*t25*t35*(1.0D0/2.0D0))
313 A0(2,6) = -t31*(t54+t72-sig31*t4*t25*t35*(1.0D0/2.0D0))
314 A0(2,7) = -t22*t56-t22*t57+t35*t55
315 A0(3,1) = -t31*(t59+t60-t61)
316 A0(3,2) = -t31*(-t61+t63+t64)
317 A0(3,3) = t31*(t65+t22*t48+t35*t50)+1.0D0
318 A0(3,4) = -t31*(t67+t68-sig12*t2*t25*t35*(1.0D0/2.0D0))
319 A0(3,5) = -t31*(t69+t70-sig23*t2*t25*t35*(1.0D0/2.0D0))
320 A0(3,6) = -t31*(t71+t72-sig31*t2*t25*t35*(1.0D0/2.0D0))
321 A0(3,7) = -t22*t55-t22*t57+t35*t56
322 A0(4,1) = sig12*t7*t25*t31*xG*(1.0D0/2.0D0)
323 A0(4,2) = sig12*t4*t25*t31*xG*(1.0D0/2.0D0)
324 A0(4,3) = sig12*t2*t25*t31*xG*(1.0D0/2.0D0)
325 A0(4,4) = t76-t17*t25*t31*xG+1.0D0
326 A0(4,5) = -sig12*sig23*t25*t31*xG
327 A0(4,6) = -sig12*sig31*t25*t31*xG
328 A0(4,7) = sig12*t23*xG
329 A0(5,1) = sig23*t7*t25*t31*xG*(1.0D0/2.0D0)
330 A0(5,2) = sig23*t4*t25*t31*xG*(1.0D0/2.0D0)
331 A0(5,3) = sig23*t2*t25*t31*xG*(1.0D0/2.0D0)

```

```

332 A0(5,4) = -sig12*sig23*t25*t31*xG
333 A0(5,5) = t76-t18*t25*t31*xG+1.0D0
334 A0(5,6) = -sig23*sig31*t25*t31*xG
335 A0(5,7) = sig23*t23*xG
336 A0(6,1) = sig31*t7*t25*t31*xG*(1.0D0/2.0D0)
337 A0(6,2) = sig31*t4*t25*t31*xG*(1.0D0/2.0D0)
338 A0(6,3) = sig31*t2*t25*t31*xG*(1.0D0/2.0D0)
339 A0(6,4) = -sig12*sig31*t25*t31*xG
340 A0(6,5) = -sig23*sig31*t25*t31*xG
341 A0(6,6) = t76-t19*t25*t31*xG+1.0D0
342 A0(6,7) = sig31*t23*xG
343 A0(7,1) = -t75-H0*t26*t80*t86*xlam*(1.0D0/3.0D0)
344 A0(7,2) = -t74-H0*t26*t80*t86*xlam*(1.0D0/3.0D0)
345 A0(7,3) = -t73-H0*t26*t80*t86*xlam*(1.0D0/3.0D0)
346 A0(7,4) = sig12*t23
347 A0(7,5) = sig23*t23
348 A0(7,6) = sig31*t23
349 A0(7,7)=-H0*a*t26*t80*t86-H0*t26*t40*t80*t86+H0*a*t26*t80*t87*t9
350 &0*xlam*(1.0D0/2.0D0)+H0*t26*t40*t80*t87*t90*xlam*(1.0D0/2.0D0)+
351 &a*t26*t77*t81*t83*t86*xlam+t26*t40*t77*t81*t83*t86*xlam
352
353 end subroutine

```

## D.2 MATLAB Script

```

1 clear all
2
3 syms sigtr11 sigtr22 sigtr33 sigtr12 sigtr23 sigtr31
4 syms sig11 sig22 sig33 sig12 sig23 sig31
5 syms xK xG dQdsig
6 syms Q F xlam xlam0 alpha alphaQ p pref xJ2 xkf sinpsi
7 syms v r J sinrho H0 sinphi a sinpsi0 alphaQ0
8
9
10 p = (sig11 +sig22 + sig33)/3;
11 Sigtr = [sigtr11; sigtr22; sigtr33; sigtr12; sigtr23; sigtr31];
12 Sig = [sig11; sig22; sig33; sig12; sig23; sig31];
13 S = Sig - p*[1; 1; 1; 0; 0; 0];
14
15 sinrho = H0*xlam/(1+H0*xlam/sinphi);
16 xJ2 = 0.5*(S(1)^2+S(2)^2+S(3)^2+2*S(4)^2+2*S(5)^2+2*S(6)^2);
17
18 alpha = 2*sinrho/(sqrt(3)*(3-sinrho)); %TXC

```

```

19 alphaQ0 = 2*sinpsi0/(sqrt(3)*(3-sinpsi0)); %TXC
20 %alpha = 2*sinrho/(sqrt(3)*(3+sinrho)); %TXE
21 %alphaQ0 = 2*sinpsi0/(sqrt(3)*(3+sinpsi0)); %TXE
22 %alpha = sinrho/(sqrt(3)*sqrt(3+sinrho^2)); %PS
23 %alphaQ0 = sinpsi0/(sqrt(3)*sqrt(3+sinpsi0^2)); %PS
24
25 xkf = 3*alpha*a;
26 alphaQ = alphaQ0*(1-p/(2*pref));
27
28 v = [Sig; xlam];
29 F = sqrt(xJ2) - alpha*3*p - xkf;
30 Q = sqrt(xJ2) - alphaQ*3*p;
31
32 for i = 1:3
33     for j = 1:3
34         D(i,j) = xK - 2*xG/3;
35     end
36     D(i,i) = xK + 4*xG/3;
37     D(i+3,i+3) = xG;
38 end
39
40 for i = 1:6
41     dQdsig(i,1) = diff(Q, Sig(i));
42 end
43
44 r = [Sig - Sigtr + D*dQdsig*(xlam-xlam0); F];
45
46
47 for i = 1:7
48     for j = 1:7
49         J(i,j) = diff(r(i),v(j)); %"J = drdv"
50     end
51 end
52
53 fortran(J, 'file', 'jac.f')
54 fortran(dQdsig, 'file', 'dQdsig.f')

```



## D.3 vars.f-module

```
1  module vars
2    double precision , dimension(7) :: v, v0, vs, vs0, r
3    double precision , dimension(6) :: de, Sigtr
4    double precision , dimension(10) :: c
5    double precision , dimension(7,7) :: dvdr
6    double precision , dimension(6,6) :: Dm
7    double precision :: xG, BFac, a, phirad, alpha, xky
8    double precision :: P, Q, xJ2, Msf, alphaQ, psirad, H0, pref
9    double precision :: sinpsi0, xn, epsV, elam, e0, xlams
10   double precision , parameter :: pi=3.141592654
11   integer :: i,j, ipls, nrabort
12 end module vars
```



# Appendix E

## Documentation of Calculations

### E.1 Load-Displacement Curves

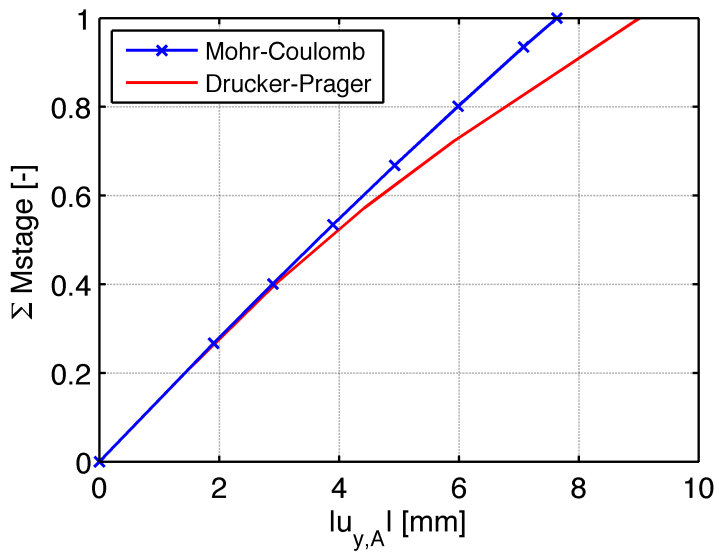


**Figure E.1:** Load-deformation curve for material parameter Set 6 ( $\phi = 30^\circ$ ,  $\psi = 0^\circ$ ).

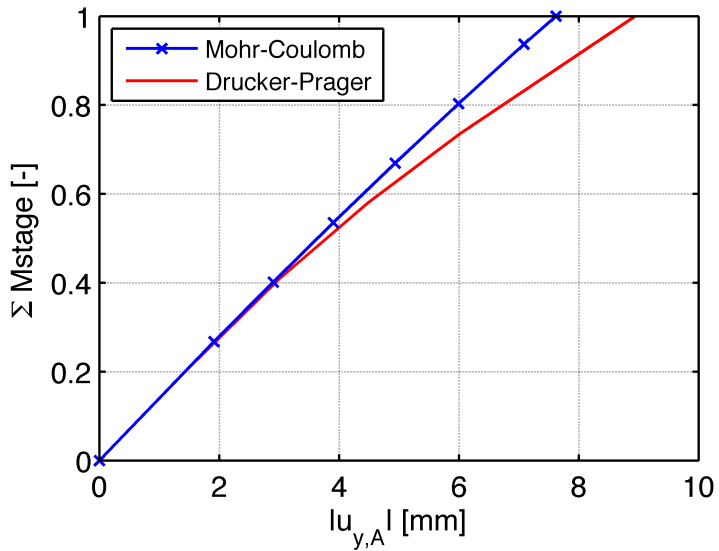


**Figure E.2:** Load-deformation curve for material parameter Set 7 ( $\phi = 30^\circ$ ,  $\psi = 1^\circ$ ).

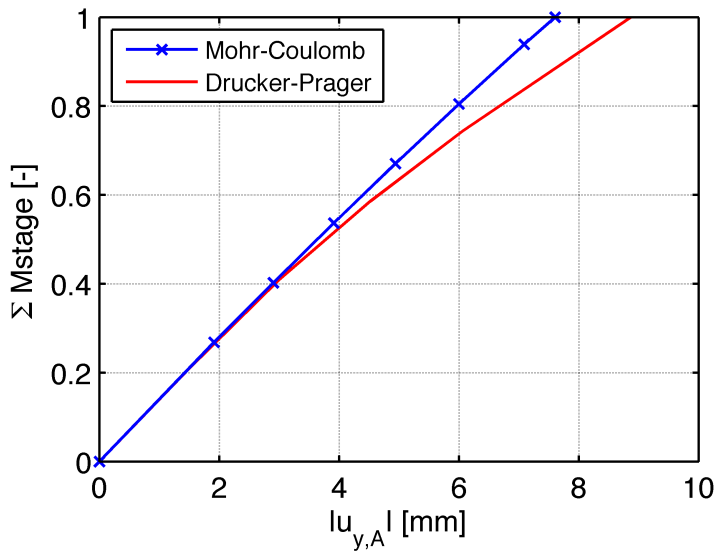


**Figure E.3:** Load-deformation curve for material parameter Set 8 ( $\phi = 30^\circ$ ,  $\psi = 2^\circ$ ).

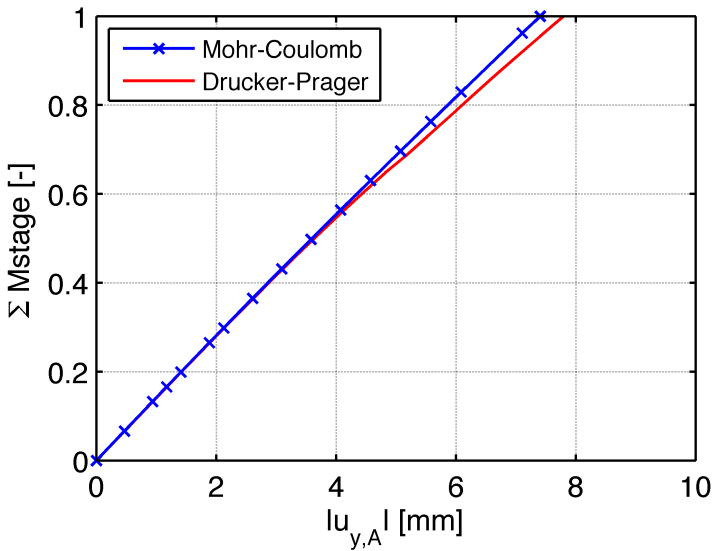


Figure E.4: Load-deformation curve for material parameter Set 9 ( $\phi = 30^\circ$ ,  $\psi = 30^\circ$ ).

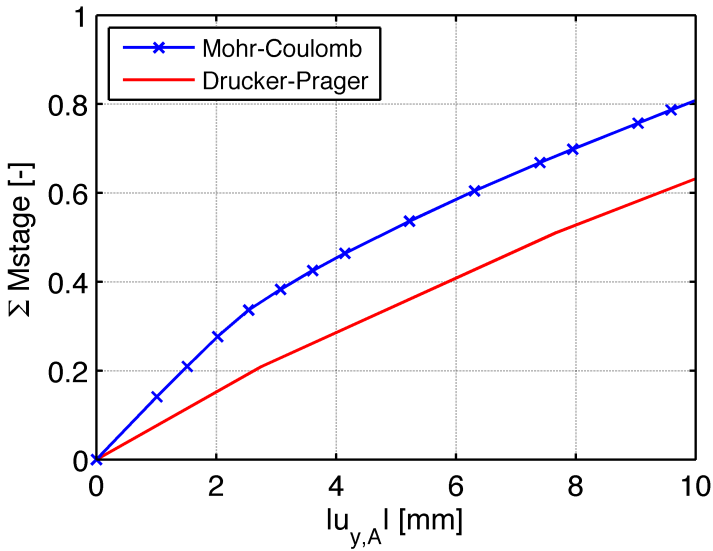
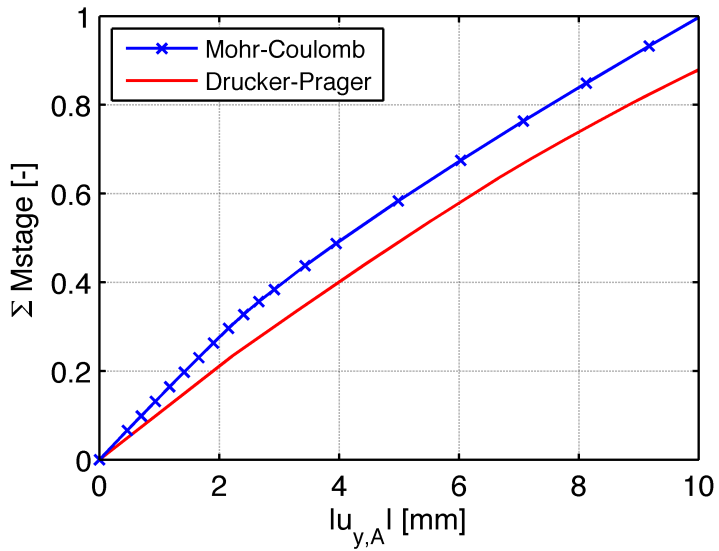
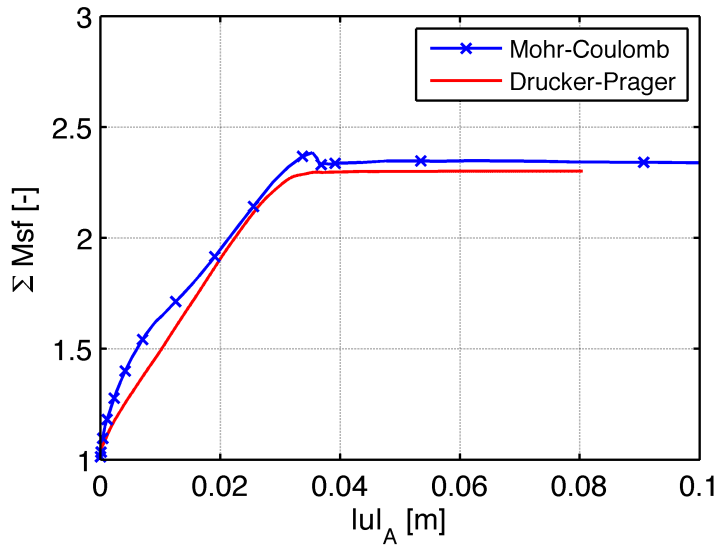


Figure E.5: Load-deformation curve for material parameter Set 10 ( $\phi = 20^\circ$ ,  $\psi = 0^\circ$ ).



**Figure E.6:** Load-deformation curve for material parameter Set 11 ( $\phi = 20^\circ$ ,  $\psi = 20^\circ$ ).

## E.2 Displacement-Factor of Safety Curves



**Figure E.7:** Safety factor-deformation curve for material parameter Set 6 ( $\phi = 30^\circ$ ,  $\psi = 0^\circ$ ).

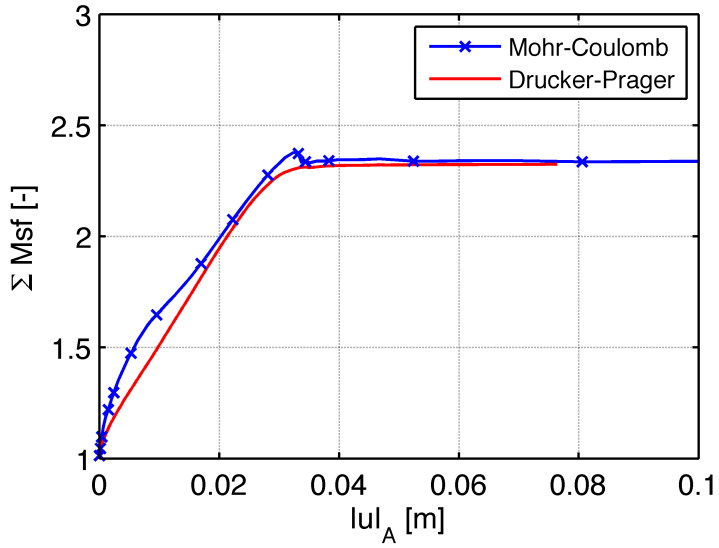


**Figure E.8:** Safety factor-deformation curve for material parameter Set 7, with friction ( $\phi = 30^\circ$ ,  $\psi = 1^\circ$ ).

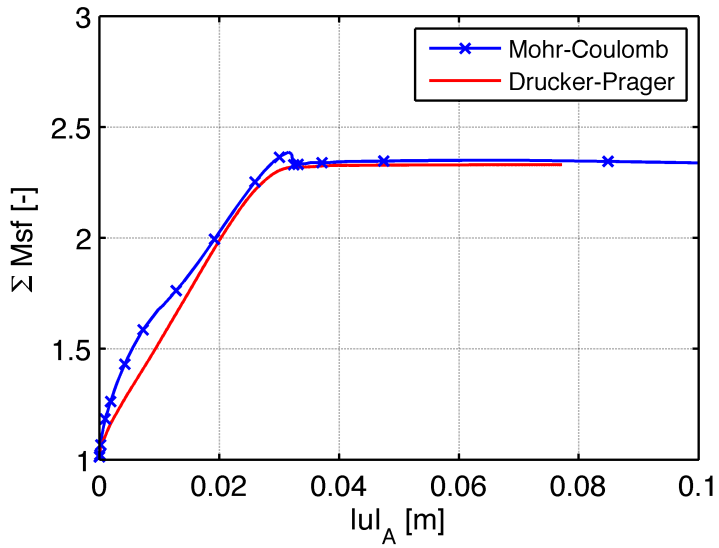


**Figure E.9:** Safety factor-deformation curve for material parameter Set 8 ( $\phi = 30^\circ$ ,  $\psi = 2^\circ$ ).



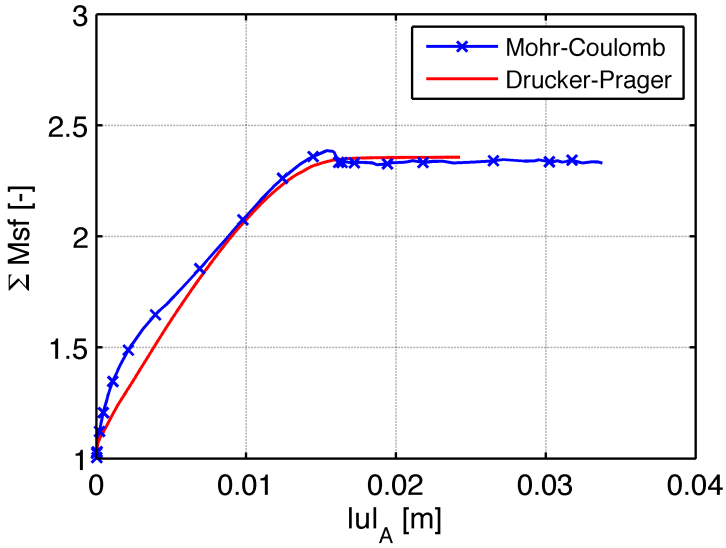


Figure E.10: Safety factor-deformation curve for material parameter Set 9, with friction ( $\phi = 30^\circ$ ,  $\psi = 30^\circ$ ).

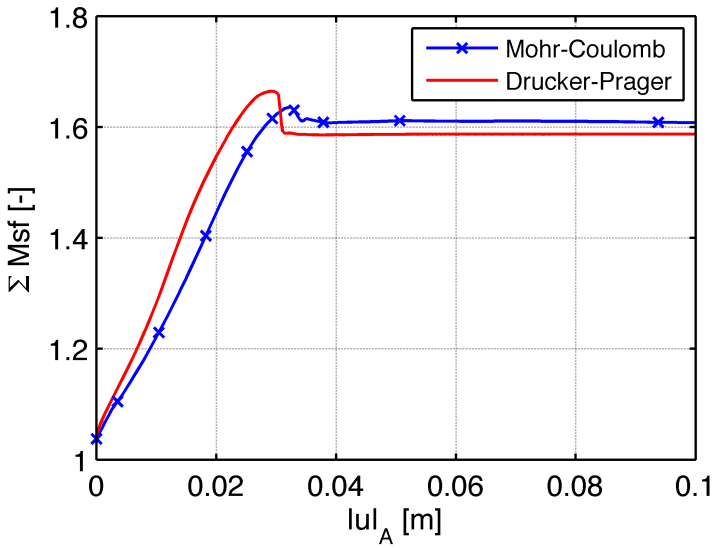
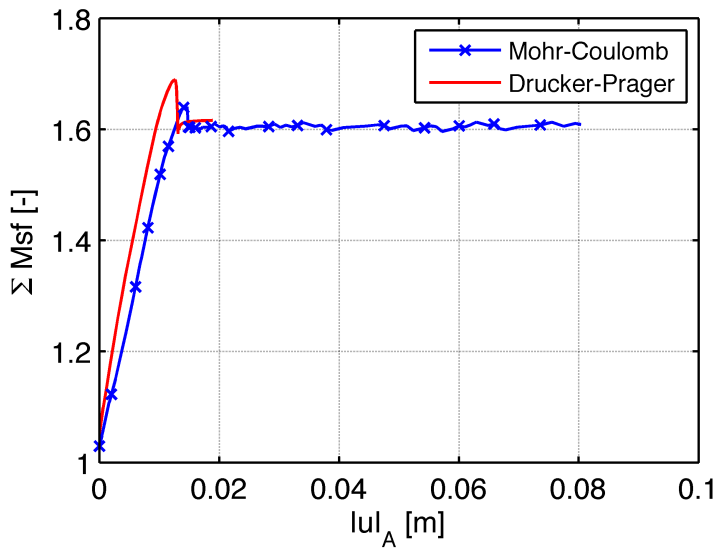
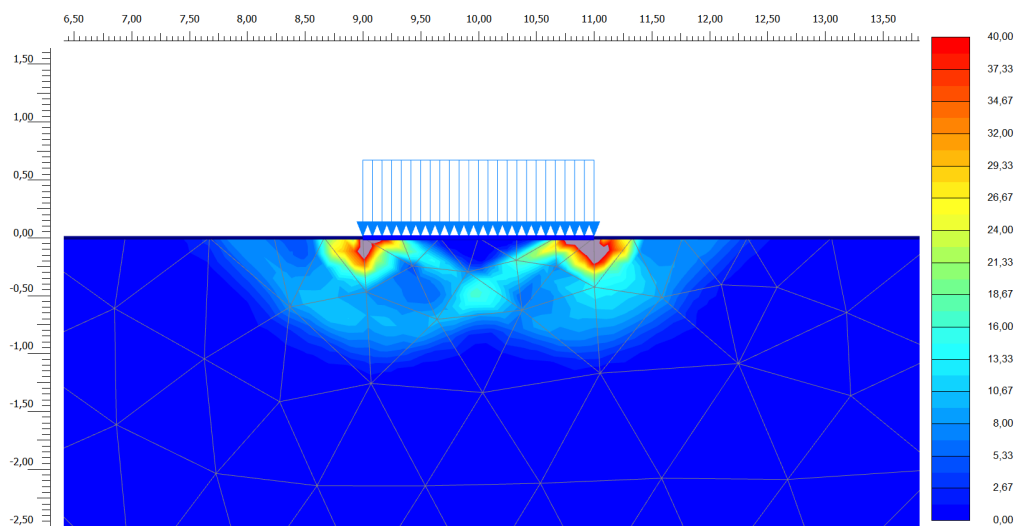


Figure E.11: Safety factor-deformation curve for material parameter Set 6 ( $\phi = 20^\circ$ ,  $\psi = 0^\circ$ ).



**Figure E.12:** Safety factor-deformation curve for material parameter Set 9, with friction ( $\phi = 20^\circ$ ,  $\psi = 20^\circ$ ).

### E.3 Shadings of Incremental Shear Strains



**Figure E.13:** Shadings of incremental shear strains at failure for Mohr–Coulomb model with material parameter Set 6 ( $\phi = 30^\circ$ ,  $\psi = 0^\circ$ ).

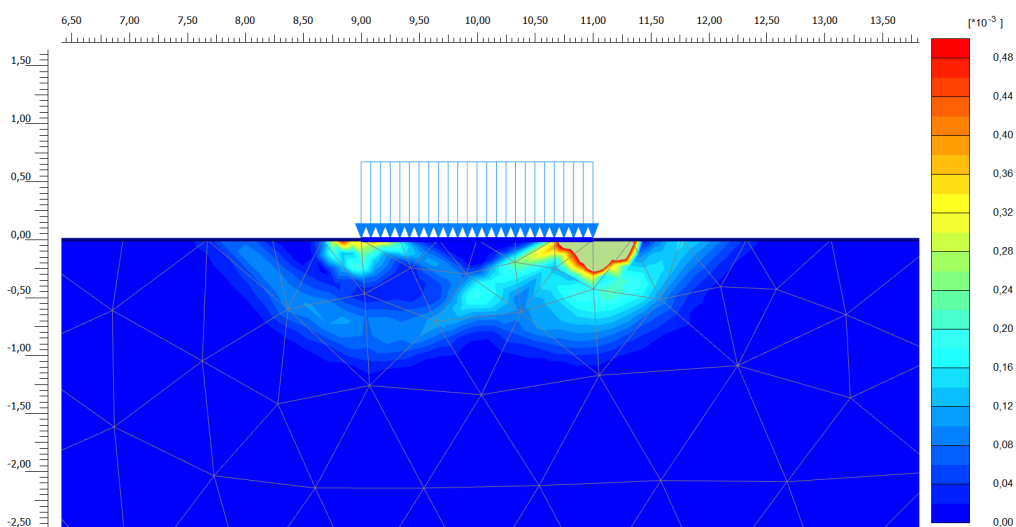


**Figure E.14:** Shadings of incremental shear strains at failure for Drucker–Prager model with material parameter Set 6 ( $\phi = 30^\circ$ ,  $\psi = 0^\circ$ ).

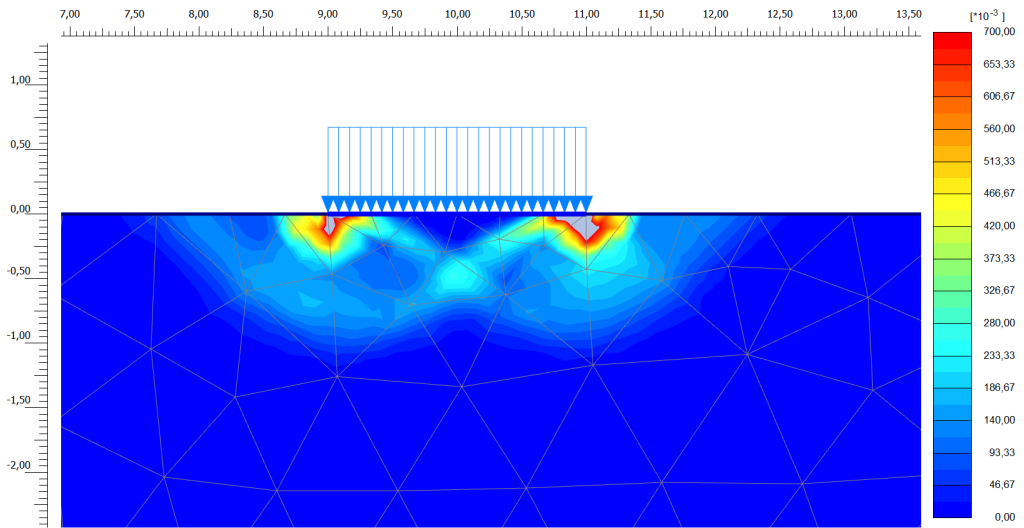


**Figure E.15:** Shadings of incremental shear strains at failure for Mohr–Coulomb model with material parameter Set 7 ( $\phi = 30^\circ$ ,  $\psi = 1^\circ$ ).

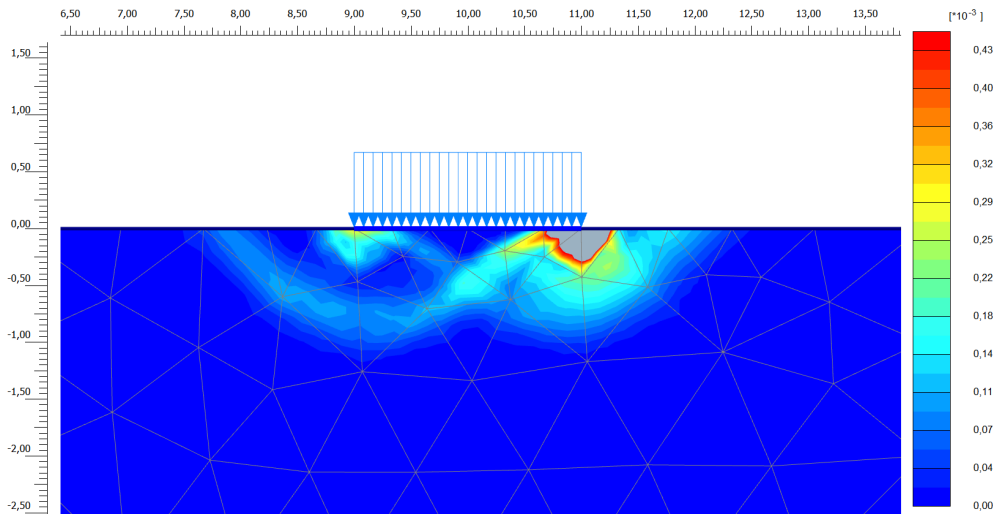


**Figure E.16:** Shadings of incremental shear strains at failure for Drucker–Prager model with material parameter Set 7 ( $\phi = 30^\circ$ ,  $\psi = 1^\circ$ ).

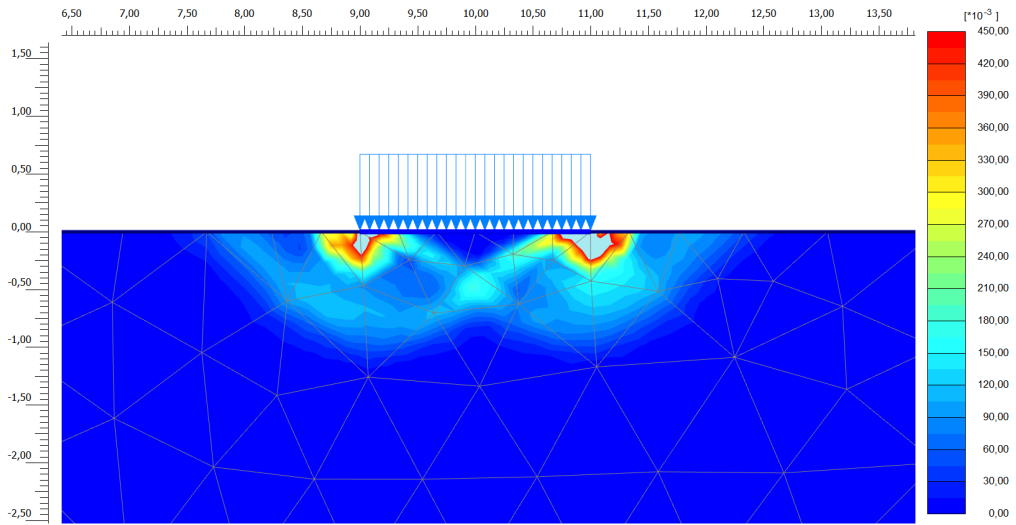


**Figure E.17:** Shadings of incremental shear strains at failure for Mohr–Coulomb model with material parameter Set 8 ( $\phi = 30^\circ$ ,  $\psi = 2^\circ$ ).

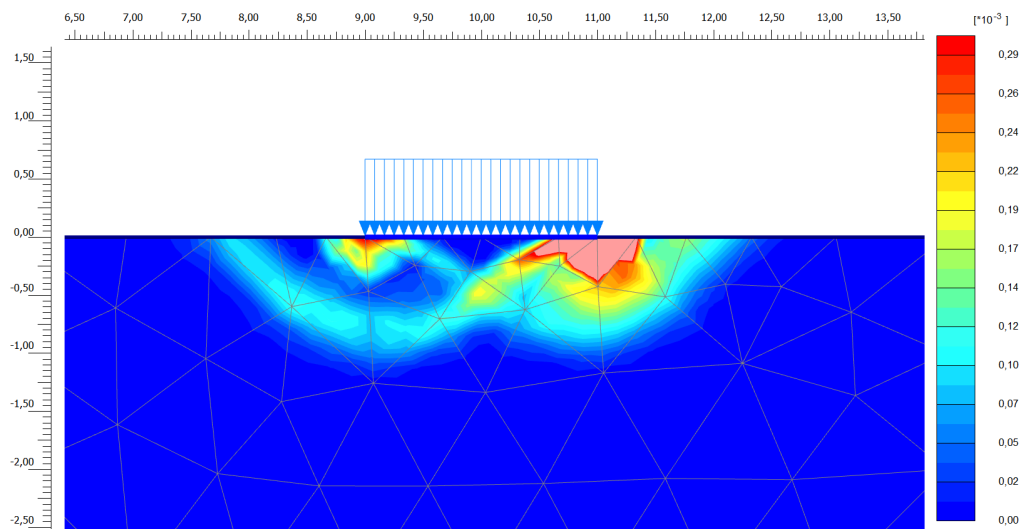


**Figure E.18:** Shadings of incremental shear strains at failure for Drucker–Prager model with material parameter Set 8 ( $\phi = 30^\circ$ ,  $\psi = 2^\circ$ ).

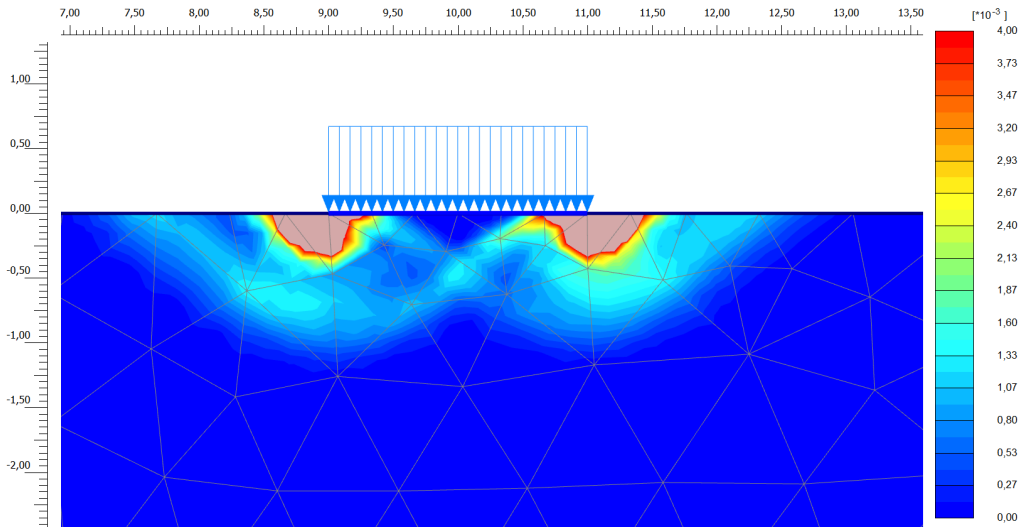


**Figure E.19:** Shadings of incremental shear strains at failure for Mohr–Coulomb model with material parameter Set 9 ( $\phi = 30^\circ$ ,  $\psi = 30^\circ$ ).

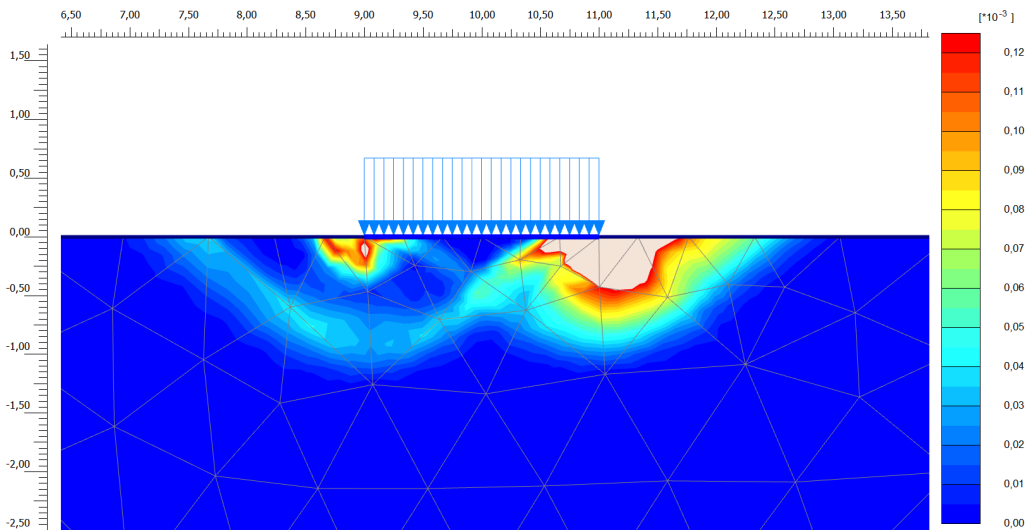


**Figure E.20:** Shadings of incremental shear strains at failure for Drucker–Prager model with material parameter Set 9 ( $\phi = 30^\circ$ ,  $\psi = 30^\circ$ ).

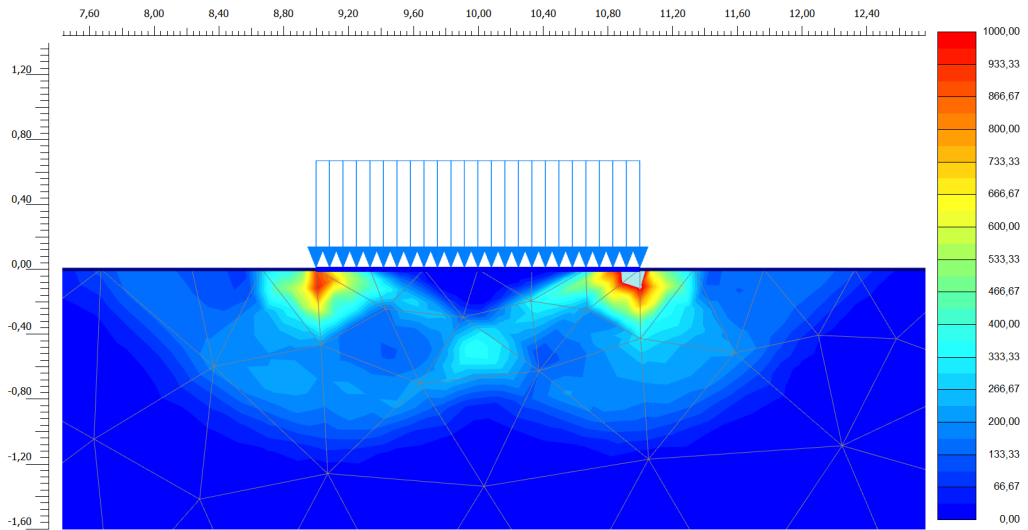


**Figure E.21:** Shadings of incremental shear strains at failure for Mohr–Coulomb model with material parameter Set 10 ( $\phi = 20^\circ$ ,  $\psi = 0^\circ$ ).

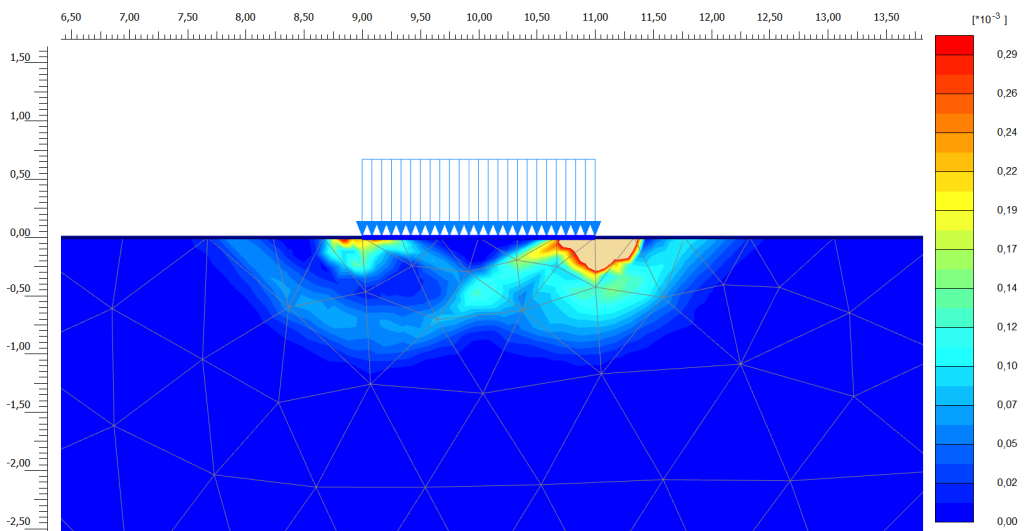


**Figure E.22:** Shadings of incremental shear strains at failure for Drucker–Prager model with material parameter Set 10 ( $\phi = 20^\circ$ ,  $\psi = 0^\circ$ ).

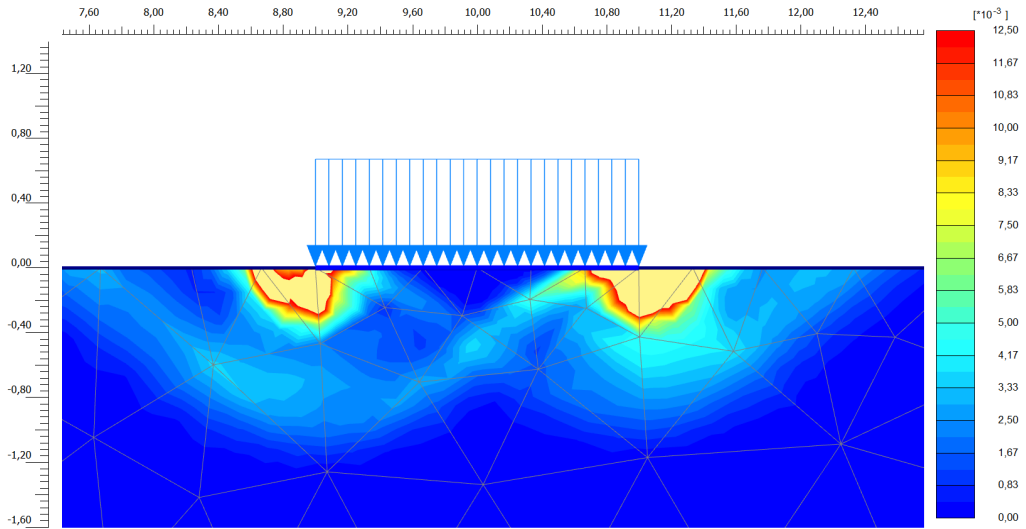


**Figure E.23:** Shadings of incremental shear strains at failure for Mohr–Coulomb model with material parameter Set 11 ( $\phi = 20^\circ$ ,  $\psi = 20^\circ$ ).

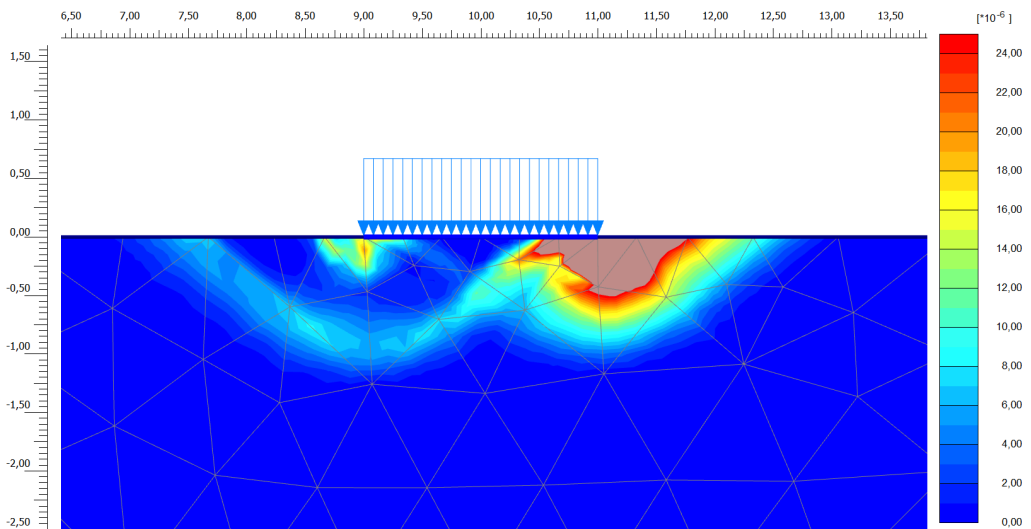


**Figure E.24:** Shadings of incremental shear strains at failure for Drucker–Prager model with material parameter Set 11 ( $\phi = 20^\circ$ ,  $\psi = 20^\circ$ ).